# Photo-thermal control of surface plasmon mode propagation at telecom wavelengths

Serkan Kaya

UNIVERSITÉ DE BOURGOGNE FRANCHE - COMTÉ

FACULTÉ DES SCIENCES

Laboratoire Interdisciplinaire Carnot de Bourgogne

Département Nanosciences

# PHOTO-THERMAL CONTROL OF SURFACE PLASMON MODE PROPAGATION AT TELECOM WAVELENGTHS

Thèse présentée à l'Université de Bourgogne Franche - Comté
pour obtenir le grade de Docteur (Mention Physique)

par

**Serkan KAYA**

Soutenue le 17 Octobre 2016 devant la commission d'examen composée de:

| | | |
|---|---|---|
| GAUTHIER-LAFAYE O. | Chargé de Recherche, LAAS Toulouse | Rapporteur |
| DAGENS B. | Directrice de Recherche, Univ. Paris Sud | Rapporteur |
| BRUYANT A. | Maître de conférence, Univ. de Tech. Troyes | Examinateur |
| CLUZEL B. | Maître de conférence, Univ. de Bourg. F.-C. | Examinateur |
| FINOT C. | Professeur, Univ. de Bourg. F.-C. | Co-directeur de thèse |
| WEEBER J.-C. | Professeur, Univ. de Bourg. F.-C. | Directeur de thèse |

*Dedicated to my dear parents,* ***Yaşar*** *and* ***Nurhayat***
*for their endless support,*

# Acknowledgement

This manuscript presents the PhD research that has been conducted in the interdisciplinary laboratory Carnot of Bourgogne under the groups of OSNC (Optique Submicronique et Nano-Capteurs) and SLCO (Solitons, Lasers et Communications Optiques) at the University of Burgundy Franche-Comté (Université de Bourgogne Franche-Comté) in Dijon. During this challenging and long period of time, I benefited from the advices, supports and guidance of several people that is why I would like to express my sincere appreciation to them without whom it would not have been possible to realize this work.

First, I would like to express my sincere gratitude to my advisors **Jean-Claude Weeber** and **Christophe Finot** for giving me a chance to perform this PhD study and related research, for their encouragement, patience, and immense knowledge. Without their precious guidance and support I could not able to conduct this research.

Secondly, I would like to thank Alain Dereux, the director of the interdisciplinary laboratory Carnot of Bourgogne, Eric Lesniewska, the director of the OSNC (Optique Submicronique et Nano-Capteurs) group and Guy Millot, the director of the SLCO (Solitons, Lasers et Communications Optiques) group for accepting me into the laboratory and their groups respectively for this research.

I would like to thank the members of the defense committee, Olivier Gauthier-Lafaye and Béatrice Dagens for accepting to be reviewers, Aurélien Bruyant and Benoît Cluzel for admitting to be examiners in this study.

A special thank goes to Alexandre Bouhelier for his helpful ideas and sharing his brilliant comments and suggestions in my experimental issues, to Gérard Colas des Francs for his support and guidance in performing numerical calculations, to Kamal Hammani for precious help and discussion while writing my thesis.

I express my gratitude to Eric Lesniewska and Eric Bourillot for their support in using AFM experimental setups. I would also like to thank Laurent Markey, Juan Arocas and Yvon Lacroute for giving me nanofabrication training and precious assistance whenever I needed.

I would furthermore like to thank my fellow labmates in the laboratory without whom I would not have had such wonderful times during my PhD study. Thanks Thomas, Ece, Simon, Pauline, Christian, Thibault, Stéphane, Antonin, Mingxia, Michael G. Nielsen, Filimon, Marie, Mickaël, Karim, Yacoub, Jean, Arunandan, Arnaud, Floriane and Padmnabh.

A special thanks to Elisabeth Lacroute for managing all our administrative tasks, her precious help and kindness.

I also want to thank Jean-Marc Muller and Brice Gourier from the Atelier of Mecanic Optics and Nanoscience for their support in fabrication of various instruments.

I would especially like to thank Tahsin AKALIN from the IEMN who excited and encouraged me for stepping into the world of science. Another special person that I would like to thank, is my twin brother **Sertan** living in the USA, who motivated and supported me throughout this PhD study. A special thanks to Connie Rippee, art director & creative consultant in the USA, for proof-reading English grammar of my dissertation.

Finally, I would like to thank my family; my devoted and beloved wife, **Feray**, words cannot express how grateful I am to you. You were always with me at every instant and tolerated me every time patiently. It would not have been possible to complete this study without your love and understanding. I would also like express my sincere gratefulness to my dear parents, Yaşar and Nurhayat and my dear parents-in-law, Lütfi and Birdal for their love, encouragement and permanent support during my PhD study.

# Abstract

Surface plasmon polaritons (SPPs) is the promising versatile platform proposed for guiding electromagnetic waves at nanoscale dimensions. In this context dynamic control of SPPs propagation is of paramount importance. Thermo-optical (TO) effect is considered as an efficient technique for performing active control of plasmonic devices. Among the thermo-optical based plasmonic devices demonstrated so far TO coefficient is dominantly provided by a dielectric material on top of the metal sustaining the SPP mode, however, the role of TO properties of the metal has been rarely investigated for plasmonic applications especially at the telecom frequency ranges. Therefore, the aim of this thesis is to investigate in detail the impact of thermo-optical properties of metals onto various SPP modes at telecom wavelengths.

First, we report on photo-thermal modulation of thin film SPP mode traveling at gold/air interface excited at telecom wavelengths. We start by investigating the photo-thermally induced modulation of SPPs propagation mediated by the temperature dependent ohmic losses in the gold film. Then we extract the thermo-plasmonic coefficient of the SPP mode from the accurately measured SPPs signal depth of modulation by which we could compute the thermo-optical coefficients (TOCs) of gold at telecom wavelength. Lastly, we demonstrate a pulsed photo-thermal excitation of the SPPs in the nanosecond regime.

Secondly, we investigate the thermo-optical dynamics of polymer loaded surface plasmon waveguide (PLSPPW) based devices photo-thermally excited in the nanosecond regime. First, we demonstrate thermo-absorption of PLSPPW modes mediated by the temperature-dependent ohmic losses of the metal and the thermally controlled field distribution of the plasmon mode within the metal. Next, we consider the thermo-optical response of a PLSPPW based racetrack shaped resonator coupled to a straight bus waveguide and evaluate the photo-thermal activation through heating and cooling times. We conclude that nanosecond excitation combined to high thermal diffusivity materials opens the way to high speed thermo-optical plasmonic devices.

Finally, we report on the photo-thermal modulation of SPPs propagation along lithographically fabricated gold nanowires sustaining highly confined plasmonic mode at telecom wavelengths. First, we investigate telecommunication characterization of the nanowires by applying high bit rate signal transmission, 10 Gbit/s, through fiber-to-fiber confocal detection setup. Next, we demonstrate and evaluate the photo-thermal modulation of SPPs propagation along the nanowires where we discuss qualitatively TO effects due to light-induced modulations on nanowires and show the impact of the incident beam polarization on the photo-thermal modulation.

**Key words:** Surface plasmon polaritons (SPPs), Plasmonic waveguides, Thermo-optical materials, Metal optics, Photo-thermal effects, Optical switching devices, Polymer waveguides

# Résumé

Les plasmons-polaritons de surface (PPS) font figure de plateforme polyvalente très prometteuse pour le guidage des ondes électromagnétiques à l'échelle nanométrique. Dans ce contexte, le contrôle dynamique de la propagation PPS est d'une importance capitale. Le contrôle actif des dispositifs plasmoniques a souvent été réalisé jusqu'à présent par le biais d'un effet thermo-optique (TO). Toutefois dans la majorité des cas considérés, l'effet thermo-optique résulte d'une modification des propriétés d'un matériaux diélectrique en contact avec le métal supportant le mode plasmon. Ainsi, le rôle des propriétés thermo-optiques du métal lui-même a rarement été analysé aux fréquences télécom dans le cadre d'applications plasmoniques. L'objectif principal de cette thèse est donc d'analyser en détail l'impact des propriétés thermo-optiques des métaux sur différents modes PPS aux longueurs d'ondes télécom.

En premier lieu, nous considérons la modulation photo-thermique d'un mode plasmon supporté par un film mince d'or se propageant à l'interface "or/air". Nous démontrons tout d'abord la modulation de la propagation des modes PPS induite par la dépendance des pertes ohmiques de l'or à la température du film mince. Le contrôle de la température du film est obtenu par un effet photo-thermique en régime continu modulé. Les mesures expérimentales de la profondeur de modulation de l'intensité des modes PPS combinées à la simulation numérique de la distribution de température le long du film d'or nous permettent de remonter aux coefficients thermo-optiques de l'or aux fréquences télécoms.

Dans un second temps, nous considérons le contrôle thermo-optique de modes plasmons dont le confinement spatial (et donc l'indice effectif) est supérieur à ceux des modes de films. Les modes considérés dans cette seconde étude sont connus sous le nom de "polymer-loaded surface plasmon waveguides (PLSPPWs)". Ces modes présentent un confinement latéral induit par l'indice de réfraction du ruban de polymère déposés sur le film métallique et un confinement vertical résultant de leur nature plasmonique. L'excitation photo-thermique de ces guides plasmoniques dans un régime nano-seconde nous permet de mettre en évidence la dynamique thermo-optique du métal aux temps courts (<1ns) et du polymère aux temps plus longs (<1$\mu$s). La même démarche appliquée à un micro-résonateur plasmonique en anneau révèle les temps caractéristiques de la dynamique de diffusion de la chaleur dans le polymère à l'échelle de quelques dizaines de nanomètres. Sur la base de ces expériences, nous suggérons un design de dispositifs plasmoniques thermo-optique dont la bande passante est de l'ordre du megahertz, un ordre de grandeur au-dessus des systèmes thermo-optiques traditionnels.

Enfin, nous présentons la modulation photo-thermique de la propagation PPS le long de

nanofils d'or fabriqués par lithographie éléctronique supportant des modes plasmons très confinés aux longueurs d'onde télécom. La transmission d'un signal télécom à 10 Gbit/s est tout d'abord démontrée afin d'établir sans ambiguïté la pertinence de tels guides d'ondes miniatures pour la transmission d'informations à très courtes échelles. Enfin, nous mettons en évidence la modulation photo-thermique de la propagation de tels modes. En particulier, nous investiguons l'influence sur la profondeur de modulation de la polarisation du faisceau pompe relativement à l'orientation des nanofils. Cet effet de polarisation s'explique par une absorption exaltée si la polarisation du faisceau pompe est orientée perpendiculairement à l'axe du nanofil. L'exaltation résulte de l'excitation d'un mode plasmon local selon l'axe transverse du nanofil.

**Mots clés:** Plasmon-polaritons de surface (SPPs), Guides d'onde plasmoniques, Matériaux thermo-optiques, Optique de métal, Effets photo-thermique, Dispositifs de commutation optique, Guides d'ondes en polymères

# Contents

# Introduction

We are witnessing exciting technological developments in recent years. Improvements of microelectronics in direct connection with the impressive fabrication performances particularly attracts great attention. However, the deceleration in miniaturization of electronic circuits in contrast to the expectation given by Moore's law have motivated researchers to investigate alternative solutions to overcome these limitations. Among different routes, the use of surface plasmon modes allowing for light fields concentration at nanoscale dimensions is considered as a promising solution for small footprint and very large bandwidth as optical platform interconnects. In fact, plasmons are collective oscillations of the metal's free electrons. Although surface plasmon polariton (SPP) mode can be sustained by highly doped semiconductors [1, 2], metals are still today the materials of choice for plasmonics. The presence of metals in an optical interconnect is obviously at the origin of light field damping, but it also offers the unique opportunity of controlling simultaneously optical and electrical signals using the same material. Once again, one can argue that highly doped semi-conductors can be used for the same purpose with however a much higher resistivity than for metals and thus a corresponding bandwidth for the electric signal much lower than in the case of metals. Using outstanding optical property of nano-engineered metals in conjunction with a dielectric material constituting a boundary when it is illuminated by electromagnetic waves under suitable conditions allows us to concentrate light waves at nanoscale dimensions. These generated waves either can be guided as electromagnetic waves along a flat boundary (at metal/dielectric interface) named as surface plasmon polaritons (SPPs) or can be found as a strong enhancement of the electromagnetic fields around nanoparticles named as localized surface plasmons (LSPs). Plasmonics is defined as the new branch of the nanophotonics which is interested in surface plasmons (SPs) waves and its applications [3–9].

Surface plasmons exhibit fascinating properties such as field confinement at the nanoscale dimensions. Owing to this property, plasmon-based waveguides may not be subjected to the diffraction limit imposed to photonic waveguides relying on refractive index contrast. In this respect, plasmon-based interconnects feature the large bandwidth of standard optical interconnect but also a very high potential in terms of compactness and miniaturization that bridges the gap between standard integrated optics circuitry and electrical circuitry at the chip scale [10].

For the development of a true plasmonic circuitry [11] integrated into real devices, something that has been accomplished only very recently [12–14], many components are needed. These components should be met not only passive components such as waveguides or couplers

but also be dynamic and allow for the control of SPPs signals during its propagation. While many works dealing with passive plasmon-based waveguides and devices have been reported, only very few works have been addressed specifically plasmonics dynamic devices. Among those works most of them rely on thermo-optical effect taking place into a dielectric material loaded onto the metallic film sustaining the plasmon mode [15–17]. At that stage and to the best of our knowledge, the role of the metal itself into thermo-optical processes has only very rarely been considered so far for plasmonic applications in particular at the telecom frequency range. It is the purpose of this thesis to investigate in detail the impact onto SPP modes propagation of the thermo-optical properties of metals at telecom frequencies.

Specifically, we investigate qualitatively and quantitatively the modulation of surface plasmon mode travelling along extended metal thin films, metal stripes and metal nanowires when the metal is heated by means of a photo-thermal effect. The use of a photo-thermal effect for metal heating features interesting properties such as controlled local heating switching from the continuous to the nanosecond regime, polarization dependence of the heating efficiency and direct numerical modeling. Besides, the photo-thermal heating is a process that is expected in any SPPs-based active configuration whenever the wavelength use to pump the gain material is significantly absorbed by the metal. In this respect, the results we discuss in the following are also of interest in the context of SPPs losses-compensation or amplification [18, 19]. Finally it is worth to note that our results can also be useful in the context of non-linear plasmonics where significant thermal contributions are expected.

The manuscript is organized as follows. In chapter 1, we briefly recall the properties of surface plasmon polariton (SPP) mode at the interface between a dielectric and a metal. This very basic configuration is useful to introduce quantity such as propagation length and penetration depth that are of paramount importance to any plasmonic waveguiding configurations. Next we focus onto a short and thus necessarily non-exhaustive review of plasmon-based active and dynamic devices that could be of interest for datacom applications.

After this literature review, in chapter 2, we investigate the photo-thermal modulation of thin film surface plasmon polariton (SPP) mode traveling at a gold/air interface excited at telecom wavelengths. By operating a modulated continuous-wave pump laser, the photo-thermally induced modulation of SPPs propagation mediated by the temperature dependent ohmic losses in the gold film is demonstrated. To that aim, we operate a fiber-to-fiber characterization set-up allowing us to measure accurately the SPPs signal depth of modulation. On the basis of these measurements, we extract the thermo-plasmonic coefficient of the SPP mode. By combining our measurements with tabulated values of the temperature-dependent imaginary part of gold dielectric function, we compute the thermo-optical coefficients (TOCs) of gold at telecom wavelengths. And finally, we investigate a pulsed photo-thermal excitation of the SPPs in the nanosecond regime on this type of plasmonic waveguides.

In chapter 3, we push forward the characterization of the dynamics of the photo-thermal SPPs modulation by operating a nanosecond pump laser. In particular, we demonstrate thermo-absorption of polymer loaded surface plasmon waveguide (PLSPPW) modes mediated by the temperature-dependent ohmic losses of the metal and the thermally controlled field distribution of the plasmon mode within the metal. Next, we consider the thermo-optical response of a PLSPPW based racetrack shaped resonator coupled to a straight bus waveguide and evaluate the photo-thermal activation in terms of heating and cooling times. The results discussed in this chapter address the dynamic of thermo-optical effects down to the regime of nanoseconds,

a topic that has not been considered so far for plasmonic waveguiding configurations.

Finally, in chapter 4, we investigate the photo-thermal modulation of SPPs propagation along lithographically fabricated gold nanowires sustaining highly confined plasmonic mode at telecom wavelengths. First, we demonstrate telecommunication characterization by performing high bit rate signal transmission experiment, namely 10 Gbit/s, along gold nanowires through fiber-to-fiber homemade confocal detection set-up at telecom wavelengths what is believed to be the first investigation in this context. Next, we focus onto optical characterizations of gold nanowires at telecom wavelengths in which the photo-thermal modulation of highly confined mode of SPPs propagation mode is investigated by illuminating nanowires with an electro-optically modulated CW visible laser. Finally, we demonstrate and discuss qualitatively thermo-optical effects due to the light-induced modulations on nanowires and emphasize the impact of the incident beam polarization on the photo-thermal modulation. More specifically, we show the depth of modulation of nanowire mode is affected by the polarization of the pump beam. This result is understood from the excitation of a local plasmon resonance of the nanowire along its transversal axis. In this respect, we demonstrate what we call a plasmo-plasmonic modulation process.

Chapter 1

# Plasmon-based waveguiding and integrated plasmonics

## 1.1 Introduction

Electronic devices and systems have become strictly indispensable and vitally necessary even in our daily life. Many operations such as our bank accounts, electronic mails, paying taxes, official works and so forth are conducted by means of computers and over the Internet. And also mobile phone, computer, television and radio are only some electronic devices that have become part of daily life. As its name suggests, word 'electronics' is derived from the word 'electron'. If we claim that all of the technological developments fundamentally is based on the discovery of the electron by the British physicist J.J. Thomson, we would not make a mistake. Since electrons are the key elements in electronic devices in order to transmit and receive signals. Controllability of the electron by various ways has opened this technological era.

Significant developments in nanotechnology recently allow for the fabrication of nanoscale structure. Although the building blocks of miniaturized electronics circuits has reached critical sizes of the order of a few nanometers, two major problems still stand in front of us as challenges such that *delay through interconnections* and *thermal issues*. On the other hand, optical systems always seem alternative solutions because of their bandwidth larger than their electronic counterparts. However, for standard optical waveguides relying on refractive index contrast, the diffraction limit imposes minimum waveguides cross-sections size of the order of half the wavelength of the light in the core material. Thus, while minimum electronic connections on the chip are of typical width of 14 nm [20], nowadays mature optical interconnection solutions are of typical sizes around half a micron making a co-integration of two technologies difficult on the same chip. At that stage, Plasmonics [3–5] has been identified as a promising candidate to overcome the footprint limitations of "classical" optical interconnects.

When the light waves impinge a metal-dielectric interface under suitable conditions, a type of surface waves can be generated by means of the interaction between incident light waves and surface mobile electrons of the metal which are not strongly connected to the atoms. In fact, the light waves excite these free electrons and then the electrons respond collectively by

making an oscillation eventually a resonant interaction forms between the incident light and the oscillation of free electrons at the same frequency. This resonant interaction generates a type of surface waves that propagates along the surface of the metal. As a matter of fact, the eigenmode sustained by the metal-dielectric interface are known as **surface plasmons (SPs)** whereas the coupling between the incident electromagnetic field and the surface plasmons are denoted as **surface plasmon polaritons (SPPs)** given that the incident field must generate polarization charges at the surface of the metal film for the surface plasmon mode to be excited. They are essentially trapped electromagnetic waves which propagate on the surface of the metal.

Why can plasmonics play a remarkable role between photonics and electronics? As a matter of fact, surface plasmon polaritons (SPPs) has been known more than a half of a century [6]. However, micro and nano fabrications were not developed in those days. Photonic devices were bulky. Besides, propagation length of surface plasmon polaritons (SPPs) was much smaller than the size of the components because of high losses in metals. As a result, it was not thought to use them as light carrier through photonics devices. With the technological developments, nanofabrication and electromagnetic simulation tools have progressed well. Currently, nanoscale components can be readily fabricated by different methods such as electron beam lithography or ion beam-milling. Thus, surface plasmon polaritons (SPPs) have gained renewed interest.

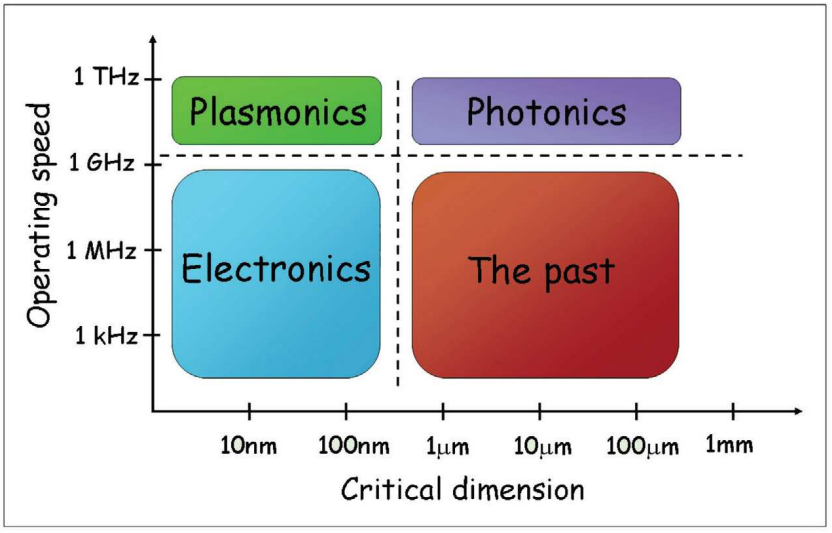


Figure 1.1: Evolution status of various chip technologies in terms of operation speed and critical dimension. It is widely accepted that a half micron to be a critical size for photonic devices (Image adapted from ref. [8] by permission from Elsevier © 2006)

As indicated above, the resonance frequency of SPPs equals to the frequency of the incident light waves. Whereas the wavelength of SPPs, in which the field of the SPPs not only extends into the superstrate but also in metal, is interestingly smaller than the light. This feature can be used to squeeze SPPs downto nanoscale structures such as nanowires, waveguides and etc. In principle, plasmonics can beat the diffraction limit at least if the reference wavelength

is the incident free space wavelength. What this means is that we can achieve to fabricate subwavelength photonic devices [7]. This is the superiority of the plasmonics with respect to the photonics. Furthermore, the interface of SPPs which is metal-dielectric also gives us an opportunity to transmit electrical signals as well as optical ones. In brief, plasmonics can be viewed as a good candidate for new generation chip technology [8].

Based on the discussion above, it can be concluded that plasmonics carries both of high bandwidth of photonics and the miniaturization of electronics. As can been seen in the figure 1.1 plasmonics can act as a bridge between photonics and electronics [9]. Therefore, it is widely accepted that plasmonics is capable to merge photonics and electronics at nanoscale dimensions [10].

The scope of plasmonics is not just limited to propagating or guiding of SPPs but also different domains such as biology, chemistry and medicine are interested in prospective potential of plasmonics. Cancer therapy mediated by nanoshells [21, 22], photoluminescence enhancement of LEDs in light industry [23, 24],plasmonic laser known as SPASER (surface plasmon amplification by stimulated emission of radiation) [25, 26], plasmon mediated SERS (surface enhanced raman scattering) [27] and plasmonic nanolithography [28, 29] are some of the growing areas of plasmonics. All the above-mentioned fields are however out of scope of this thesis which is oriented toward datacom applications of plasmonics.

In this very first chapter, we will briefly recall the basic properties of surface plasmon supported by a simple metal-dielectric interface along with standard coupling and excitation techniques when using an incident electromagnetic wave.

Next, we will give an extensive albeit non-exhaustive overview of plasmonics when applied for waveguiding and interconnect purposes. This field is so rich and the literature around that topic is so abundant that an exhaustive analysis of the state-of-art in waveguided plasmonic sounds rather difficult. Instead, we will focus onto either pioneering works or remarkable recent works that fit with the context of this thesis. Our subjective selection does not mean that other published results do not deserve consideration but just that those works are less relevant to our topic.

## 1.2 Plasmon basics

### 1.2.1 Drude model for metals

Prior to the discussion of the properties of SPP modes sustained by a metal-dielectric interface, it is worth to recall briefly the optical properties of metals through the crude but still useful Drude's model. One of the oldest and simplest models of metals is known as Drude Theory or Model. After J. J. Thomson discovered electrons in 1897, only 3 years later, a German physicist Paul Drude developed his famous model just before quantum theory appeared which explains the transport properties of electrons in metals. By applying successfully the kinetic theory of gases to metals, he was able to elucidate electrical and thermal conduction mechanisms in metals. In this model, ions are assumed to be immobile and valence electrons are considered to form a gas of electrons which wanders around the fixed ions. The fundamental assumptions of the model are [30]:

1) Except instantaneous collisions of electrons with immobile ions, the interactions of an

electron with the others and ions are neglected. These are known as independent electron approximation and free electron approximation respectively. So electrons travel in a straight line between the collisions in the absence of externally applied field.

2) The collisions of electrons are instant events that change the velocity of electrons. It happens between electrons and ions as can be seen in the molecules of a gas in the kinetic theory.

3) The collision time, the relaxation time or the mean free time between two subsequent collision is $\tau$. The probability of an electron having a collision in a time interval *dt* is $dt/\tau$.

4) After each collision, electrons get a thermal equilibrium with their surroundings. It means that electrons will have local temperature after a collision.

Although it models a metal in a simple manner, it is still used today for rough estimations. It can be concluded from the model that electrons travel in a straight line in the absence of externally applied field and collisions. If we apply an external electric field to a metal

$$m\frac{\partial^2 \mathbf{r}}{\partial t^2} + \frac{m}{\tau}\frac{\partial \mathbf{r}}{\partial t} = -e\mathbf{E} \tag{1.1}$$

will be the motion equation of an electron where *m* is the mass of the electron, *e* is the elementary charge, $\tau$ is the collision (relaxation) time and *r* is the direction of the electron [31]. If this external field assumes to be $\mathbf{E} = E_0 e^{-i\omega t}$, then the electron would also follow this harmonic field $\mathbf{r} = r_0 e^{-i\omega t}$. When we substitute **r** in the equation 1.1

$$\mathbf{r} = \frac{e\mathbf{E}}{m(\omega^2 + \frac{i\omega}{\tau})} \tag{1.2}$$

will be the displacement vector. The movement of the electron in the direction of the displacement vector **r** gives rise to *dipole moment* due to the separation of charges. Assuming $n$ electrons displacement per unit of volume lead to emerge the *polarization* of the metal. Total effect of the displacement of $n$ electrons to the polarization is

$$\mathbf{P} = -ne\mathbf{r} \tag{1.3}$$

$$\mathbf{P} = \frac{-ne^2\mathbf{E}}{m(\omega^2 + \frac{i\omega}{\tau})} \tag{1.4}$$

The *displacement field* also changes due to the polarization which is given by

$$\mathbf{D} = \epsilon_0\mathbf{E} + \mathbf{P} \tag{1.5}$$

$$\mathbf{D} = \epsilon_0\left(1 - \frac{ne^2/m\epsilon_0}{(\omega^2 + \frac{i\omega}{\tau})}\right)\mathbf{E} \tag{1.6}$$

At the right side of the equation 1.6 the term $\sqrt{ne^2/m\epsilon_0}$ is known as **plasma frequency** and denoted by $\omega_p$.

$$\mathbf{D} = \epsilon_0 \left(1 - \frac{\omega_p^2}{(\omega^2 + \frac{i\omega}{\tau})}\right)\mathbf{E} \tag{1.7}$$

$$\mathbf{D} = \epsilon_0 \epsilon_r \mathbf{E} \tag{1.8}$$

After substituting $\omega_p$ into the equation 1.7, we could also deduce the complex relative permittivity of the metal according to the correlation with the equation 1.8 which can be acquired as follows

$$\epsilon_r(\omega) = 1 - \frac{\omega_p^2}{\omega^2 + i\omega/\tau} \tag{1.9}$$

As seen above, the relative permittivity is a complex number which consists of real and imaginary parts. The imaginary part represents ohmic losses in the metal. Furthermore, the complex relative permittivity is a function of the driving frequency of the field making the relative permittivity a dispersive quantity. In the optical regimes that we are interested in $\omega > 1/\tau$ (satisfies at high frequencies), and it can be approximated to

$$\epsilon_r(\omega) = 1 - \frac{\omega_p^2}{\omega^2} \tag{1.10}$$

It is important to note that $\omega_p$ has a critical role in here [32]. When the driving frequency of the field, $\omega$ is greater than plasma frequency, $\omega > \omega_p$ , then $\epsilon_r$ would a positive real number. Consequently, the metal demonstrates a transparency characteristic to the electromagnetic radiation and no absorption occurs. This corresponds to ultraviolet regime in the electromagnetic spectrum. Conversely, if $\omega$ is smaller than plasma frequency, $\omega < \omega_p$, and so $\epsilon_r$ would a negative real number. This time the metal does not allow the propagation of the electromagnetic radiation through itself instead it absorbs the light and become a good reflector. This occurs in visible and infrared radiation.

### 1.2.2 Metal-Dielectric interface surface plasmon modes

The first observation of surface plasmon was reported by R.H. Ritchie in 1957. According to his angle-energy distribution characterization, while a fast electron passes through a metallic foil, it loses an amount of characteristic energy because of the excitation of plasma oscillations or **plasmons** [6]. Two years later, Powell and Swan confirm this loss behavior in their thin and thick film experiments [33]. With the start of these first attempts to explore surface plasmon polaritons (SPPs), numerous researches were conducted afterwards. H. Raether incorporated into and systematize these studies in his famous book, namely *Surface Plasmons on Smooth and Rough Surfaces and on Gratings* [34]. Afterwards, it should be indicated that researches

and publications in this area have exploded due to the progress in top-down and bottom-up nanofabrication techniques, high-performance simulation tools and new characterization techniques such as near-field and leakage radiation microscopies. In this section, we recall surface plasmon fundamental properties and comment on their typical dispersion relation, propagation length and penetration depth.

#### 1.2.2.1 Dispersion relation of SPPs for a single interface

Let us consider a planar interface composed of two semi-infinite medias, namely dielectric/metal, as shown in the figure 1.2. It is assumed to be that both of them are isotropic, non-magnetic, homogeneous and are characterized by own dielectric constants ($\epsilon_{i=1,2}$ corresponds to metal and dielectric medium respectively). A propagating electromagnetic-wave through this interface can be easily described by a wave equation with taking into account that the external charge ($\rho_{ext}$) and current densities ($\mathrm{J}_{ext}$) equal 0 for the maxwell equations:

$$\nabla^2\mathbf{E} - \frac{\epsilon}{c^2}\frac{\partial^2\mathbf{E}}{\partial t^2} = 0 \tag{1.11}$$

If it is assumed that all fields have harmonic-time dependence as $\mathbf{E}(r,t) = E(r)e^{-iwt}$, then we can transform the wave equation to the helmholtz equation in a such way:

$$\nabla^2\mathbf{E} + k_0^2\epsilon\mathbf{E} = 0 \tag{1.12}$$

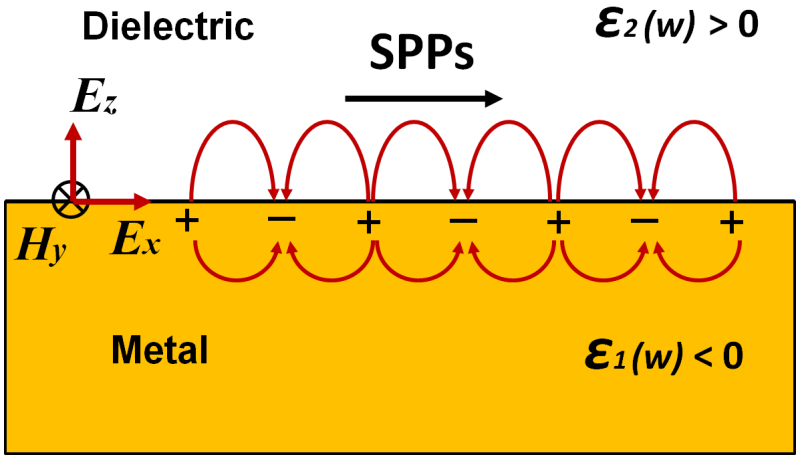


Figure 1.2: SPPs can only be supported if both of the relative permittivity of metal $\epsilon_1$ and dielectric $\epsilon_2$ are in opposite sign. TM (Transverse magnetic) character is a specific feature of the SPPs waves where the magnetic field oriented in the $k_y$ direction

where $k_0 = w/c$ is the free-space wave vector. We also suppose that the wave propagates towards to x-direction along the $z = 0$ plane (or the interface) and exponentially vanishes along z-directions into both medias. So, we can demonstrate propagating electromagnetic waves as

$$\mathbf{E}(x,y,z) = E(z)e^{i\beta x} \qquad \mathbf{H}(x,y,z) = H(y)e^{i\beta x} \tag{1.13}$$

where $\beta$ is the propagation constant of the wave along x-direction and equals $k_x$ wave vector. Substituting these equations into the helmholtz equation 1.12 is going to give us

$$\frac{\partial^2 \mathbf{E}(z)}{\partial z^2} + (k_0^2\epsilon - \beta^2)\mathbf{E} = 0 \qquad \frac{\partial^2 \mathbf{H}(y)}{\partial y^2} + (k_0^2\epsilon - \beta^2)\mathbf{H} = 0 \tag{1.14}$$

wave equations in appropriate forms. If we solve Maxwell's equations, namely Maxwell-Faraday and Ampere's laws, through the wave equations, we are going to get

$$\frac{\partial E_z}{\partial y} - \frac{\partial E_y}{\partial z} = i\omega\mu_0 H_x \tag{1.15a}$$

$$\frac{\partial E_x}{\partial z} - \frac{\partial E_z}{\partial x} = i\omega\mu_0 H_y \tag{1.15b}$$

$$\frac{\partial E_y}{\partial x} - \frac{\partial E_x}{\partial y} = i\omega\mu_0 H_z \tag{1.15c}$$

$$\frac{\partial H_z}{\partial y} - \frac{\partial H_y}{\partial z} = -i\omega\epsilon_0\epsilon E_x \tag{1.15d}$$

$$\frac{\partial H_x}{\partial z} - \frac{\partial H_z}{\partial x} = -i\omega\epsilon_0\epsilon E_y \tag{1.15e}$$

$$\frac{\partial H_y}{\partial x} - \frac{\partial H_x}{\partial y} = -i\omega\epsilon_0\epsilon E_z \tag{1.15f}$$

Besides, these equations can be simplified due to the propagation along only x-direction, $\frac{\partial}{\partial x} \rightarrow i\beta$, and homogeneity along the y-direction, $\frac{\partial}{\partial y} \rightarrow 0$ as follows [35]:

$$\frac{\partial E_y}{\partial z} = -i\omega\mu_0 H_x \tag{1.16a}$$

$$\frac{\partial E_x}{\partial z} - i\beta E_z = i\omega\mu_0 H_y \tag{1.16b}$$

$$i\beta E_y = i\omega\mu_0 H_z \tag{1.16c}$$

$$\frac{\partial H_y}{\partial z} = i\omega\epsilon_0\epsilon E_x \tag{1.16d}$$

$$\frac{\partial H_x}{\partial z} - i\beta H_z = -i\omega\epsilon_0\epsilon E_y \tag{1.16e}$$

$$i\beta H_y = -i\omega\epsilon_0\epsilon E_z \tag{1.16f}$$

This equation set allows two kinds of solutions which correspond to two type of wave polarizations such that transverse electric (TE or s) mode sustaining $E_y, H_x, H_z \neq 0$ and transverse magnetic (TM or p) mode sustaining $E_x, E_z, H_y \neq 0$.

The solutions for TE mode can be expressed in each media as follows, for $z > 0$:

$$E_y(z) = A_2 e^{i\beta x} e^{-k_{2,z} z} \tag{1.17a}$$

$$H_x(z) = -i\frac{A_2 k_2}{\omega\mu_0} e^{i\beta x} e^{-k_{2,z} z} \tag{1.17b}$$

$$H_z(z) = \frac{A_2 \beta}{\omega\mu_0} e^{i\beta x} e^{-k_{2,z} z} \tag{1.17c}$$

for $z < 0$:

$$E_y(z) = A_1 e^{i\beta x} e^{k_{1,z} z} \tag{1.18a}$$

$$H_x(z) = i\frac{A_1 k_1}{\omega\mu_0} e^{i\beta x} e^{k_{1,z} z} \tag{1.18b}$$

$$H_z(z) = \frac{A_1 \beta}{\omega\mu_0} e^{i\beta x} e^{k_{1,z} z} \tag{1.18c}$$

where $A_i, k_i$ are amplitude coefficients and normal components of wave vectors for each medium respectively. Since the electric field, $E_y$ and the magnetic field, $H_x$, components must be continuous along the interface, it can be deduced from the above-mentioned equations such that:

$$k_{1,z} + k_{2,z} = 0 \tag{1.19}$$

However, the surface bound modes only occurs when both $\Re\{k_1\}$ and $\Re\{k_2\} > 0$ [35] which cannot be fulfilled for the condition above. So, it is concluded that there is no SPP modes for TE polarization.

Let us investigate the conditions for TM polarization. The solutions of the equations set in 1.16 for TM mode can be demonstrated as follows, for z > 0:

$$H_y(z) = A_2 e^{i\beta x} e^{-k_{2,z} z} \tag{1.20a}$$

$$E_x(z) = i\frac{A_2 k_2}{\omega\epsilon_0\epsilon_2} e^{i\beta x} e^{-k_{2,z} z} \tag{1.20b}$$

$$E_z(z) = -\frac{A_2 \beta}{\omega\epsilon_0\epsilon_2} e^{i\beta x} e^{-k_{2,z} z} \tag{1.20c}$$

for $z < 0$:

$$H_y(z) = A_1 e^{i\beta x} e^{k_{1,z} z} \tag{1.21a}$$

$$E_x(z) = -i\frac{A_1 k_1}{\omega\epsilon_0\epsilon_1} e^{i\beta x} e^{k_{1,z} z} \tag{1.21b}$$

$$E_z(z) = -\frac{A_1 \beta}{\omega\epsilon_0\epsilon_1} e^{i\beta x} e^{k_{1,z} z} \tag{1.21c}$$

In this case, considering again boundary conditions, continuity of both the tangential components, $H_y$, $E_x$ along the interface, and the normal component of the electric displacement field across the interface, $D_{z,i} = \epsilon_i E_z$, so result in:

$$A_1 = A_2 \qquad \text{and} \qquad \frac{k_{2,z}}{k_{1,z}} = -\frac{\epsilon_2}{\epsilon_1} \tag{1.22}$$

We must emphasize that these results can only be provided when the real parts of permittivity of metal and dielectric are found to be opposite sign which is a fundamental requirement for the existence of SPP mode for a single interface at TM mode. This condition can be readily fulfilled by noble metals whose relative permittivity is known to be negative below the plasma frequency while the dielectric ones are generally positive and constant. Besides, SPPs excitation can only be launched through a TM polarization of the electromagnetic field where the normal component of the electric displacement field is continuous across the interface whereas the normal component of the electric field is discontinuous (see fig.1.2). So, this cause to change the sign (or direction) of the electric field across interface (in the z direction) which provides to trap electrons at the interface surface. Thus, these trapped charges respond to the incident electromagnetic field by collectively moving back and forth longitudinally at the interface which is in fact the origin of the coupling mechanism for SPPs excitation.

Again returning back to the calculation, $H_y$ has to satisfy the wave equations which can be deduced from the equations 1.16:

$$k_{1,z}^2 + k_0^2\epsilon_1 - \beta^2 = 0 \qquad k_{2,z}^2 + k_0^2\epsilon_2 - \beta^2 = 0 \tag{1.23}$$

By combining these wave equations with the results in 1.22 will give us the **dispersion relation of SPP mode** for a single interface between two semi-infinite isotropic media as shown below [34]:

$$\beta = k_0\sqrt{\frac{\epsilon_1\epsilon_2}{\epsilon_1 + \epsilon_2}} \tag{1.24}$$

where $\beta = k_{spp}$ , the parallel component of the wave vector at the direction of the propagation, is named as the *SPPs wave vector*, and $\epsilon_1$, $\epsilon_2$ are relative permittivities of the metal and dielectric medium respectively. Since the relative permittivity of the metal $\epsilon_1$ is a complex number, the wave vector of SPPs, $k_{spp}$ , is also complex which can be written as:

$$k_{spp} = k_{spp}^{'} + ik_{spp}^{''} \tag{1.25}$$

in which $k_{spp}^{'}$ and $k_{spp}^{''}$ are respectively the phase constant and the attenuation constant of the SPP mode.

Let us now discuss on the SPPs dispersion relation which is schematically plotted in the figure 1.3. The dark-yellow solid line, $\omega = ck_x$, represents light line and the dark-blue one corresponds to SPPs dispersion curve without damping based on the Drude model previously demonstrated in the equation 1.10. As can be seen, the SPPs dispersion curve lies right of the light line due to its bound nature and a momentum mismatch is clearly noticeable at the same frequency where the SPPs' one, ($\hbar k_{spp}$ ), is greater than the light's one, ($\hbar k_0$). This implies that in order to generate SPPs from the light waves, this momentum difference must be bridged as explained in the context of the excitation and coupling techniques subsequently. Due to this momentum difference SPPs also cannot radiate easily into free-space, showing a

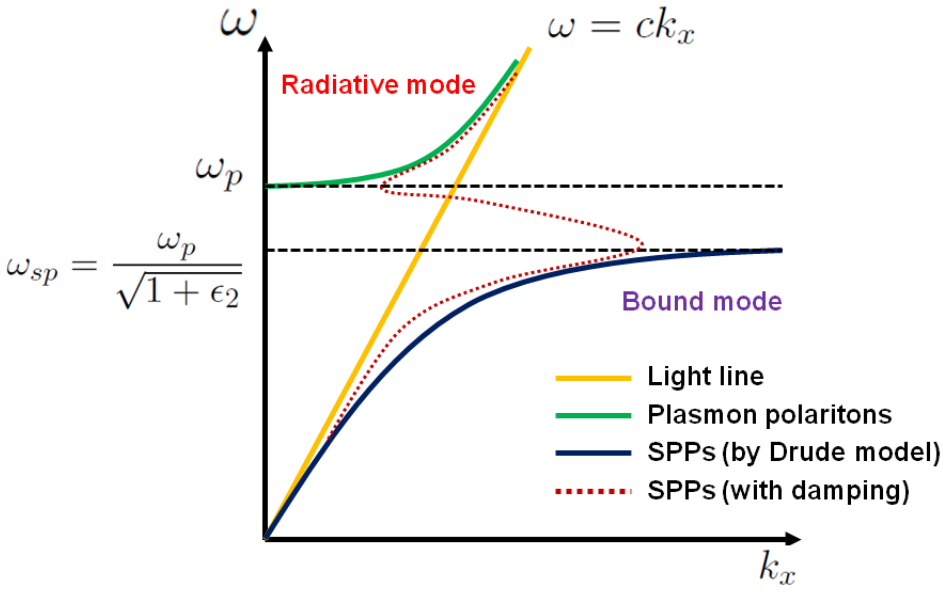


Figure 1.3: Dispersion relation of surface plasmon polaritons (SPPs) depicted depending on Drude model without damping and a real metal model with damping

bound or non-radiative nature, which is a very desired situation while transmitting or guiding SPPs waves through plasmonic components (such as waveguides, couplers and etc.).

At low frequencies (or for small $k_{spp}$), the dispersion curve approaches to the light line and SPPs demonstrates a light-like character (grazing-incidence) but still is larger than the light line. If the frequency increases gradually, the dispersion curve starts to move away from the light line and approaches to asymptotic frequency limit for large $k_{spp}$ values which is called *surface plasmon resonant frequency*, $\omega_{sp}$ (see fig.1.3). By assuming that the damping is being zero at this stage and if the frequency continues to increase, then the wave vector will go to the infinity. So, the group velocity is also going to be zero and the mode demonstrates electrostatic character, transforms to surface plasmons (SPs).

On the other hand, considering damping in SPPs propagation, which is the actual situation in a real metal because of the intraband and interband transitions of electrons, results in a back-bending on the dispersion curve (see fig.1.3). Besides, the SPPs wave vector can reach a finite value at surface plasmon frequency, $\omega_{sp}$, which leads to a limitation on both surface plasmon wavelength, $\lambda_{sp}$ and mode confinement of the SPPs wave into each medium [35]. This confinement is described by the normal component of the wave vector deduced from the equations above as follows [34]:

$$k_{z,i} = \sqrt{\epsilon_i \left(\frac{\omega}{c}\right)^2 - k_{spp}^2} \tag{1.26}$$

where $\epsilon_i$ is the relative permittivity of the metal and the dielectric medium respectively for $i = 1, 2$.

At plasma frequency, it is possible to excite longitudinal collective oscillations of the conduction electrons inside the metal, known as *volume plasmons* which is depicted by a solid-

green in the figure 1.3. For the frequency greater than the plasma frequency, $\omega > \omega_p$ , metal behaves a transparent character and radiation through the metal occurs.

#### 1.2.2.2 The propagation length of the SPPs

As SPPs propagates along a smooth metal surface, it gradually attenuates and loses its energy. The energy is absorbed by the metal which in turn is dissipated as heat. The distance for which the intensity of SPPs decreases to the 1/e value of its initial energy is defined as the **propagation length** and denoted by $L_{spp}$ . The attenuation constant of the SPPs wave vector $k_{spp}^{''}$ corresponds to the absorption of the metal and is used to calculate the propagation length of the SPPs which is given by [34]:

$$L_{spp} = \frac{1}{2k_{spp}^{''}} = \frac{c}{w}\left(\frac{\epsilon_1^{'} + \epsilon_2}{\epsilon_1^{'}\epsilon_2}\right)^{3/2} \frac{(\epsilon_1^{'})^2}{\epsilon_1^{''}} \tag{1.27}$$

This dissipation channel is commonly denoted as the ohmic loss channel. This basic remark is at the origin of the works described in the following. Given that in the absence of scattering loss mechanism a SPPs loses its energy as heat and it is possible to control SPPs propagation by controlling the temperature of the metal sustaining the plasmon mode. Losses originating from ohmic losses of the metal are still a challenge in the plasmonics world. So far, many different strategies and structures have been proposed in order to overcome this obstacle and will be discussed further in the following.

#### 1.2.2.3 The penetration depth of the SPPs

The penetration depth describes the spatial extensions of the electromagnetic field amplitudes of the SPPs into surrounding media which are metal and dielectric. We have previously mentioned that SPPs is characterized by two wavevectors $k_{spp}\,(k_x)$ and $k_z$ which are parallel and perpendicular to the interface respectively as shown in the figure 1.2. If we take $k_{z,i}$ from the equation 1.26 and substitute into the dispersion relation in the equation 1.24, we are going to obtain penetration depths as given below [34]:

$$\delta_d = \frac{\lambda}{2\pi}\left(\frac{\epsilon_1^{'} + \epsilon_2}{\epsilon_2^2}\right)^{1/2} \qquad \delta_m = \frac{\lambda}{2\pi}\left(\frac{\epsilon_1^{'} + \epsilon_2}{\epsilon_1^{'\,2}}\right)^{1/2} \tag{1.28}$$

$\delta_d$ and $\delta_m$ correspond to penetration depth into dielectric and metal respectively.

The nature of the exponential decay in both of the media known as *evanescent character* and demonstrates bound and nonradiative features of the SPPs [7]. As shown schematically in the figure 1.4, decay length of $\delta_d$ inside the dielectric medium is generally greater than the metal's one is approximately on the order of half wavelength of incoming light whereas $\delta_m$ is typically on the order of a few tenth of nanometers. In addition, while the intensity of electric field is maximum at the surface (at z=0), it exponentially decays towards to surrounding media (see fig.1.4(b)). Therefore, SPPs is extremely sensitive to the surface roughness of the metal. By tailoring or nanoenginnering of the metal surface, SPPs can be readily controlled and guided through subwavelength components such as waveguides, switches, and etc. due to their surface bounded character.

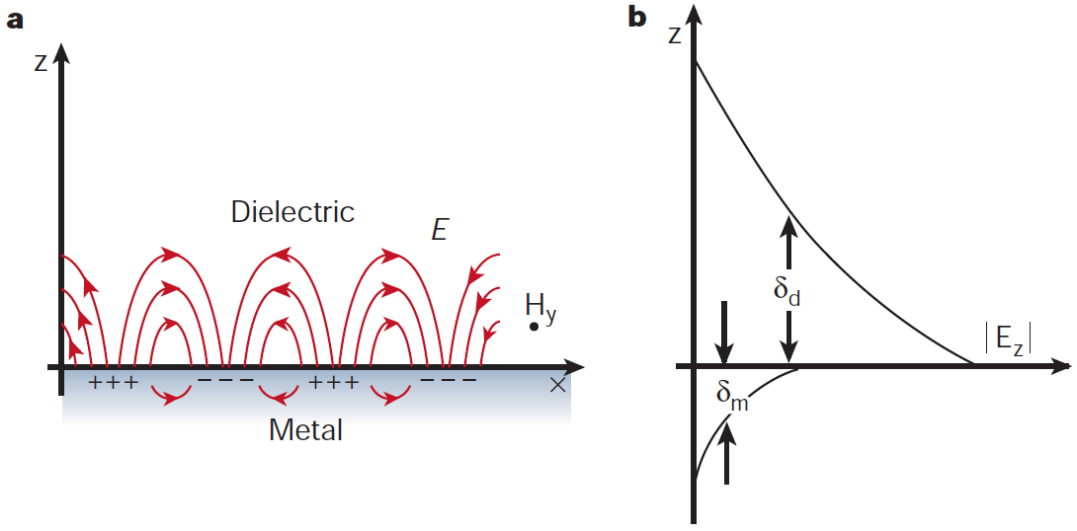


Figure 1.4: (a) SPPs waves at a metal-dielectric interface which demonstrates a hybrid character of electromagnetic fields and surface charges (b) The penetration depths inside two neighboring media; metal and dielectric conjunction with the electric field intensity (Images adapted from ref. [7] by permission from Macmillan Publishers Ltd. © 2003)

### 1.2.3 Thin films surface plasmons modes

So far we have considered only the surface plasmon modes of a single interface. However, in most practical applications, the SPP mode of interest is sustained by a thin film. At that stage, the penetration depth $\delta_m$ is a good parameter to look at in order to determine whether SPP modes sustained by a thin film mode significantly different from the SPP modes of the corresponding interfaces. Thin films configurations can be classified in two types of structures: insulator-metal-insulator (IMI) and metal-insulator-metal (MIM) systems.

#### 1.2.3.1 Insulator-metal-insulator (IMI)

In this type of structures, a thin metal film is surrounded by two thick dielectric claddings. This configuration can support two separate SPPs film modes at each dielectric-metal side if the distance between adjacent interfaces larger than the decay length of SPP modes. Otherwise, when the separation is smaller, the SPPs film modes of each side start to interact depending on their dielectric constants and leads to a coupled mode. This coupled mode can be classified in two modes according to transverse electric field distributions; antisymmetric and symmetric mode (see fig.1.5). If the thin metal film is placed on a symmetric medium (see fig.1.5), the solutions would be named as long-range SPP mode which supports the largest propagation length of SPPs with low confinement. If the medium is asymmetric, the solutions would be short-range SPP mode that provides a high confinement through the metal film.

#### 1.2.3.2 Metal-insulator-metal (MIM)

This time, a thin dielectric layer is surrounded by two metallic claddings. If the dielectric constants of both metals are supposed to be same, an attractive mode without cut-off can be achieved for thinner dielectric cores [36]. Besides, by changing the thickness and material, the confinement at each metal side can be controlled. Gap SPPs can be pointed out one of the promising modes, which provides very high confinement, will be considered later.

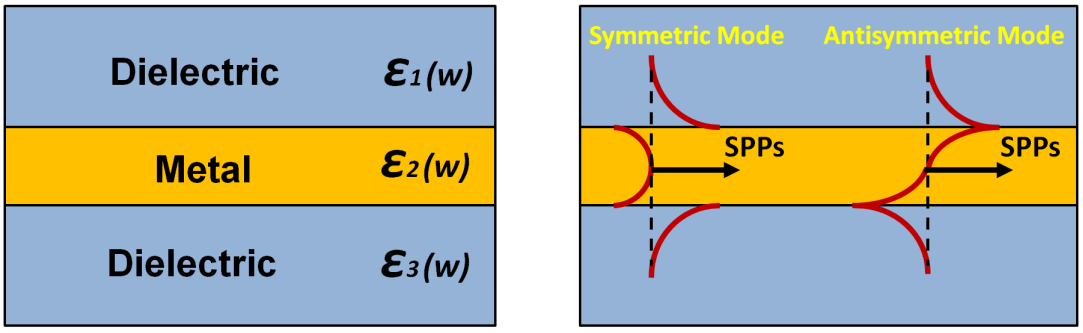


Figure 1.5: (a) If $\epsilon_1 = \epsilon_3$ then it corresponds to symmetric medium, conversely if $\epsilon_1 \neq \epsilon_3$ corresponds to asymmetric medium (b) According to transverse electric field distributions, modes are classified as symmetric and antisymmetric modes like sketched above (assumed to be in a symmetric medium)

### 1.2.4 Excitation and coupling techniques

In this section we briefly discuss the techniques that are commonly used for the excitation of surface plasmon modes. Different techniques have been proposed so far in the literature. We would like summarize the most known techniques which are excitation by electrons, prism coupling and grating coupling.

#### 1.2.4.1 Excitation by electrons

The first attempt of excitation by electrons was carried out by Ritchie [6]. By using fast electrons which penetrates through a metallic foil, he could able to excite SPPs. In fact, while a fast electron passes through a solid, it transfers its momentum and energy to the electrons of the solid. Then, it losses some of its energy and is scattered towards a different direction.

High-energy free electrons ($\sim$ 50 keV) can also excite SPPs on metal surfaces which shows that electron beam excitation on unstructured metal surfaces provides a localized source of SPPs [37]. Propagating SPPs can be generated not only in metal surfaces but also in different geometries such as planar dielectric cavities, metallic wires and nanoparticle waveguides can be provided by fast electrons with high efficiency [38].

Besides high-energy electrons, recently it has been demonstrated that low-energy electrons can excite SPPs on one end of a nanowire as well [39]. The physical mechanism in this technique is to tunnel electrons between a gold tip and a single-crystal gold nanorod that first excites gap plasmons and then in turn couples to SPPs along the nanorod. This last method seems to be a promising approach amongst all of them due to requiring less power, voltage-controlled and nanoscale compatibility.

#### 1.2.4.2 Prism coupling

Prism coupling or ATR (Attenuated total reflection) coupling is a well-known optical technique used for SPPs excitation. There are two fundamental configurations: **Otto** [40] and **Kretschmann-Raether** [41] (see fig.1.6).

Otto configuration consists of a quartz or glass prism, a dielectric spacer layer and a metal film. By using a dielectric prism with a higher refractive index, the wave vector of light (or momentum) can be increased. If the incident angle of the light waves is adjusted to be larger than the critical angle ($\theta_{ATR} > \theta_C$) while passing through the boundary between the prism and the dielectric spacer layer, attenuated total reflection (ATR) will occur which leads to launch evanescent waves. These waves in fact are able to excite SPPs waves along the spacer layer-metal interface as soon as both of their wavevectors being equal. The excitation can be determined experimentally whenever a strong decrease is observed in the reflection measurement (ATR minimum).

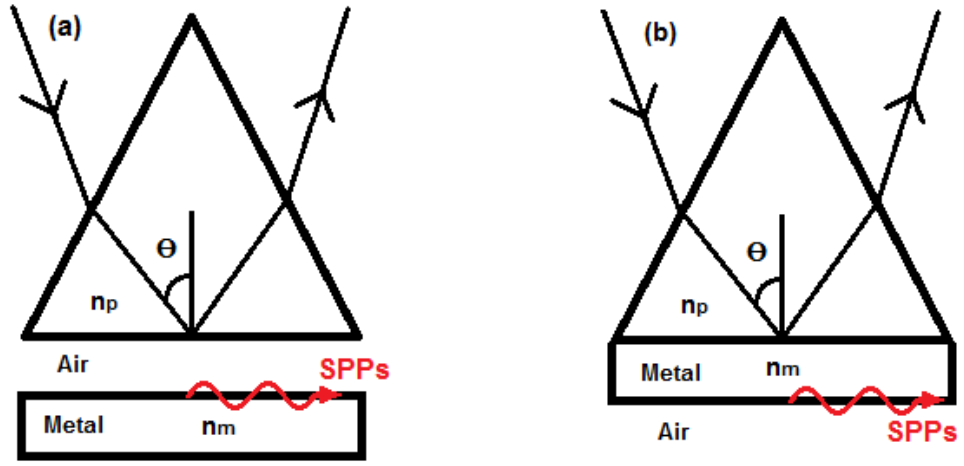


Figure 1.6: (a) Otto configuration: dielectric prism - air - metal (b) Kretschmann-Raether configuration: dielectric prism - metal - air

The second configuration Kretschmann-Raether looks like the Otto configuration but a thin metal film is evaporated at the bottom of the prism used as a spacer layer instead of the air. As above-mentioned total reflection condition is again used to launch evanescent waves which can penetrate through the metal film provided that its thickness is not much larger. So, SPPs can be excited along the metal-air interface (on other side of the metal film) by means of the evanescent fields if the resonant condition is satisfied.

#### 1.2.4.3 Grating coupling

Grating coupling is an another optical technique used to couple incident radiation to the SPPs. By nano-fabricating a particular pattern such as corrugations or shallow gratings on a metal's surface, the translational symmetry of the surface can be removed. When incident radiation strikes these gratings as shown in the figure 1.7, it will be scattered by adding or subtracting integer multiples of a grating momentum vector $G = 2\pi/a$ (a is the period of the gratings)

from the incident radiation. Then, a part of the incident waves reflects and the other parts produce diffracted and evanescent waves. So, the evanescent waves provide an additional momentum to the incident waves in order to couple to the SPPs.

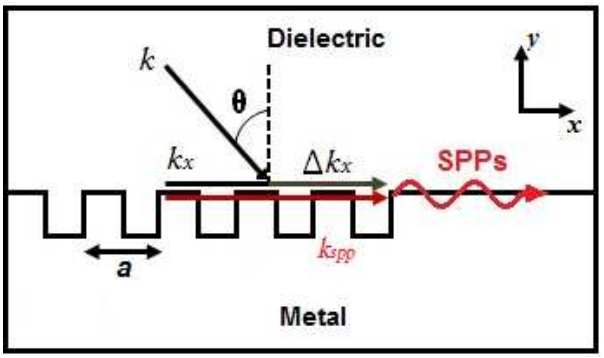


Figure 1.7: Grating couplers between a metal and a dielectric interface which provides an additional momentum to incident waves to fulfill the coupling requirements of the SPPs

The theoretical correlation between incident wave vector $k$, grating vector $G$ and SPPs wave vector $k_{spp}$ is given by [34]:

$$\pm k_{spp} = ksin\theta \pm Gm \tag{1.29}$$

$$\pm k_{spp} = k_x \pm \Delta k_x \tag{1.30}$$

$\theta$, $k_x$ and $\Delta k_x$ correspond to incident angle with respect to the normal of the gratings, in-plane vector component of the incident wave vector and additional momentum vector respectively. $G = 2\pi/a$ is the grating momentum vector where $a$ is the period of the gratings. And $m$ is an integer that corresponds to the order of scattering. The sign $\pm$ in front of $\Delta k_x$ represents addition or subtraction of the momentum vector on the in-plane vector $k_x$ which can cause to change the propagation direction of the generated SPPs ($\pm x$ direction). Note that the equations 1.29 and 1.30 are only true provided that the gratings sustained a Bloch mode with a wave-vector only little different from the smooth interface SPPs. This happens in the case of point-like scatterers deposited onto a flat surface or shallow gratings.

A reverse process is also possible in which propagating SPPs can be transformed into the light waves by decreasing its momentum through the grating couplers. Recently, the use of the grating coupling technique has increased due to the flexibility in computer-aided design and easy producibility by means of micro/nano fabrications such as electron-beam lithography, UV lithography and focused ion beam-milling.

## 1.3 Plasmonic waveguiding

In this paragraph we focus onto the plasmon-based waveguiding configurations that have been suggested and described in the literature so far. As mentioned earlier, we are forced to restrict our discussion to a limited number of configurations given the abundant literature dealing

with that topic. We choose to organize the description of the different kinds of plasmon based waveguides as a function of the field confinement they provide.

### 1.3.1 Low field confinement

#### 1.3.1.1 Thin film based waveguides

**Long-range and short-range SPPs**

Guiding SPPs along thin film waveguides has been demonstrated long time ago by many researchers in various structures. Economou elaborated the dispersion relation of surface plasmons in single and multiple thin films [42] where he uncovered various modes of surface plasmons as the metal thickness decreases in multiple-film systems and classified them into two main groups which will be named afterwards *symmetric* and *antisymmetric* modes (see fig.1.5). Sarid also observed and confirmed these two modes [43]. As the metal film thickness decreases gradually on a symmetric or asymmetric medium, the spatial extensions of the two SPP modes on each side of the film begin to overlap through the metal film and give rise to a transverse standing wave. He demonstrated that this degenerated SPPs wave splits into two modes symmetric and antisymmetric mode with respect to the transverse electric field distribution (see fig.1.5). Due to the less penetration of the field across the metal film and so leading small dissipations, the symmetric mode is named as the long-range SPP (LR-SPP) mode where SPP waves travel large distances but with a weak confinement. After only 2 years later, experimental observations of long-range SPPs were demonstrated on thin metal films which were coherent with the previous theoretical predictions [44].

On the other hand, the antisymmetric mode corresponds to the short-range SPP (SR-SPP) mode where the field is mostly confined inside the metal film leading large dissipation of the signal and so results in small propagation distance of SPPs. However, this mode has a outstanding feature that provides strong localization of guided signal, enabling to achieve beyond the diffraction limit, which is aimed for designing subwavelength integrated nanooptic/nanoplasmonic devices. Short-range SPP mode is provided various type of structures involving nanowires, metal-gap, -slot and -clad waveguides which all will be elaborated later.

Burke pushed forward thin film based studies by revising the dispersion relations of waves guided by a thin and lossy metal films surrounded by dielectric media [45]. He indicated that generally accepted two modes, symmetric and antisymmetric, were also split into a pair of radiative (leaky) and nonradiative (bound) modes showing totally four solutions to the dispersion relations. Besides this work, an exhaustive analysis of all kind of long-range surface modes on thin films surrounded by dielectric media was reported on both symmetric and asymmetric geometries [46]. It presented theoretically and experimentally that a long-range surface modes may exist for almost any dielectric values of the thin film.

By this time, majority of the studies related with the SPPs propagation along thin films assuming that the width of thin films to be infinite which could only provide 1D confinement. For the first time, Berini studied the properties of guided plasmon-polariton waves through a thin lossy metal film with a finite width. In this work, the propagation of purely bound electromagnetic modes was investigated along a thin lossy metal film embedded in both symmetric and asymmetric geometry. In the symmetric geometry, four fundamental modes and a few higher order modes were observed. One of the fundamental modes showed attractive characteristics

which had a lower attenuation values than the thick metal slab counterparts implying to be a good candidate for finite width metal film waveguide structures due to supporting long-range mode. Indeed, as the dimensions of thin film were reduced to $w \sim 1\mu\, m$ and $t \sim 15\, nm$, it provided highly low attenuation values that was in the range of 0.1 to 10 dB/cm at the telecom wavelengths [47]. On the other hand, the mode spectrum provided by the asymmetric geometry was rather different and complex from the symmetric one. Only one of the higher modes was observed to be a long-range mode although its attenuation decreases very quickly with the decreasing film thickness. Besides, the cutoff thickness of this mode was found to be greater than the one of symmetric and slab waveguide geometries. This long-range mode seemed to be quite sensitive to the small induced changes of substrate and superstrate refractive indices which have to be taken into account while choosing surrounded media [48]. The superiority of the thin metal films of finite width to those of infinite widths is not only providing 2D field confinement along the film but also allow us to fabricate various waveguides with the intention of guiding SPPs waves towards a particular direction and address.

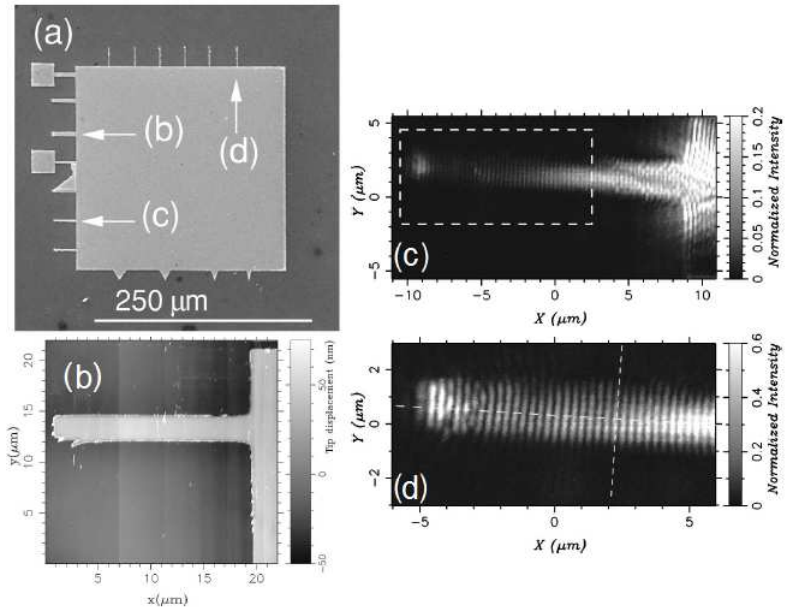


Figure 1.8: (a) Scanning electron microscope (SEM) image of homogeneous silver thin film and various connected finite width thin metal films (stripes) supported by a glass substrate (b) SEM image of a silver stripe which had a width of 2.5 $\mu$m and a length of 18 $\mu$m (c) PSTM image of the SPPs propagation (takes place from right to left) through the silver stripe (The tip-sample distance is 100 nm) (d) More closer PSTM image of the SPPs propagation through the same silver stripe (The tip-sample distance was less than 50 nm) (Image adapted from ref. [49] by permission from the American Physical Society © 2001)

Afterwards, experimental confirmation of the propagation of long-range plasmon-polariton mode guided by a thin metal film of finite width embedded in a symmetric medium was demonstrated at the telecom wavelength [50]. Polarization dependence of the main mode was investigated by means of varying polarization angle of incidence. Besides, it was proved that the experimental results were found to be a fair agreement with the previous theoretical predic-

tions.

The first near-field observation of SPPs propagation on thin silver metal stripes (finite-width thin metal films) at a visible frequency was presented by Weeber et al. [49]. The experimental measurement setup was composed of a *photon scanning tunneling microscope* (PSTM) which was not only a suitable and efficient tool to observe in direct space but also allowed to use ATR excitation technique straightforwardly [51]. SPPs is launched by a focused beam on a homogeneous thin silver film whose area is much larger than the incident spot and then SPPs is guided through the metal stripes of various widths (see fig.1.8).

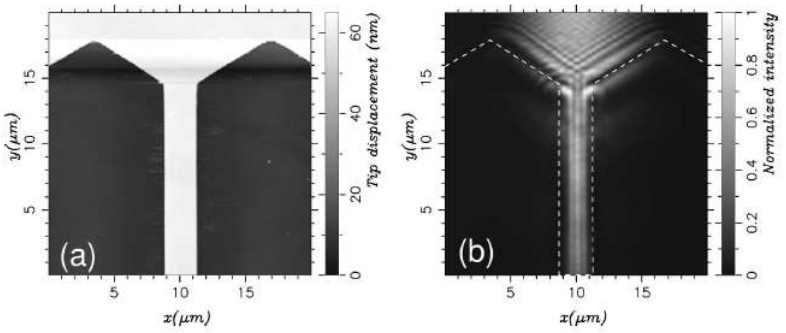


Figure 1.9: (a) The AFM image of the 2.5 $\mu$m wide stripe (b) The PSTM image of the SPPs propagation which excited on whole gold film and propagates through 2.5 $\mu$m wide stripe (Image adapted from ref. [52] by permission from the American Physical Society © 2003)

The silver metal stripes deposited on a glass substrate support propagation of SPPs were microfabricated by a lithography process and excitation of SPPs was provided by ATR configuration. The propagation constant of the SPPs propagation could be deduced directly from constant-height PSTM images and it was concluded that as the width of the stripe is about four times the SPPs wavelength, the propagation constant of the SPPs through the metal stripe were equal to the one of the whole silver film. Consequently, the stripe width of 2.5 $\mu$m provided a good coupling between whole thin film SPPs and the stripe mode. Furthermore, the focus of the SPPs field could be achieved by using a stripe with a triangularly shaped termination.

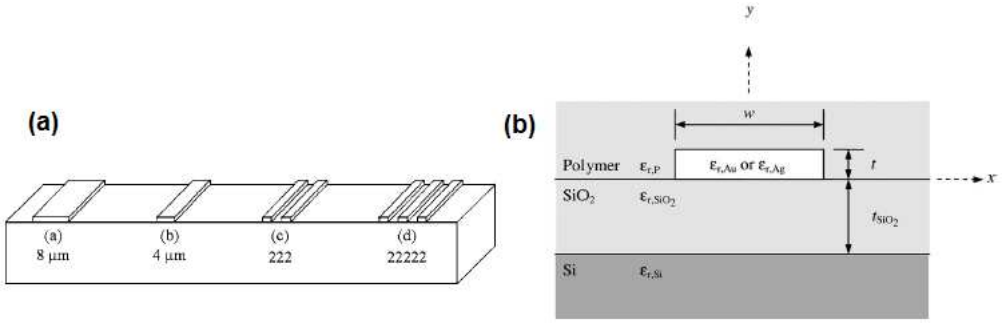


Figure 1.10: (a) Various waveguide structures in different finite widths (b) Cross-section of a general waveguide structure (Image adapted from ref. [53] by permission from AIP Publishing © 2005)

Due to the inconvenience of thin silver stripes to observe the feature of transverse intensity profile via the PSTM, the optical near-field distribution of thin gold stripes in various widths

was investigated at a wavelength of 800 nm [52]. An attractive feature was observed that field distributions of SPPs strongly confined within the width of the stripes as in the lateral confinement of a dielectric waveguide which could only be obtainable for high contrast of refraction index between the core and the cladding (see fig.1.9). However, the propagation of SPPs along the thin gold stripes did not depend on the reflection of fields on the lateral edges of the stripes which was the case fundamentally in guided modes of dielectric waveguides. Thus, SPP modes along the metal stripes exhibited a hybrid mode that was coupling of interface and boundary modes and was mostly localized at the lowest index side of the interface.

The largest propagation lengths of SPPs waveguides that support long-range mode was reported so far to be 10340 $\mu$m for Au finite width thin film and 13572 $\mu$m for Ag finite width thin film of which both were embedded in an optically homogeneous dielectric [53]. These results also correspond to the lowest measured attenuations values which are 0.42 and 0.32 dB$/$mm at the Au and Ag waveguides respectively at the telecom wavelength $\lambda$=1.55 $\mu$m. (see fig.1.10)

**Active plasmonics with gain**

Although the plasmonics can be accepted as a promising platform for nanophotonics due to its versatile properties, there are still some challenges where the most frustrating one is high losses. In order to overcome this obstacle, various approaches have been proposed so far in which *loss compensation* and *amplification* can be mentioned as primary solutions [54]. While loss compensation is meaning to reduce existing losses, amplification is generally referring to provide much more gain rather than the compensation losses and also to extend the lifespan of SPPs. So now, we will present various remarkable works in this context.

Nezhad et al. investigated SPPs propagation on several metal-dielectric configurations in the presence of a gain medium next to it [55]. Their analytic and numerical calculation indicated that the gain medium could compensate losses and provide a SPPs propagation with little or nearly without losses along these waveguides. Besides, they calculated the gain layer's effect and from here deduced possible relative locations in order to provide best compensation for the practical applications at infrared wavelengths.

Seidel et al. demonstrated one of the first experimental amplification of SPs on an attenuated total reflection (ATR) setup [56]. By employing organic dye molecules (rhodamine 101 or cresyl violet in ethanol) which could be optically pumped (580 nm) for serving as a gain medium, the stimulated emission of SPs (633 nm) at the interface between a thin silver film and the gain medium could be detected by means of the reflectance versus the incident angle measurements. This amplification did not only compensate SPs losses but also changed characteristic reflectance dip of SPs which was a clear evidence of the stimulated SPs emission.

The active control of SPPs propagation along *dielectric-loaded surface plasmon polariton waveguides (DLSPPWs)* was also investigated. Grandidier et al. reported that the propagation length of confined SPP modes a could be increased to 27% at telecom wavelength by the help of stimulated emission of quantum dots (QDs) which were to be doped inside a polymer strip-loaded waveguide [57]. A polymer (PMMA) strip waveguide with dimensions of 600 nm height, 400 nm width and 65 $\mu$m long on a 40$\pm$3 nm thick gold film fabricated by UV-lithography was doped with lead sulfide (PbS) QDs (see fig.1.11). Illuminating of the doped polymer waveguide only by a 532 nm laser could pump the QDs to their excited states and caused to exhibit a emission of QDs fluorescence at 1.5 $\mu$m wavelength. By the investigation

of the leakage radiation microscopy, it was demonstrated that this fluorescence emission could couple to SPP mode supported by the DLSPPW. In order to achieve this coupling, the SPP mode was excited by a TM-polarized infrared laser beam $\lambda$=1.55 $\mu$m focused on the taper of the doped polymer waveguide. And then the waveguide was homogeneously illuminated by the 532 nm laser to see the effect of the QDs on the SPPs propagation. It was found that while the propagation length was constant around 13.5 $\mu$m for pump irradiance under 500 $\mathrm{W/cm^2}$, it increased to 17.2$\pm$1 $\mu$m for 1000 $\mathrm{W/cm^2}$ of which was greater than the propagation length of the undoped waveguide. As a matter of fact, the QD emission caused to the doped polymer (PMMA) to act as an optical gain medium. The increase of 27% in the propagation length of the SPPs corresponded to a 160 $\mathrm{cm^{-1}}$ optical gain coefficient. So, this gain could provide a compensation of confinement-induced SPPs losses of DLSPPW.

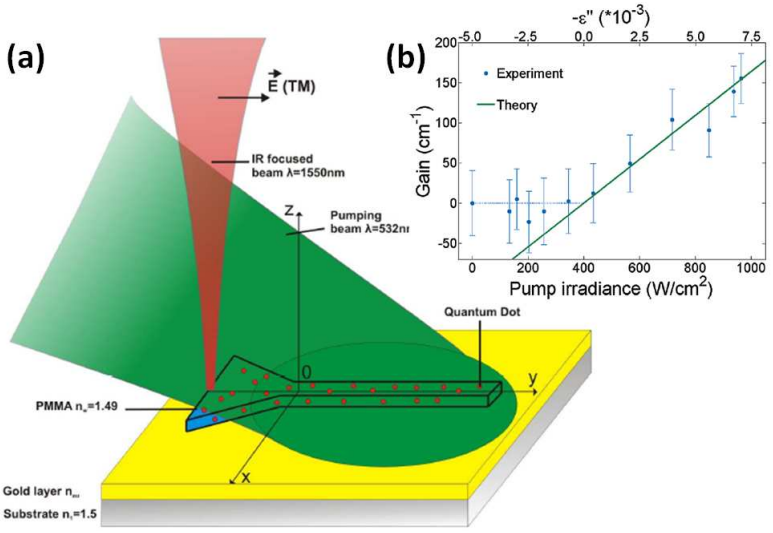


Figure 1.11: (a) QDs doped DLSPP polymer waveguide excited by a TM-polarized infrared laser beam at $\lambda$=1.55 $\mu$m from the tapering section and illuminated completely with a 532 nm laser to activate the QDs to their excited state (c) Measured (blue dots) and calculated (green line) optical gain coefficients versus pump irradiance demonstrated as a function of the imaginary part $\epsilon''$ of the DLSPPW dielectric constant (Image adapted from ref. [57] by permission from American Chemical Society © 2009)

The first direct measurement of the gain on a long-range SPP mode was achieved by Leon and Berini [19]. This experiment was performed on a symmetric gold-stripe plasmonic waveguide with dimensions 20 nm thick, 1 $\mu$m wide and lying on a 15 $\mu$m-thick $SiO_2$, covered by $\sim$ 100 nm thick gain medium containing optically pumped IR140 dye molecules in a solution (see fig.1.12). While LRSPPs was exciting (probing) through butt-coupled optical fibers at $\lambda_e = 882$ nm, the dye molecules were pumping from the top at $\lambda_p = 808$ nm with 20 mJ $\mathrm{cm^{-2}}$ for 8 ns pulses. The mode power gain measured in terms of the amplifier length, $l_a$ was found to be 8.55 dB $\mathrm{mm^{-1}}$(see fig.1.12). This type of amplifier provided not only large spontaneous emission but also caused a reduced amount of spontaneous emission noise, namely 6.3 dB.

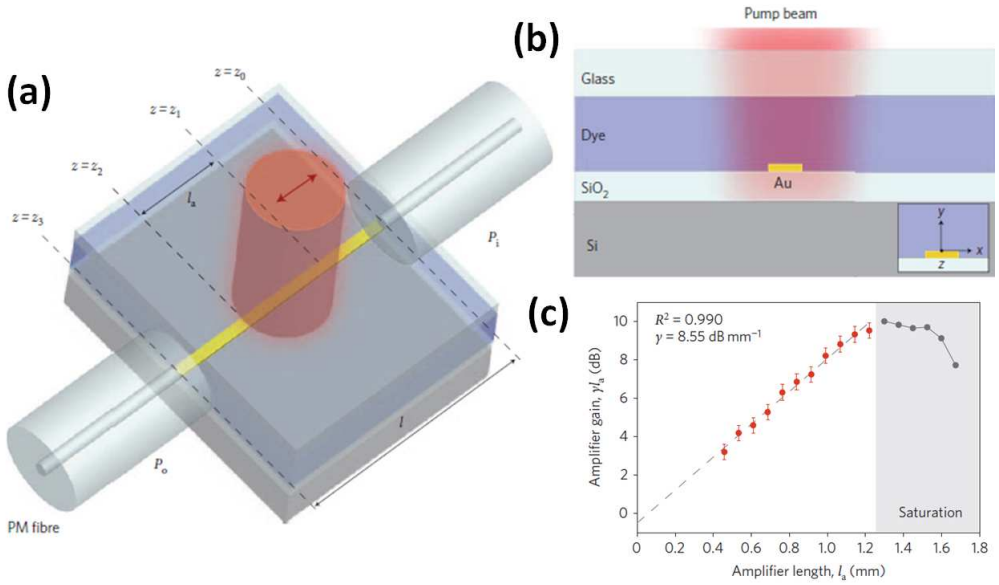


Figure 1.12: (a) The plasmonic waveguide structure employed for the measurement of the long-range SPPs amplification. While the probe signal was let in (out) to (from) the system by end-fire coupling technique using polarization-maintaining fibres, the incident pump light for the amplification with a polarization shown by the red arrow was applied at a normal incident onto the sample center (b) Cross-section of the structure employed for the amplification (c) The measured amplifier gain, $\gamma l_a$, in terms of the amplifier length, $l_a$, was displayed where a linear fit matching with the measured data shown 8.55 dB mm$^{-1}$ mode power gain of LRSPPs. (Image adapted from ref. [19] by permission from Macmillan Publishers Ltd. © 2010)

## 1.3.2 Intermediate field confinement

### 1.3.2.1 Dielectric-loaded surface plasmon polariton waveguides (DLSPPWs)

Recent years, *dielectric-loaded surface plasmon polariton (DLSPP)* components especially waveguides have also attracted more interest due to higher refractive index which cause to bound SPP modes inside the dielectric structure. This provides not only high confinement of SPPs but also decreasing of edge-scattering losses in DLSPPW configurations. Besides, dielectric structures allow to be tailored their optical properties by means of thermo, electro or optical activation technique which is a very crucial feature in the context of active plasmonics.

One of the first works was only aimed to realize some basic optical functionalities such as focusing and refraction by the help of surface plasmons supported by dielectric structures on top of a gold film [58]. The effect of the top dielectric ridge on the SPPs dispersion relation was considered theoretically and numerically. SPPs propagation sustained by $SiO_2$ dielectric structure was also demonstrated experimentally via leakage radiation and PSTM characterizations. Only one year later, the first SPP waveguides comprised of $SiO_2$ stripes on gold film were reported [59]. In this work, the straight waveguides with different widths from 5 $\mu$m down to 100 nm, bent waveguides and crossing of two waveguides were investigated by comparing with the effect index method which showed a good agreement with experimental results. Low loss in waveguide bends and no crosstalk through waveguide crossings were

observed. Besides, multimode and monomode behaviors were found depending on the widths of the straight waveguides.

Waveguiding properties of DLSPPWs structures were investigated in detail through two methods; the effective-index method (EIM) and the finite element method (FEM) [60]. Effective index, confinement and propagation length of DLSPPWs mode were computed in terms of different widths and thicknesses of a polymer ridge deposited on a gold film at telecom wavelengths. It was found that DLSPPWs single-mode could be achieved when ridge thicknesses were smaller than ∼630 nm and widths were below ∼655 nm. In contrast to the conventional trade-off between confinement and propagation length, high lateral confinement could be sustained by adjusting convenient ridge thickness, even when propagation length increasing.

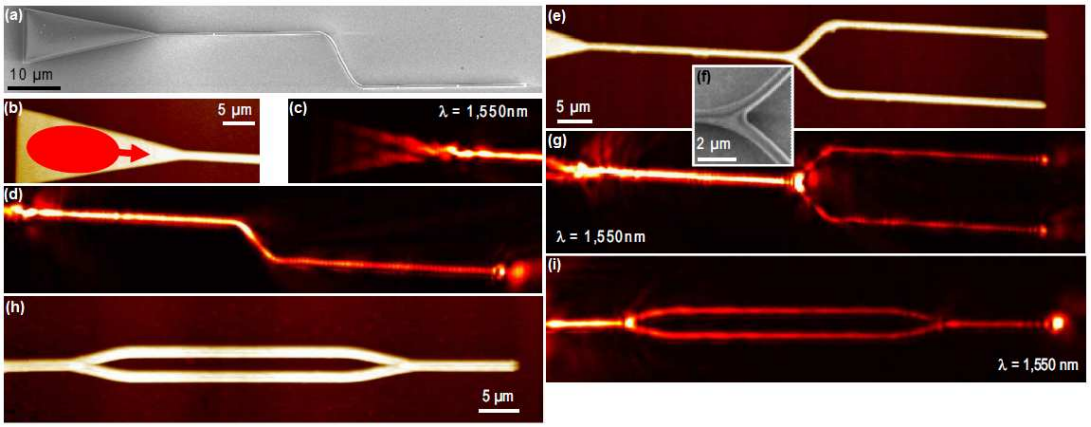


Figure 1.13: (a) SEM image of a taper connected 10 $\mu$m-long-S bend with an offset of d=10 $\mu$m (b) Topographical image of the taper in which SPPs excitation launched (c) Near-field optical image of the taper while excited SPPs was propagating through the taper (d) Near-field optical image of SPPs propagation in 10 $\mu$m-long-S bend with a 5 $\mu$m offset (e)[(g)] Topographical [Near-field optical] image of a 10 $\mu$m-long-Y splitter with an arm separation of 10 $\mu$m (f) SEM image of the junction area (h)[(i)] Topographical [Near-field optical] image of a 45 $\mu$m-long-Mach-Zehnder interferometers with an arm separation of 3 $\mu$m where SPPs propagates from left to right (Image adapted from ref. [61] by permission from OSA © 2008)

DLSPPW based plasmonic components such as bends, splitters and Mach-Zehnder interferometers were also demonstrated [61]. Characterization of the fabricated components was performed by scanning near-field optical microscope (SNOM) and the performances were evaluated by comparing experiment results with the results of full vectorial three-dimensional finite element simulations. It was found that for the S bends, the pure bend loss was very small (<10%) if the offset was smaller than 3 $\mu$m otherwise the main contribution of losses arose from radiation out of the bend if the offset was bigger than 6 $\mu$m (fig.1.13(a),(d)). Y-splitters functioned as a 50/50 splitting of DLSPPW mode, however, they experienced transmission losses due to the radiation out of the junction area (fig.1.13(e),(f),(g)). The transmission through the 45-$\mu$m-long Mach-Zehnder interferometer was found to be ∼20% and the propagation loss of the DLSPPW mode along the Mach-Zehnder interferometer constituted 74% of the total losses (fig.1.13(h),(i)).

Several characterization and numerical techniques were proposed in order to understand

guiding properties of DLSPPWs. Leakage radiation microscopy (LRM) is one of the characterization methods which provide direct measurement of both the real and imaginary parts of the effective index of the guided mode by observing both image plane and fourier plane (see fig.1.14) [62–64]. As a numerical technique, the differential method was demonstrated to be an efficient numerical method for the investigation of DLSPPWs which exhibited a fair agreement with other complex methods such as FEM [65].

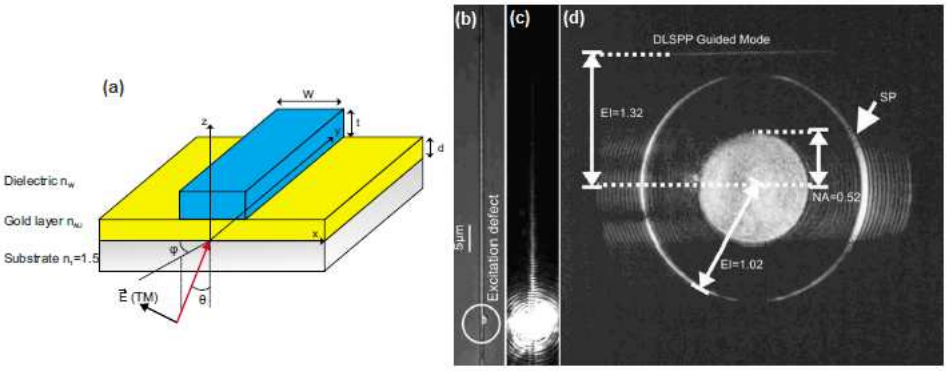


Figure 1.14: (a) Sketch of a DLSPPW structure (b) Optical micrograph of a straight DLSPPW configuration comprised of PMMA ridge of finite width and thickness deposited on a gold film (c) Image plane of leakage radiation microscopy (LRM) of SPPs propagation along the DLSPP waveguide (d) Fourier plane of leakage radiation microscopy (LRM) of SPPs propagation by which the effective index of both DLSPP guided mode and Au/air SPP mode could be deduced as indicated by arrows (Image adapted from ref. [62] by permission from the American Physical Society © 2008)

The active control of SPPs propagation along DLSPPWs has also been investigated in diverse works. The principle mechanism is that one of the interfaces is employed as an active part whose refractive index is altered by means of an external excitation or stimulus that causes to change effective index of the SPPs propagating mode. This stimulus may be provided by one of the effects through all-optic, thermo-optic, electro-optic or magneto-optic.

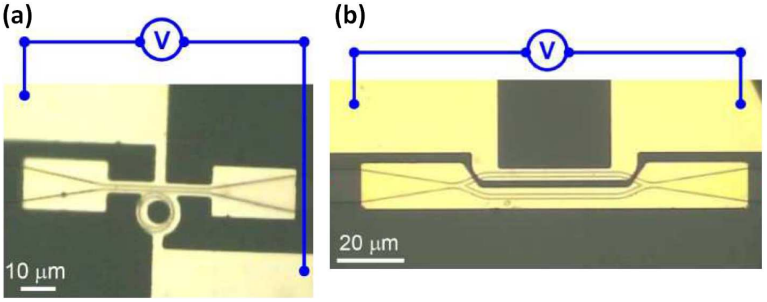


Figure 1.15: (a) Optical microscope image of a waveguide-ring resonator (WRR) modulator connected with electrodes shown schematically (b) Optical microscope image of a Mach-Zehnder interferometer (MZI) modulator connected with electrodes shown schematically (Image adapted from ref. [16] by permission from OSA © 2010)

In an initial study on DLSPPWs was demonstrated that fiber-coupled DLSPPW components, namely Mach-Zehnder interferometers (MZIs), waveguide-ring resonators (WRRs) and

directional couplers (DCs) could be actively controlled via thermo-optic effect through electrical heating of the same gold stripes sustaining DLSPP mode at telecom wavelength (see fig.1.15) [16]. It was found that the modulation depth of the MZIs- and WRRs-based components could go beyond 20% and the rerouting efficiency of the DCs switches was obtained to be $\sim$30%.

Recently, it was reported that PMMA may not be an appropriate material as a dielectric loading part of DLSPPW with a lower thermo-optical coefficient ($\partial n/\partial T$ =-1.05$\times 10^{-4} K^{-1}$) for fabricating thermo-optically controlled plasmonic components [66]. Subsequently, the same research group demonstrated a 2$\times$2 efficient and compact thermo-optic DLSPPW switch composed of a high thermo-optic coefficient polymer, cycloaliphatic acrylate ($\partial n/\partial T$ =-3$\times 10^{-4} K^{-1}$) which could operate at telecom wavelengths [67]. The working principle of this thermo-optic switch was based on the interference of the fundamental plasmonic and the second-order (photonic) mode, namely dual mode interference (DMI) mode which gave an opportunity to decrease insertion losses because of the low-damping feature of the photonic mode.

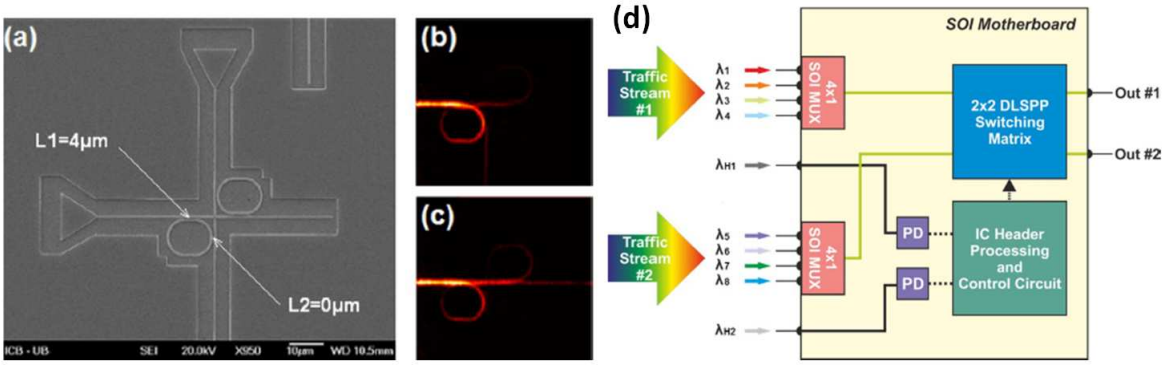


Figure 1.16: (a) SEM image of the router core element: a novel dual-ring DLSPP add/drop filter component (b) [(c)] Leakage radiation microscope (LRM) image of guided SPPs signal along the drop [through] port (d) A 2x2 silicon-plasmonic router architecture layout (Image adapted from ref. [68] by permission from IEEE © 2011)

Furthermore, it was realized a 2x2 silicon-plasmonic router architecture having 320 Gb/s throughput capability for optical interconnect applications [68]. This fabricated router was based on a novel dual-ring DLSPP component serving as a 2x2 switch, which was integrated onto a silicon-on-insulator (SOI) photonic motherboard (see fig.1.16). The router setup included two 4x1 SOI multiplexing circuits (SOI-MUX) whose were employed to support 40 Gb/s NRZ channel multiplexing with a 100 GHz channel spacing. An attractive coupling, butt-coupling design, between DLSPP switch and SOI circuitry was achieved with low losses, 2.6 dB. And the final router design could perform a successful 2x2 routing of two incoming 4-wavelength NRZ (Non return to zero) signals at 40 Gb/s data traffic by which a promising architecture with an effective footprint and a reduced power consumption has been demonstrated for next generation optical interconnects.

#### 1.3.2.2 Wedge waveguides

Wedge shaped metal waveguides have also been investigated as plasmonic waveguides owing to providing smaller modal size and long propagation distance. Pile et al. reported a numerical and first experimental observation of SPPs guiding along a triangular metal wedge [69]. Dispersion and dissipation of the wedges were investigated by finite-difference time-domain algorithm. Plasmons were excited by end-fire coupling and detected by near-field optical probe. It was found that wedge plasmon (WP) mode could not be sustained if the wedge angle was greater than a critical angle ($\simeq$ 102° for a silver wedge at $\lambda$= 0.6328 $\mu$m). Besides, a strong field subwavelength confinement and sufficient propagation distance proved that WP might be a promising structure for subwavelength plasmonic waveguiding. In another study, it was demonstrated that a sharp triangular metal wedge on a dielectric substrate allow to achieve efficient plasmon nanofocusing [70].

Moreno et al. demonstrated a theoretical investigation of the guided modes of wedge plasmon polaritons (WPPs) at telecom wavelengths [71]. The modes of WPPs were found to had strong field confinements with similar propagation lengths with respect to the other subwavelength counterpart configurations (see fig.1.17). Besides, they showed that it was possible to realize nanofocusing of SPPs by only altering geometrical dimensions of the wedge structure, and so, all above-mentioned results concluded that WPPs might be a good candidate for subwavelength guiding and focusing of SPPs.

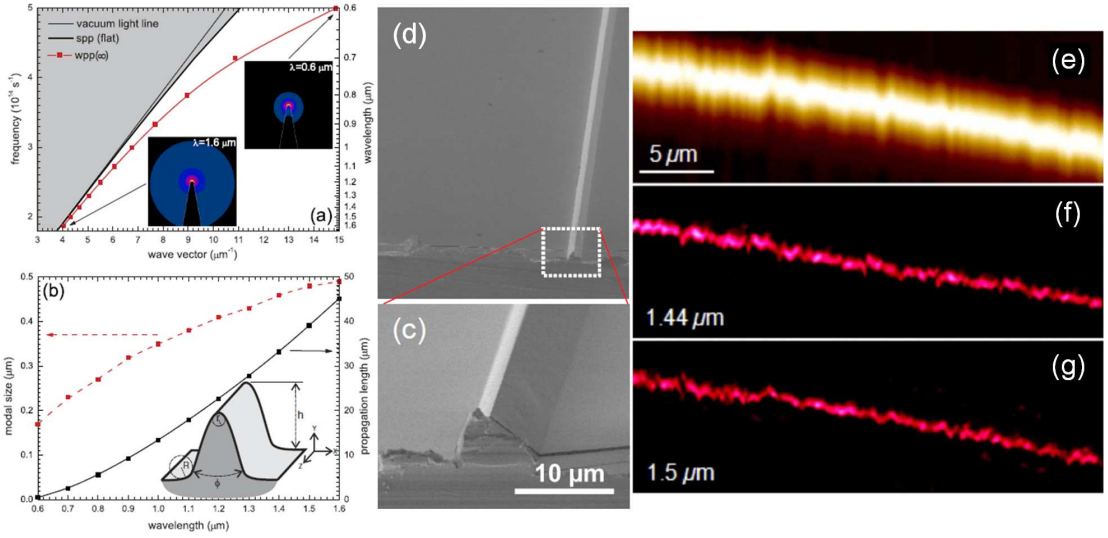


Figure 1.17: (a) The dispersion relation of WPP in comparison with SPPs' one on flat surface and light's one in vacuum (b) Modal size and propagation length of WPP at wavelengths between 0.6 - 1.6 $\mu$m (c)-(d) SEM image of a fabricated gold wedge waveguide with dimensions of 8.5 $\mu$m-wide and 6 $\mu$m-high (e) Topographical image of the wedge (f)-(g) SNOM images of WPP propagation for TM polarization at two different wavelengths (Image adapted from ref. [71] by permission from the American Physical Society © 2008 and from ref. [72] by permission from OSA © 2008)

At the same year, the experimental demonstration of subwavelength plasmon-polariton guiding at telecom wavelengths along triangular metal wedges was reported by Boltasseva et her co-workers [72]. The gold wedge waveguides were fabricated by standard UV lithogra-

phy process which allow to extend this process for mass-production (see fig.1.17(b)-(c)). The SNOM characterization of wedge plasmon-polaritons (WPPs) along a triangular 6-$\mu$m-high and 70.5°-angle gold wedge showed not only high confinement feature of the mode, mode width $\sim$ 1.3 $\mu$m, but also possibility of WPP guiding with lower losses at 1.43-1.52 $\mu$m wavelengths.

#### 1.3.2.3 Hybrid plasmonic waveguides

Hybrid plasmonic waveguides are aimed to merge useful properties of photonics and plasmonics on the same structure in order to achieve efficient waveguiding with subwavelength confinement and lowest losses. So far, it has been proposed various hybrid plasmonic waveguides.

A hybrid waveguide merging dielectric waveguiding with plasmonics first was demonstrated by Oulton et al. [73]. It was composed of a metal surface and a dielectric nanowire which were separated from each other by a nanoscale gap (see the inset of fig.1.18a). By adjusting diameter of the dielectric nanowire and the gap distance, it was possible to achieve subwavelength confinement ($\lambda^2/400\, to\, \lambda^2/40$) and long-range propagation (40 - 150 $\mu$m) due to the hybridization of the photonic mode with plasmonics one which leads capacitor-like energy storage throughout the gap. This new approach was not only suitable integration for semiconductor fabrication techniques but also enabling to realize subwavelength devices with smaller mode size and large propagation lengths as well as providing to be applied waveguide loss compensation techniques.

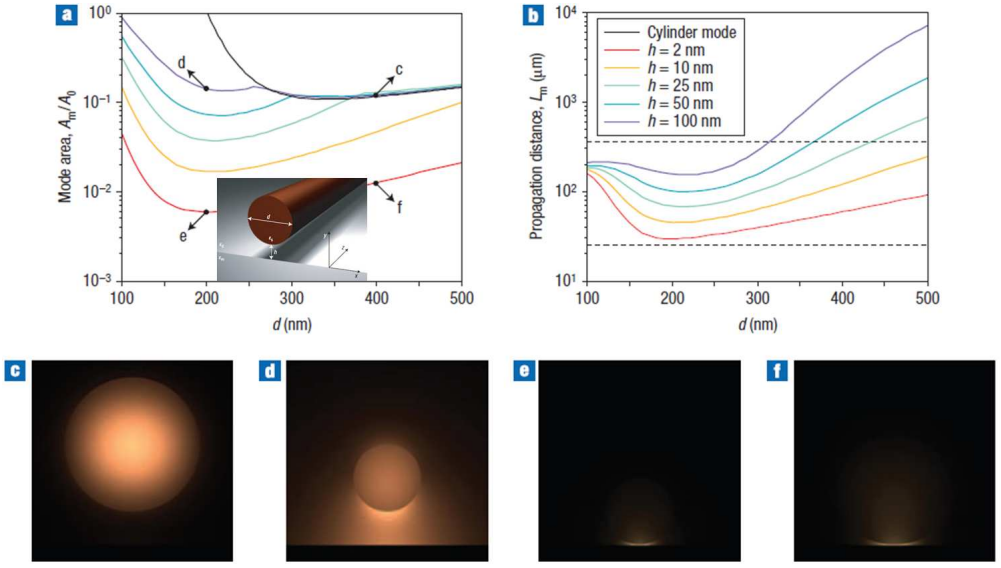


Figure 1.18: (a) Mode area as a function of dielectric waveguide diameter, d, and gap distance, h, (b) Propagation length of the guided mode as a function of dielectric waveguide diameter and gap distance (c)-(f) Electromagnetic field distribution of the hybrid mode for (d , h) = (400,100), (200,100), (200,2) and (400,2) [nm] respectively which all were pointed out on the curves of the panel (a) (Image adapted from ref. [73] by permission from Macmillan Publishers Ltd. © 2008)

Briggs et al. reported efficient coupling of light between dielectric-loaded plasmonic and

silicon photonic waveguides [74]. They demonstrated coupling of light in and out to polymer-on-gold DLSPP waveguides efficiently and then end-coupling of the waveguide to silicon-on-insulator (SOI) waveguides with 79±2% transition efficiency at telecom wavelengths. Besides, it was determined SPPs propagation distance as 51±4 $\mu$m due to low propagation losses at $\lambda$=1550 nm. They also showed efficient coupling to whispering-gallery modes in plasmonic ring resonators with a quality factor of 180±8. These promising results indicated that this type of plasmonic waveguides could be merged with optical ones in order to realize real plasmonic circuitry.

### 1.3.3 High field confinement

#### 1.3.3.1 Plasmonic nanowires

The diffraction limit in classical optics stands as an inevitable obstacle while decreasing dimensions of integrated-optical devices. However, SPPs enable to us to overcome this limitation by means of subwavelength confinement along the metal-dielectric interface. Nanowires play a critical role in here by sustaining subwavelength waveguiding of SPPs waves.

Nanowires practically can be either microfabricated via electron-beam lithography corresponds to polycrystalline nanowires or synthesized by chemically corresponds to single-crystalline nanowires [75]. Single-crystalline nanowires compose of well develop crystals and surfaces, thus they exhibit remarkably less damping than polycrystalline ones [76]. However, the integration of this type nanowires to any photonic or plasmonic interfaces is a challenging task due to their production method. On the other hand, polycrystalline nanowires have a strongly damping characteristics due to scattering at grain boundaries. Recently, a spectroscopic study demonstrates that the damping of polycrystalline silver and gold nanowires can be reduced by using quartz support instead of ITO-glass one [77]. Despite significant damping in polycrystalline nanowires, they are generally more preferred to fabricate as subwavelength plasmonic elements because of compatibility and flexibility in the integration methods and facility of the fabrication techniques. Now, we are going to present several works that have been demonstrated so far.

First theoretical pioneer work was performed by Takahara et al. who considered the guiding properties of the light through one-dimensional optical waveguides (nanowires) which were composed of a metal core and a dielectric cladding [78]. They demonstrated that it was possible to guide strongly confined one-dimensional optical beams (SPPs) within a nanowire whose diameter was thinner than the wavelength of free-space at the visible and near-infrared regions.

Very soon after, Weeber et al. investigated theoretically the propagation of plasmon polaritons along metallic nanowires by using the Green dyadic technique [79]. It was shown that while illuminating the end of a nanowire by a proper polarization, the local excitation could be confined and guided by means of localized surface plasmons along a few micrometers long nanowires. Furthermore, the single-particle excitation was achieved through nanowires which gave rise to an impressive switching character by altering incident wavelength.

These and other similar theoretical studies paved the way for experimental researches. Not too late only after 1 year later, Dickson et al. demonstrated unidirectional propagation of SPPs along metallic nanowires whose dimensions were 20 nm diameter and $<$10 $\mu$m long [80]. First, SPPs propagations were shown along Au and Ag nanowires by local optical excitation at

the visible wavelengths and then these results were exploited to obtain a undirectional SPPs propagation through a electrosynthesized Au/Ag heterojunction nanowire.

To determine dispersion relation of nanowires was a complicated work since the small dimensions of the nanowires did not permit to make measurement easily by using attenuated total reflection spectroscopy. Schider et al. proposed an alternative technique, namely conventional extinction spectroscopy, by which they could measure SPPs dispersion relation of Ag and Au nanowires of a fixed cross section and different lengths which had been fabricated by e-beam lithography [81]. It was shown that the dispersion relation of nanowires was found to be similar to that of the planar metal-dielectric interface one except the upper limiting frequency of SPPs excitation was smaller. Besides, SPPs propagation along Ag nanowires was found to be slower than that of the planar metal-dielectric interface one.

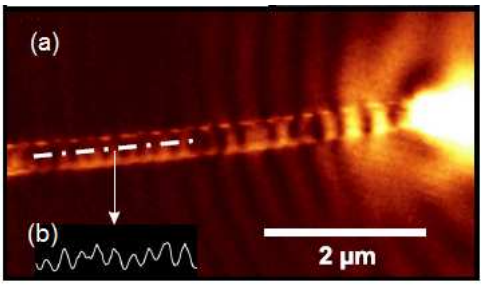


Figure 1.19: (a) Scanning near-field optical microscopy (SNOM) image of the distal end of the 18.6 $\mu$m long silver nanowire in which the SPPs propagation is scattered into light. (b) The light spectra along the 2 $\mu$m long cross-cut of the same nanowire (through the dotted-line) (Image adapted from ref. [76] by permission from the American Physical Society © 2005)

Nanowires sustaining SPPs may also serve as surface plasmon resonators under appropriate conditions. It was demonstrated that chemically prepared silver nanowires with $\sim$ 100 nm cross-section and up to 20 $\mu$m length could provide a large propagation length at about 10 $\mu$m due to the well develop crystals and surface structures [76]. Besides, their end face reflectivity was found to be 25 % at the same wavelength (785 nm). These two important properties allowed to exploit the nanowires as efficient surface plasmon Fabry-Perot resonators (see fig.1.19). Moreover, the wavelength of the SPPs along these nanowires was seen to be reduced to half value of the exciting light. This result proved again that subwavelength mode could be achieved by means of plasmonic nanowires.

Maybe the most difficult obstacle is efficient SPPs excitation through nanowires. Due to the ohmic and radiation losses and also quickly accessible cutoff width of the nanowires, it is not very easy to achieve highly confined nanowire modes. Verhagen et al. demonstrated that the SPPs excitation of highly confined nanowire modes can be obtained by means of adiabatic mode transformation [82]. A gold waveguide on BK7 glass substrate which composed of a hole array and whose width narrowed through a taper of 20 $\mu$m length in order to be connected to a nanowire of 40 $\mu$m length was fabricated by means of e-beam lithography and reactive ion etching (see fig.1.20). Due to the inconvenience of air-guided modes for adiabatic coupling to the nanowire mode, the SPPs excitation was launched directly at the substrate side (gold/glass) via the hole array. The excited SPPs started to propagate first along the waveguide and then gradually evolves to the nanowire mode as the width of the stripe decreased along the

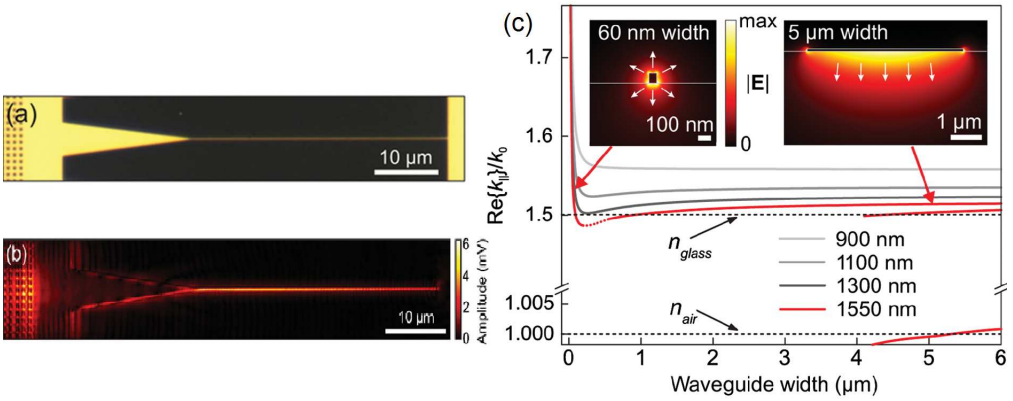


Figure 1.20: (a) Optical microscope image of the waveguide structure (b) The SPPs amplitude which was measured by phase- and polarization-sensitive near field microscopy (c) The normalized wave vector ($n_{eff}$) of the SPPs was calculated in terms of the waveguide widths at different wavelengths. In the insets, the electric field amplitudes of 60 nm and 5 $\mu$m widths of the waveguide at telecom wavelengths 1550 nm were demonstrated (Image adapted from ref. [82] by permission from the American Physical Society © 2009)

taper which determined the degree of the adiabaticity namely the efficiency of coupling to the nanowire mode. As can be seen in the fig.1.20, at large widths the eigenmodes of the waveguide were mostly localized either in the air or in the glass medium due to the asymmetry of the interface. But as the width decreases, only one mode existed and encompassed subwavelength cross-section of the nanowires that was identified as nanowire mode in which the transverse electric field at opposite sides of the waveguide had opposite sign. This mode showed a characteristic antisymmetric nature in which the surface charges around the nanowire had equal sign. It should be also noted that the normalized wave vector (or $n_{eff}$ in here) crossed the substrate light line as the width decreased. These results suggested that suchlike structures may serve an efficient coupling element to excite nanowire SPPs by means of adiabatic mode transformation.

#### 1.3.3.2 Gap plasmon polaritons

One of the first pioneer works was demonstrated by Pile et al. where a numerical and first experimental investigation of a novel 2D strongly localized plasmon modes guided by a rectangular nanogap was presented in a thin metal film [83]. By using finite-difference time-domain (FDTD) method, dispersion, dissipation and propagated field intensity were examined. Moreover, gap plasmon mode was excited by using end-fire coupling and scattered from the edge by which images could be detected and recorded by charge coupled device (CCD). It was concluded that the gap plasmon mode would be a promising option for all optical nanocircuits due to high confinement, reasonable propagation length and easy fabrication technique.

Neutens et al. presented remote electrical detection of gap plasmons propagation inside a MIM (metal-insulator-metal) waveguide [84]. By using a nanoscale integrated GaAs MSM (metal-semiconductor-metal) detector attached with a MIM waveguide, strongly confined gap plasmon mode could be detected and examined (see fig. 1.21(a)-(b)). According to the Monte Carlo simulations, the RC-limited bandwidth of this device was found between 240 GHz to

909 GHz depending on the waveguide geometry. Two dimensional photocurrent maps and polarization dependent SPPs dispersion in the waveguide were also demonstrated. The electrical detection of the confined SPPs showed that $e^{-1}$ decay lengths were found to be 3.5 $\mu$m and 9.5 $\mu$m for wavelengths of 660 nm and 870 nm respectively. In summary, this type of integrated MSM detector in conjuction with MIM waveguide was believed to be a suitable and powerful device for electrical detection of strongly confined gap plasmons which might play a critical role in order realize novel active plasmonic components.

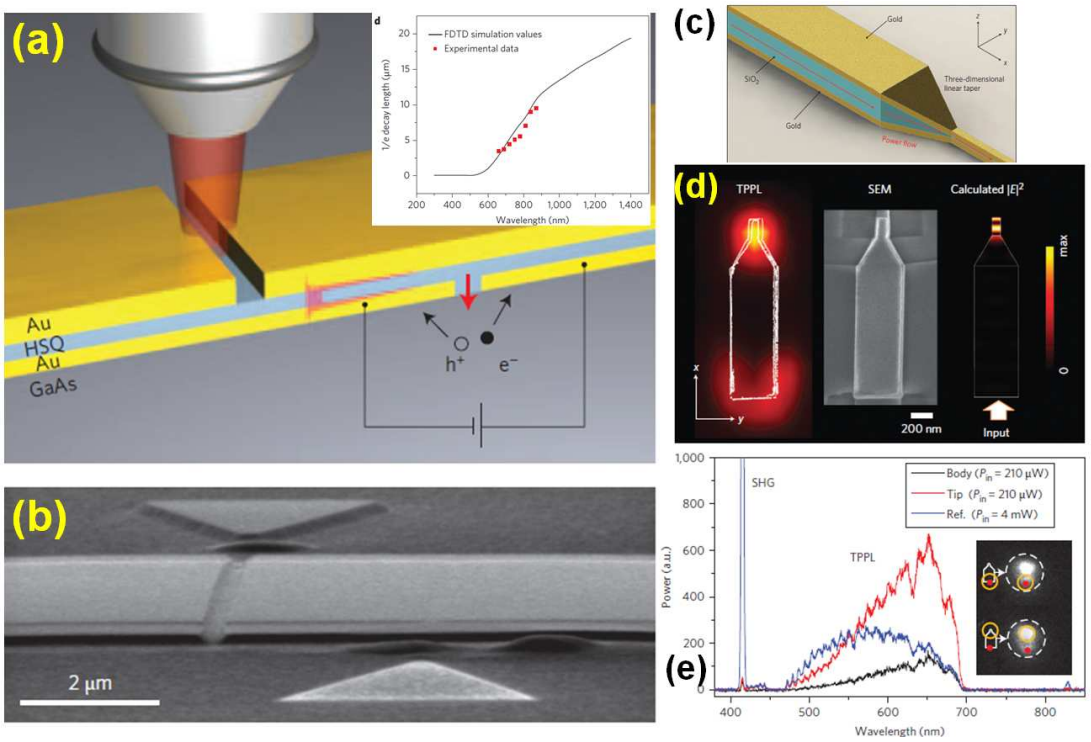


Figure 1.21: (a) Schematic representation of the MIM waveguide in conjuction with the integrated MSM detector. (Inset): $e^{-1}$ decay length ($\mu$m) versus wavelength (nm) where the experimental values were compared with FDTD simulation results (b) SEM image of the fabricated device where two arrows indicated excitation and detection slit respectively (Image adapted from ref. [84] by permission from Macmillan Publishers Ltd. © 2009) (c) Schematic illustration of a three-dimensional nanoplasmonic photon compressor (NPC) with a 3D taper connected to a MIM waveguide (d) Field intensity map of the fabricated sample characterized by TPLL image, SEM image of the characterized sample and $E^2$ intensity profile of the corresponding fabricated sample calculated by simulations (e) Detected emission spectra of the 3D NPC device on the body (black curve), on tip (red curve) and on a smooth gold film for reference (Image adapted from ref. [85] by permission from Macmillan Publishers Ltd. © 2012)

Recently, a challenging task, nanofocusing of light, has also been achieved by the help of gap plasmon waveguide. Choo et al. demonstrated a highly efficient, on-chip 3D nanoplasmonic photon compressor (3D NPC) [85]. It was composed of $Au-SiO_2-Au$ gap plasmon waveguide which was linearly tapered with a well fabricated three dimensional taper functioning to minimize high losses during performing nanofocusing where intrinsic scattering and resistive absorption losses were taken into account in this process (see fig. 1.21(c)-(e)). Critical

taper angle and required distance were extracted from the finite-difference time-domain (FDTD) simulation results. It was found that a 3D tapering could be possible while focusing of 830 nm wavelength light into a 235 $nm^2$ area below 3 dB losses and with 3.03104 intensity enhancement. Besides, the fabricated device was characterized by a two-photon photoluminescence (TPPL) setup with a electron-multiplying charge-coupled device (EMCCD) and a spectrometer where it was found 21.3 dB (74% transmittance) coupling efficiency and 400 intensity enhancement in a 14x80 $nm^2$ cross-sectional area. As a result, this 3D NPC device had great potential and could be useful for implementing on-chip nanoscale photonic/plasmonic applications.

#### 1.3.3.3 Slot waveguides

Liu et al. demonstrated one of the pioneer studies in slot plasmonic waveguides where a novel SP waveguide structure was realized by etching a small trench through a metallic thin film lying on a silica substrate [86]. Highly confined mode properties of SP along the waveguide was investigated and the necessity of a polymer upper-cladding with a refractive index close to the silica's one on top of the thin metal film was emphasized. Moreover, the coupling conditions between two closely positioned waveguides as well as 90° bend waveguides were discussed numerically which shown that highly integrated and sharp bend waveguides could be possible to realize by the proposed structures only with a reasonable separation distance and bending radius. Easy fabrication of the waveguide structure could also be mentioned as an another advantage with respect to the other types of SPs waveguides for highly integrated plasmonic circuits.

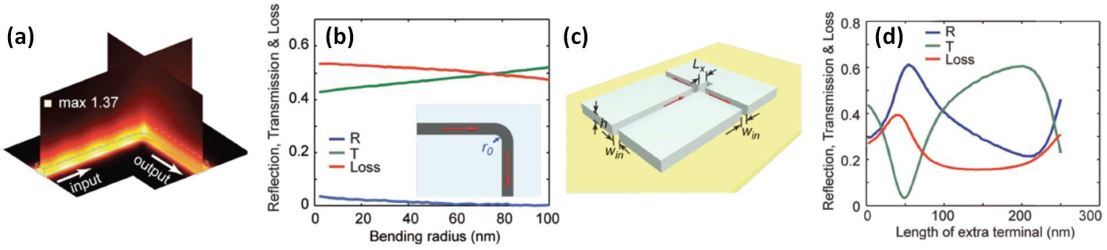


Figure 1.22: (a) Full-wave simulation of normalized magnetic field distribution on a 90° bend with a 50 nm bending radius of a 3D MSM slot waveguide (b) Obtained results of reflection, transmission and loss versus bending radius on a 90° bend (c) Schematic representation of a T-splitter with an extra terminal ($L_x$) by using a 3D MSM slot waveguide (d) Obtained results of reflection, transmission and loss versus the length of an extra terminal on a T-splitter (Image adapted from ref. [87] by permission from John Wiley and Sons, © 2010 WILEY-VCH Verlag GmbH & Co. KGaA, Weinheim)

At the same year, Veronis et al. also investigated numerically the existence of bound optical mode sustained by a slot waveguide within a thin metallic film deposited on a substrate [88]. The novelty of this slotline was the dimension much smaller than the wavelength of interest. They found that the slotline could provide a fundamental bound mode with a modal size almost entirely dominated by the near field of the slot for a wide frequency range. This modal size was so small than the incident wavelength that was even sustained close the mode of the light line in the surrounding media. Furthermore, it was shown that the group velocity of

this mode was close the light one's in the substrate and the propagation distance of the mode was found to be tens of micrometers at the optical communication wavelength.

Dionne et al. demonstrated a numerical investigation on wavelength dependent properties of plasmon slot waveguides [89]. The dispersion relation, wavelength dependent propagation and energy density decay was discussed on $Ag/SiO_2/Ag$ MIM waveguides with thickness ranging 12 nm to 250 nm. Although it was found the same modes below 100 nm core thickness ($SiO_2$) in IMI structures, namely symmetric and antisymmetric modes, they did not exhibit the same characteristics. In symmetric mode, the surface plasmon momentum did not always go beyond photon momentum even was found effective indices as low as n=0.15 for thicker films such as d$\sim$50 nm. In antisymmetric mode, a cutoff was observed below 20 nm core thickness. In the range of visible to NIR wavelengths, SPPs propagation length could achieve as large as tens of microns with a fields confinement only around 20 nm core width. If the core thickness was increased, the propagation length would increase as well with the same localization and besides, conventional waveguide mode were not observed until 100 nm core thickness.

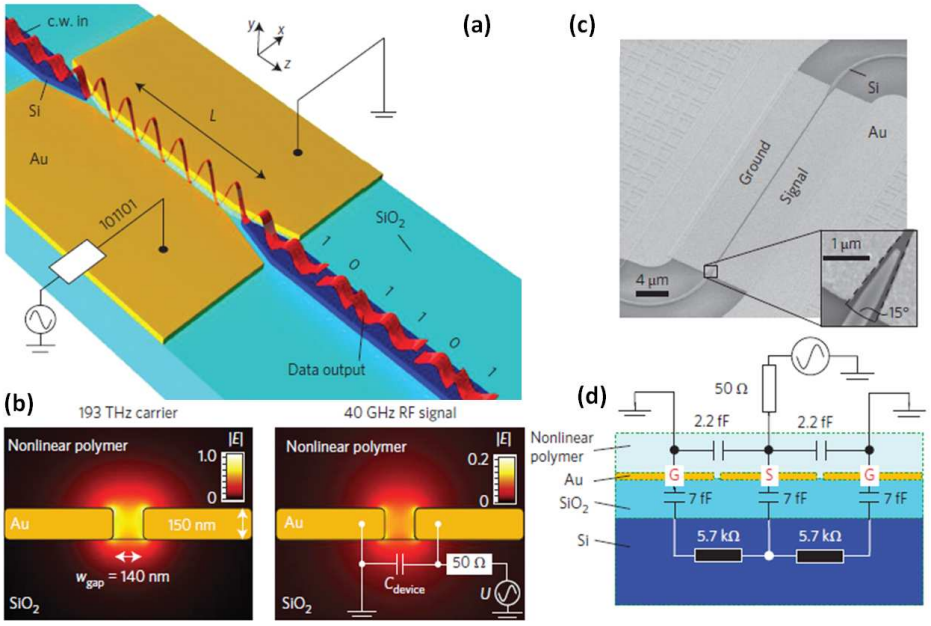


Figure 1.23: (a) Schematic representation of the plasmonic phase electro-optic modulator based on the Pockels effect of a nonlinear polymer realized by using plasmonic slot waveguide (b) Cross section and electric field mode profiles along the slot waveguide (c) SEM image of the fabricated device just before coating with nonlinear-polymer (d) Cross section and lumped element model of the device used for the electrical characterization (Image adapted from ref. [90] by permission from Macmillan Publishers Ltd. © 2014)

Cai et al. presented a numerical investigation of various passive elements by using 3D slot waveguides for routing and manipulation of SPPs at $\lambda$=850 nm (see fig. 1.22) [87]. First, they investigated fundamental characteristics of a straight slot such as mode index, loss factor and energy confinement and named as a metal-dielectric-metal (MDM) slot waveguide due its silver-dielectric-silver structure. Then, they developed several passive elements like bend,

mirrors and T-splitters. In sharp bends with 90° corners leading excessive losses could be minimized by means of eliminating power reflections and increasing transmission if a 50 nm bend curvature was used at the corner (see fig. 1.22(a)-(b)). However, such a bend curvature could not improve performance significantly of T-shaped splitters which were fundamental elements for power dividing and directional couplers. One solution was providing impedance matching of input and output slot widths which might cause challenge in fabrication step. They suggested an original solution which was introducing an extra terminal at the end of the input slot by which the interference behavior could be controlled through observing destructive interference at the input channel (see fig. 1.22(c)-(d)). In this work, they also analyzed the performance of X-junctions and a sandwich-type structure for the dielectric slots.

Recently, a first successful experimental demonstration of high-speed plasmonic phase modulator (ppm) using plasmonic slot waveguide was reported by Melikyan et al. [90]. Based on the Pockels effect of a nonlinear polymer where SPPs propagates inside a 140 nm slot between gold films could be realized as an ultra-compact electro-optical modulator operating at 40 Gbit/s (see fig. 1.23). This device had only 29 $\mu$m length and could work across 120 nm wide wavelength range at the center of 1550 nm wavelength which nearly covered all optical S, C and L bands. The modulation frequency was found to be flat up to 65 GHz and beyond. Besides, this device could operate under high temperatures up to 85°. Easy fabrication of this ppm could also be mentioned as another advantage. It was believed that this novel design could play a critical role for realizing future ultra-compact and CMOS-compatible on chip Mach-Zehnder and in-phase and quadrature phase plasmonic modulators which are required to perform amplitude modulations in plasmonic circuitry.

## 1.4 Conclusion

In summary, we have presented the new branch of nanophotonics, surface plasmon polaritons (SPPs) and its intriguing properties which is believed to be a promising candidate for combining the best properties of photonics and electronics at nanoscale dimensions. First of all, we have started with plasmon basics such as Drude model, dispersion relation, propagation length and penetration depth. Secondly, we have briefly explained surface plasmon modes on thin films as well as excitation and coupling techniques. After that, we have elucidated plasmonic waveguiding in three sections with respect to the confinement degree of SPPs within the metal film where we selected and focus on the most interesting works demonstrated so far in the literature.

In order to realize a real plasmonic circuitry for controlling and processing SPPs signals, it is absolutely required a large number of elements not only passive components (waveguides, couplers, etc.) but also active components (modulators, switches, etc.). Many works have been addressed for the demonstration of passive components since the birth of the plasmonics. However, active components, which are capable to generate, modulate and/or switch in other words - can control actively - SPPs waves through plasmonic interfaces, are still urgently needed to be able to develop and improve integrated plasmonic circuit technology especially at telecom wavelengths.

It is well known that SPPs propagates at the interface between metal-dielectric, so in an active component, one of these interfaces is employed as an active part whose refractive index (or dielectric, $\varepsilon_r$ = $n^2$) is altered by means of an external excitation or stimulus that causes

to change effective index of the SPPs propagating mode. This excitation can be provided by using one the effects of thermo-optic, electro-optic and magneto-optic. Thermo-optical (TO) effect is known as one of the efficient technique especially for dynamical control of plasmonic devices. This effect can be performed by means of either electrical or photo-thermal activation. Photo-thermal activation is more attractive and efficient due to offering possibility to tune parameters by using incident pump wavelength and polarization. It also proposes controlled local heating through focusing feature to avoid using high powers. Thus, our research will be based photo-thermal activation of various plasmonic devices.

So far, many works related dielectric based TO devices have been demonstrated where the dielectric part is used as an active part for modulation of SPPs propagation. However, to the best our knowledge, the role of the metal part in TO process has been rarely considered such that only several works has been shown when active part is originated from metal side. In particular, nanosecond (ns) photo-thermal activation has never been demonstrated in this context which is the key parameter for high bandwidth TO devices. Besides, TO effect and dynamics of metal is crucial for datacom applications which also needs to be investigated in detail.

The aim of this thesis is to clarify TO effects of metal and polymer by using photo-thermal activation supported by either CW or ns pulsed laser at telecom wavelengths. Our investigation takes place from low effective index to high effective index of SPP mode within the metal part. So, in this thesis, we first investigate the photo-thermal modulation of low confined SPPs propagation mode along the extended thin metal films and metal stripes at telecom wavelengths. Investigation on thermo-optical effects of metal allows us not only evaluate the contribution impact of metal heating in the context of non-linear plasmonics but also has great importance in the situation of optical pumping of a gain material for SPPs loss compensation while the pump beam absorbing by the metal. Secondly, we push forward these studies by evaluating dynamical characterization of the photo-thermal modulation of SPPs mode using a nanosecond pump laser. Especially, we demonstrate thermo-absorption of both metal and polymer loaded surface plasmon waveguide (PLSPPW) modes mediated by the temperature-dependent ohmic losses of the metal and the thermally controlled field distribution of the plasmon mode within the metal which all has not been investigated yet. Finally, we focus on the photo-thermal modulation of most confined SPP mode along the gold nanowires where the contribution of TO effects is expected much larger than the others. Besides, we demonstrate high bit rate (10 Gbit/s) signal transmission along the nanowires which is believed to the first demonstration of this type of plasmonic waveguides in short-range data transmission at telecom wavelengths.

Chapter 2

# Photo-thermal modulation of SPPs propagation on thin gold film at telecommunication wavelengths

## 2.1 Introduction

In order to benefit from the exciting properties of plasmonics efficiently, well-designed and compact plasmonics components should be fabricated. This is not only a fundamental demand but also is an inevitable reason for overcoming mismatch problem of scaling while integrating them into photonic and/or electronic devices. After the first observation of surface plasmon polaritons (SPPs) was performed, the propagation characteristics of passive plasmonic components have been investigated many times. Although there is an intense activity around the demonstration of dynamically controlled plasmonic devices, only very few works have been reported in this direction in the literature so far, mostly due to fundamental obstacles such as short propagation distances.

As stated before active functionality of plasmonic components can be provided by means of all-optic, thermo-optic, electro-optic or magneto-optical effects. In this thesis, thermo-optical (TO) effects based plasmonic waveguides will be investigated both numerically and experimentally in detail. Many thermo-optical plasmon-based devices have been reported in the literature recently [17, 67, 91–96]. In these works, the thermo-optical functionality is provided by a high thermo-optical coefficient of dielectric material whose refractive index (or dielectric constant $\tilde{\epsilon}$) is affected by a temperature change which in turn modifies the field distribution of the plasmon mode traveling at the dielectric/metal interface. As a result, in these configurations dielectric materials were thought to be an active part for SPPs modulation. Furthermore, thermal modulation of thin film SPPs excited in the Kretschmann-Raether configuration at visible frequencies has also been reported [97, 98]. However, so far, only little works has been done to assess quantitatively thermo-optical properties of thin film SPP modes at telecommunication wavelengths (1500nm-1600nm) [99], a spectral range of interest for datacom applications. At telecom wavelengths where gold dielectric function is dominated by free-electron contribution, an increase of the temperature leads to an increase of the ohmic losses through the increase

of the electron-phonon scattering rate. As a matter of fact, this process is not different from the increase of the static (dc) resistivity of metals for an increasing temperature [100]. The thermally-controlled losses in the metal lead to a SPP mode temperature dependent propagation length which can be used to evaluate the thermo-plasmonic properties of the metal of interest. By this way, it will not only be extracted thermo-optical coefficients (TOCs) of gold at telecom wavelengths but also thermo-plasmonic properties will be demonstrated by means of experimental and numerical results in this study.

The temperature dependent optical properties of noble metals have been investigated many times in the context of surface plasmon resonance (SPR) and/or metallic particles in dielectric matrices [101, 102] whereas no work so far has been reported about *photo-thermal modulation of SPPs propagation* at telecom wavelength according to the best of our knowledge. In this respect, the results we discuss in the following can be considered as a pioneering work.

This chapter is organized as follows. First of all, general aspects on optical properties and thermo-optical coefficients (TOCs) of metals are briefly given. Experimental part is considered next which consists of nanofabrication of samples, presentation of the characterization setup and measurements of the photo-thermal modulation of SPPs propagation in the continuous wave (CW) regime. Subsequently, we develop a numerical modeling based on the property of thermally-controlled ohmic losses and perform calculations in order to correlate the experimental results with the numerical ones. Later, we first extract thermo-plasmonic coefficient and then compute TOCs of gold film at telecom wavelengths. Moreover, we propose a figure of merit obtained from the measurements of a given SPP mode. Finally, the photo-thermal modulation of SPPs propagation is investigated in the nanosecond regime to analyze dynamics and test our TOCs provided by exchanging a CW laser with a Q-switched pulsed laser on the set-up. The obtained preliminary results will be followed by a more detailed investigation in the third chapter.

## 2.2 Optical properties of metals

The interaction of light with a metal is commonly described in classical electromagnetic light theory by means of the frequency dependent refractive index of the metal. Complex refractive index of a metal is composed of two terms; *refractive index* $n$ and *extinction coefficient* $\kappa$ (see equation 2.1). While refractive index describes how light waves are refracted when passing through a metal, extinction coefficient determines the amount of absorption loss of light propagation through a metal.

$$\tilde{n} = n + i\kappa \tag{2.1}$$

It is well known that the optical constants are dependent on the frequency of incident light waves. This means that though a metal may be transparent at a specific frequency, it may be opaque at an another frequency. Besides, the well-known relationship between complex refractive index and complex dielectric function in a non-magnetic medium is given by [103]:

$$\tilde{\epsilon} = \epsilon_r + i\epsilon_i \tag{2.2}$$

$$\tilde{\epsilon} = \tilde{n}^2 \tag{2.3}$$

$$\epsilon_r = n^2 - \kappa^2 \qquad \epsilon_i = 2n\kappa \tag{2.4}$$

Optical properties of noble metals (gold, silver and copper etc.) have received great interest because of their potential applications in applied physics. These metals are also of key interest for plasmonics. In all the following we will operate gold as the plasmonic metal of interest.

On the other hand, various dominant features play roles to determine exact value of the dielectric constant of gold. Two principle mechanisms are responsible for electronic transitions expressed as follows:

$$\tilde{\epsilon} = \epsilon_{intra} + \epsilon_{inter} \tag{2.5}$$

The dispersive dielectric constant of gold in the visible and near-infrared spectral range can be expressed as the sum of two contributions revealing the underlying physical phenomenons at the origin of the optical properties of this metal. As shown in the equation 2.5 the dielectric function is the sum of a contribution resulting from intraband and/or interband transition of electrons within the metal. Briefly speaking, the intraband contribution is defined as transitions of free-electron metal in which a free electron is excited from a filled state to an unoccupied state within the same band. It is a dominant mechanism at low optical frequencies especially the red and infrared (IR) spectral zone. The intraband contribution can be explained in a good way by the Drude model (see equation 1.9) [104]. On the other hand, the interband contribution is transitions of electrons from bound levels to the conduction band levels above the Fermi level. It is a dominant mechanism at higher optical frequencies particularly photon energies greater than 2 ev although the diminishing contribution of intraband contribution persists slightly at these frequencies [101].

## 2.3 Thermo-optical coefficients (TOCs) of metals

Optical properties of metals are known to be temperature-dependent. Several decades ago, thermo-optical properties of metals have been investigated in detail, mostly for noble metals [105–109]. When a metal is heated, many phenomenons contribute to the change of its dielectric function. A non-exhaustive list of these effects includes electron-electron scattering, electron-phonon scattering, electron-impurity/defect scattering, lattice expansion, shift of Fermi level and modification of Fermi-Dirac distribution [110]. The respective contribution of each of these channels may depend upon the metal, the incident photon frequency, the actual temperature and the amplitude of the temperature change. The temperature-dependent dielectric function of noble metals can be described in the framework of the Drude model at least for energies significantly below the interband absorption edge of the metal of interest [111–113].

The temperature dependence of noble metal optical properties has gained renewed interest recently in the context of surface plasmon modes excitation. Indeed, noble metals are to date the most appropriate materials used to investigate the properties of surface plasmon polaritons

(SPPs) sustained by either extended structures such as thin films or localized structures such as nanoparticles. The thermal properties of nanoparticles have been mainly investigated in the respect of localized heat sources relying on resonantly excited nanoparticles [114]. On the other hand, the impact of temperature onto localized surface plasmon resonances has also been investigated recently for single gold nanoparticles [115], gold nanoparticles embedded into a dielectric matrix [101,102] and closely packed gold nanorods forming a metamaterial [116]. For crystalline gold nanoparticles, a very good agreement of the experimental data with the results of the temperature-dependent Drude model has been found [115] whereas significant deviations from this model were noticed in the case of evaporated thin films [117, 118]. When SPPs is excited onto a thin film, its modes can be used for bio-sensing purposes and in this respect the role of temperature onto the sensitivity of SPPs based sensors has been investigated as well [119, 120].

Thermo-optical properties of metals are described by its thermo-optical coefficients (TOCs) that are specific constants for any material which determine the amount of variation in its complex refractive index by the temperature change (K). In fact, it is denoted by the sum of the temperature derivative of both refractive index and extinction coefficient such that:

$$\frac{\partial \tilde{n}}{\partial T} = \frac{\partial n}{\partial T} + i\frac{\partial \kappa}{\partial T} \qquad [K^{-1}] \tag{2.6}$$

By changing temperature, the new refractive index of any metal can be computed from a simple equation by using corresponding TOCs as follows:

$$\tilde{n}(T) = \tilde{n}(T_0) + (\partial \tilde{n}/\partial T)\Delta T \tag{2.7}$$

$\tilde{n}(T), \tilde{n}(T_0)$ and $\Delta T$ are the new refractive index at a temperature $T$, the refractive index at ambient temperature ($T_0$) and the temperature change ($\Delta T = T - T_0$) respectively. Towards the end of the chapter, TOCs of gold at telecom wavelengths will be computed and compared with values that have been reported so far.

## 2.4 Nanofabrication of samples

The samples that sustain SPPs propagation in this study are comprised of two interfaces (gold/glass), glass as a substrate and a thin gold film as a metallic part situated on the substrate, with a couple of dielectric grating couplers fabricated from a type of polymer on the gold film which provides SPPs excitation along gold/air interface. The detail of nanofabrication of these samples are described step by step in the following paragraphs (see fig.2.1).

### 2.4.1 Preparation of glass substrate

The support material used as a substrate is square coverglasses (22x22 mm$^2$), whose thickness is 170 $\mu$m, manufactured from optical quality borosilicate (BK7). Before using them in nanofabrication, the glasses must be optically clean and decontaminated from all types of nanoparticles. Therefore, a cleaning protocol composed of three steps is implemented in each pre-nanofabrication. First of all, glass substrates to be cleaned are immersed into a beaker filled

with DI (deionized/purified) water containing a little bit of special soap which is left inside an ultrasonic cleaner for 15 minutes at 80 °C. Secondly, the same operation is performed when the beaker is filled only with DI water without soap. Thirdly, the operation is again realized when the beaker is only filled with 2-Propanol (isoproply alcohol). And finally, they are gently blown dried with nitrogen in order to make ready them for nanofabrication.

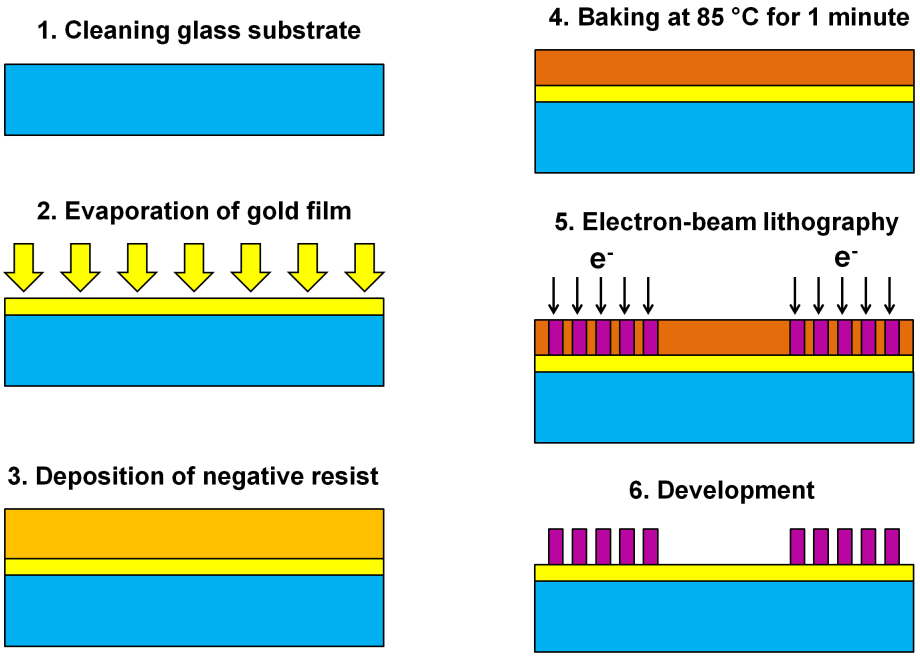


Figure 2.1: Nanofabrication steps for fabricating dielectric grating couplers on a thin gold film

### 2.4.2 Evaporation of thin gold film

The traditional wet cleaning methods as described above are not sufficient to eliminate all types of organic/inorganic nanoparticles. Thus, plasma cleaning with oxygen plasma is carried out upon the corresponding surface of the glass for 15 minutes. After that, evaporation step can be performed slowly and under vacuum condition in order to provide low surface roughness of gold. With the facility of our laboratory (ARCEN platform), it can be deposited 80 nm gold film by evaporation at a speed of 0.1 nm/s under a pressure of $10^{-8}$ mbar leading to a typical RMS roughness of the gold film below 0.8 nm.

### 2.4.3 Deposition of negative resist

It was mentioned previously that a gold/air SPP mode will be launched via dielectric grating couplers fabricated from a type of polymer. To fabricate these grating couplers, it is required to accomplish three steps; deposition of negative resist, electron-beam lithography and development process. As a negative e-beam resist, AR-N 7500, a novolac-based e-beam resist (from Allresist Co.), is chosen for this purpose which can be readily deposited onto 80 nm thick evaporated gold film surface by a spin-coating procedure. The thickness of the resist film

is determined by the quantity of the deposited resist (160 $\mu$L), rotation speed of the sample (1750 rpm for 50 s) and viscosity of the resist which all result in $\sim$ 600 nm in our case. Right after the spin-coating procedure, the sample is baked on a hot plate at 85 °C for 1 minute to increase robustness and durability of the resist before starting the electron-beam lithography step.

### 2.4.4 Electron-beam lithography

The desired pattern is exposed onto the negative resist and revealed by the development process subsequently. Electron-beam lithography is basically a process of scanning focused beam of electrons point by point in order to trace particular shapes on an electro-sensitive resist. Scanning Electron Microscope (SEM) - JEOL 6500F is serving in our laboratory as an e-beam lithography setup.

First, dielectric grating couplers are designed by a specific lithography software (Elphy Quantum RAITH) interconnected to SEM - JEOL which allows us to draw intended patterns and to exposure desired area by means of piloting electron beams on the sample. The sketch of designed dielectric grating couplers is shown in the figure 2.2 depicted by top view and cross-sectional view. The distance between input and output grating couplers is determined to be 200 $\mu$m and the length of each coupler is 40 $\mu$m.

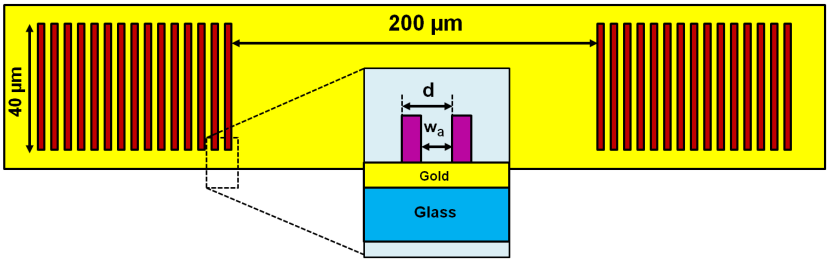


Figure 2.2: Top view and cross-sectional view of dielectric grating couplers deposited on top of 80 nm thin gold film lying on a glass substrate

SPPs excitation via dielectric grating couplers is similar to metallic grating couplers which have been extensively investigated in the literature. It has been demonstrated recently that SPPs excitation by dielectric loaded grating couplers (DLGs) is a function of two parameters such that period ($d$) and filling factor ($w_a/d$) of the grating couplers in such a way that [121]:

$$k_{spp} = k_{\parallel}^{inc} + mG \tag{2.8}$$

$$k_0\sqrt{\epsilon_{av}} = k_0 \sin\theta + m\frac{2\pi}{d} \tag{2.9}$$

where $k_{spp}$ is SPPs wave vector, $k_{\parallel}^{inc}$ is the incident wave-vector component parallel to the average surface of the gratings, m is the order of diffraction harmonics (integer) and G is the grating momentum vector of couplers which provides an additional momentum to in-plane wave vector in order to excite SPPs. The equation 2.8 can be expanded to a more appropriate form as given by the equation 2.9 in which $k_0 = 2\pi/\lambda_0$ is free-space wave vector (impinging

at an angle $\theta$ with respect to the normal of the sample surface) at telecom wavelengths (in our case), $d$ is the grating period and $\sqrt{\epsilon_{av}}$ is an average effective index for SPP mode traveling along the metal surface which is given by:

$$\sqrt{\epsilon_{av}} = \sqrt{n_p^2 + \frac{w_a}{d}(n_a^2 - n_p^2)} \tag{2.10}$$

where $n_a$ and $n_p$ denote to the real part of the effective indices of the SPPs along the metal-superstrate and the metal-polymer flat interfaces respectively and $w_a/d$ refers to the filling factor. Substituting appropriate values of $n_a = 1.005$ and $n_p = 1.25$ which are computed from reflective pole method with respect to our case results in 1.134 for $\sqrt{\epsilon_{av}}$ provided that the filling factor assumed be 50% initially. And after that, the period of the grating couplers which ensure efficient SPPs excitation can be easily computed from the equation 2.9 that yields us $d = 2.44\ \mu$m.

After the completion of dielectric grating coupler design, e-beam lithography process can be launched provided that the parameters are properly defined by means of RAITH software such as working distance, accelerating voltage, beam current, doses and lens alignment/stigmation adjustment.

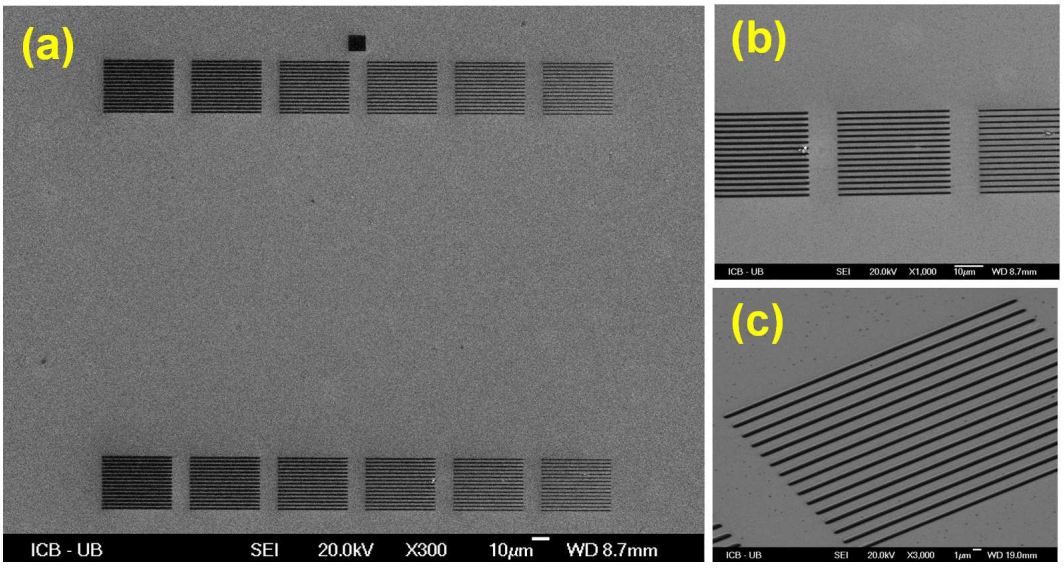


Figure 2.3: (a) Top view SEM image of various grating couplers on the thin gold film (b) More closer top view SEM image of grating couplers at 1000x magnification (c) Tilted-top view SEM image of grating couplers at 3000x magnification

### 2.4.5 Development

As soon as the lithography process finishes, the sample is immersed inside a beaker containing the developer of our negative resist (AR 300) for 2 minutes. During the development process, while the exposed part of the resist remains untouched (i.e. negative resist character), non-exposed one starts to dissolve gradually. At the end of the development step, the process is

stopped by rinsing the sample inside a beaker filled with DI water and immediately after is gently blown dried with nitrogen. Finally, the fabricated sample is observed with an optical microscope to check the nanofabrication quality and whether is ready for characterization step. For instance, SEM images of fabricated dielectric grating couplers are presented in the figure 2.3.

## 2.5 Characterization set-up

The experimental set-up used for the measurement of the SPPs photo-thermal modulation consists of various optical/electrical devices and elements. The principal and core part of the set-up is a high numerical aperture inverted microscope equipped with an immersion oil objective which has a specific configuration for displaying SPPs propagation. So before considering anything else on the set-up, it is more reasonable to show and describe this specific configuration of the inverted optical microscope known as leakage radiation microscopy (LRM).

### 2.5.1 Leakage radiation microscopy (LRM)

Together with the evolution of the investigations on SPPs, detection and monitoring methods have also progressed well thanks to the developments in microscopy imaging techniques. Near-field optical microscopy has been demonstrated for the first time at optical regimes toward the end of the twentieth century [122]. Especially, the implementation of scanning probes with scanning near-field optical microscopy (SNOM) has provided images with subwavelength resolution in the near-field (distance from the sample $\ll \lambda$) [123, 124]. The photon scanning tunneling microscope (PSTM), a new form of scanning optical microscope that uses total internal reflectance (TIR) feature of a light beam, has also been established [51] and demonstrated to be an appropriate instrument to observe propagation of SPPs in the near-field [125]. Although the near-field detection of SPPs has been used extensively, a long acquisition time for imaging, an advanced signal processing requirement and a rather complex optical set-up demand may be accounted as various drawbacks.

On the other hand, it is not directly possible to visualize SPPs propagation by the far-field imaging techniques owing to the confined subwavelength nature of SPPs along the structures on a sample. However, recently a direct and quantitative far-field imaging technique based on the detection of leakage radiation from SPPs propagation has been proposed on thin films [126–128]. It is well-known that when a thin film SPP mode propagates, it experiences energy losses from different channels. First, ohmic losses are at the origin of the conversion into heat of a fraction of the SPPs energy travelling along the interface. Second, when the film is thin enough, the power of the SPP mode can also be radiated within a high refractive index medium provided that its index is larger than the effective index of the SPP mode. For instance, if we assume that the refractive index of the substrate (glass in our case) is larger than the ones of the superstrate (e.g. air), leakage radiation (LR) will occurs provided that the phase matching condition is fulfilled between the wave vector of SPPs ($k_{spp}$) and wave vector of light ($nk_0$) inside the substrate such that:

$$k_{spp} = nk_0 \sin\theta_{spp} \tag{2.11}$$

$n, k_0$ and $\theta_{spp}$ are refractive index of substrate, free-space wave vector in air and inclination angle of SPPs, respectively ($\theta_{spp} > \theta_{crit}$). This condition also implies that LR can be readily imaged with a high numerical aperture (N.A.) microscope objective no matter how SPPs is excited either from the superstrate side (e.g. with a grating couplers or protrusion) or from the substrate side by a Kretschmann-Raether configuration. The only condition to be fulfilled is that the numerical aperture of the collection objective has to be greater than the effective index of the mode, N.A.$> k_{spp}/k_0$.

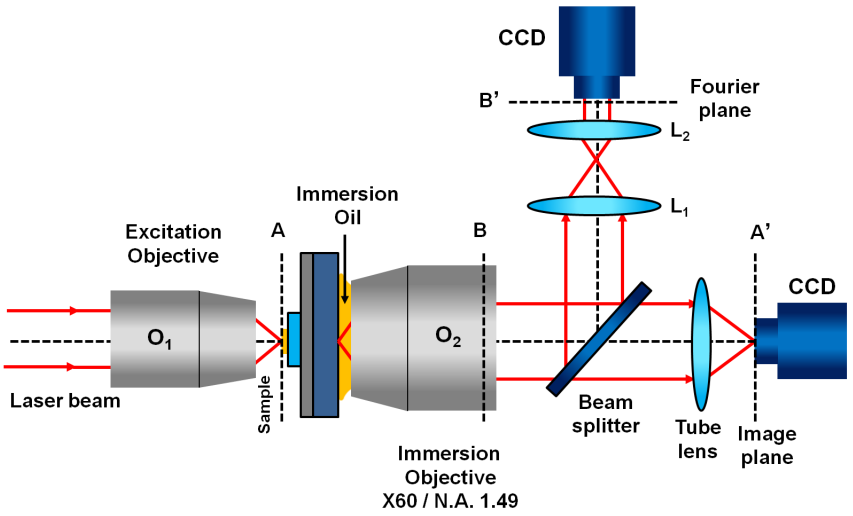


Figure 2.4: Leakage radiation microscopy optical beam path: $O_1$, excitation objective; A-A', sample plane-image plane; $O_2$, high N.A. immersion microscope objective; B-B', back focal plane-fourier plane; Tube and $L_{1/2}$, are convex lenses; CCD, charge-coupled device or camera

A typical experimental scheme for the observation of SPPs excitation and propagation by LRM setup is sketched in the figure 2.4. The incident laser beam is focused on the sample by an excitation objective ($O_1$) in order to launch SPPs propagation. As the SPPs is excited and start to propagate along air/metal interface, leakage radiations emitted from SPPs is intrinsically detected and visualized by an inverted high numerical aperture immersion collective objective ($O_2$, 60$\times$ / N.A. 1.49) due to the tunneling of the leakage radiations through thin metal film and glass, respectively. Subsequently, the LRs of the sample plane (A) are captured by a CCD located at the image plane of the sample (A') through the tube lens. From this a direct space image of SPPs propagation is obtained. Besides, a reciprocal image is formed at the back focal plane (B) inside the microscope which is the conjugate of the fourier plane (B') and is imaged by the other CCD through two convex lenses ($L_{1/2}$). Therefore, the LRM presents both direct space and fourier space image of a SPPs propagation with a simple optical set-up simultaneously which proves a direct instant imaging of the SPPs intensity corresponding to the SPPs propagation above. No resolution refers to spatial resolution. The temporal dynamic of the set-up is however limited by the characteristic acquisition time of the camera. In this respect alternative solutions to LRM for time resolved characterizations are needed and will be proposed and demonstrated throughout this thesis.

### 2.5.2 Experimental set-up

The experimental set-up used for the measurement of the photo-thermal modulation of the SPPs propagation is schematically shown in the figure 2.5. The set-up is built-up around an inverted microscope equipped with an immersion oil objective (LRM) featuring a large numerical aperture (Apo TIRF 60X / 1.49 Oil). The image collected by the immersion oil objective can be directed either on a visible CCD camera or on a sensitive InGaAs infrared camera. The samples mounted onto the microscope stage are excited at telecom frequencies by a lensed fiber generating a slightly focused spot with a typical radius of 20 $\mu$m. The input focuser is tilted at an angle of 30° with respect to the optical axis of the microscope. A similar focuser is used for output detection.

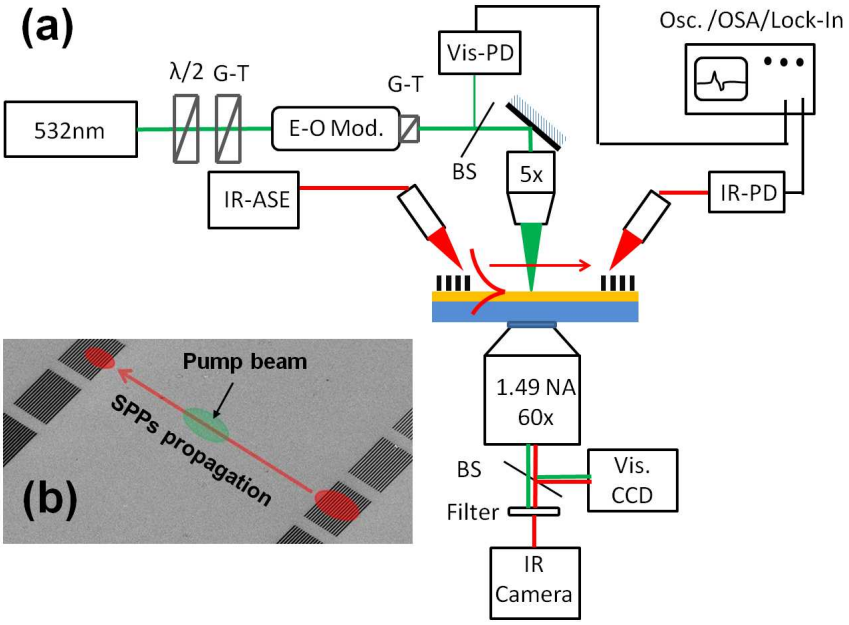


Figure 2.5: (a) Schematic view of the experimental set-up (b) Bird-eye view of the input and output grating couplers fabricated on the surface of a thin gold film in which SPPs propagation and pump beam are sketched in a representative manner

An arrangement comprising a low numerical aperture long working distance objective (EPI L Plan Apo 5X / 0.16) is placed above the microscope stage to focus the pump beam (free-space wavelength=532 nm). The pump laser can be either a continuous-wave laser modulated by a highly efficient 20 ns rise/fall-time electro-optics modulator or a Q-switched laser generating nanosecond pulses. The samples used to investigate photo-thermal modulation of SPPs propagation are comprised of dielectric input and output grating couplers fabricated by e-beam lithography using a negative tone resist lying on the surface of a 80 nm thin gold film evaporated onto a 170 $\mu$m-thick glass substrate as explained in detail in the previous section (see fig.2.3 and 2.5(b)).

The grating couplers are separated by a distance of 200 $\mu$m and are excited by an incoherent near-infrared amplified spontaneous source peaked at 1530 nm whose spectrum is displayed in the figure 2.6(a). The choice of a broadband incoherent light source in the con-

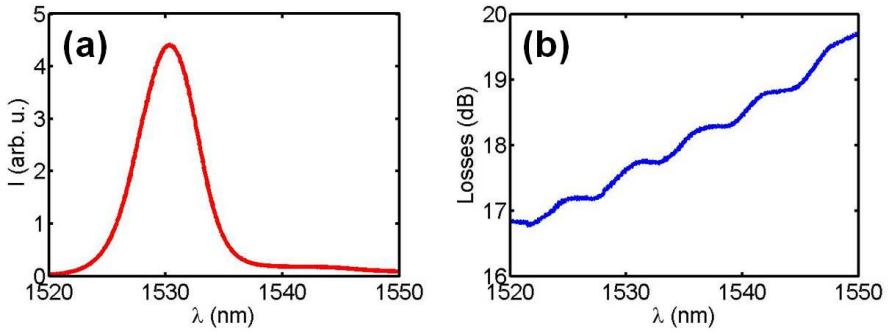


Figure 2.6: (a) Spectrum of the incoherent light-source used for the excitation of the SPP modes (b) Typical insertion losses for SPPs signal fiber-to-fiber transmission

text of this work is dictated by the fact that we want to minimize potential thermally induced changes of the grating coupling efficiency. Indeed, the thermally-induced mismatch with the Bragg condition is expected to be attenuated for a broadband source compared to the case of a highly coherent incident light. The near-infrared signal detected by the output focuser can be directed onto an optical spectrum analyzer (OSA) or a fast sensitive InGaAs photodetector/photodiode (rise time of 2ns / freq. range 0-250 MHz). The signal of the InGaAs photodiode is monitored by a 1 GHz bandwidth oscilloscope triggered by the signal of the fast visible photodetector/photodiode (rise time of 2 ns / freq. range 0-250 MHz) receiving a tiny fraction of the pump beam.

The coupling efficiency of the gratings has been characterized by recording the spectrum of the transmitted SPPs signal when the input and output focusers are adjusted at optimum positions on the gratings. This spectrum has been subsequently compared to the reference spectrum obtained by detecting the specular reflection of the incident infrared spot onto a bare gold film area. With this definition of the reference situation, insertion losses including in and out grating coupling losses and SPPs propagation losses are below 18 dB at 1530 nm (see fig.2.6(b)). It should be also noted that the insertion losses increase with the wavelength indicating that the main contribution to these losses are the coupling losses and not the propagation losses given that propagation losses are expected to decrease for increasing wavelengths.

## 2.6 Photo-thermal modulation of SPPs propagation

Our configuration allows us to record simultaneously leakage radiation (LR) images of a SPP mode travelling between the input and output grating couplers and the corresponding fiber to-fiber signal. LR images of the gold/air SPP jet excited by the input grating coupler shown on the scanning electron microscope image of the figure 2.7(a) are displayed in the figures 2.7(b) and 2.7(c) with the visible pump being respectively off and on. The illumination of the input grating coupler by the incident spot leads to a SPP jet with a transverse cross-cut of the intensity matching a Gaussian profile given by $I(x,y) = I(x,0)\exp\frac{-2y^2}{w_{jet}^2}$ with a waist $w_{jet} = 9.5\ \mu m$ (see fig.2.7(d)).

The visible pump spot in the figure 2.7(c) can be observed with the InGaAs-IR camera provided that the long-pass filter placed in front of the camera is removed. In this situation, the

visible pump light can be observed with the InGaAs sensors at the expense of a sufficiently long exposure time. By varying the pump beam power and monitoring the resulting signal onto the InGaAs camera, it has been verified the linearity of the InGaAs sensors making the use of the InGaAs camera convenient for measurement of the pump spot size. The pump spot shown in the figure 2.7(c) and in the inset of the figure 2.7(e) corresponds to the pump spot used during the experiments conducted with the cw (continuous wave) illumination. As shown in the figure 2.7(e), the spot can be approximated by a Gaussian beam with a $16\mu m$ half-width at $1/e^2$ of the maximum intensity.

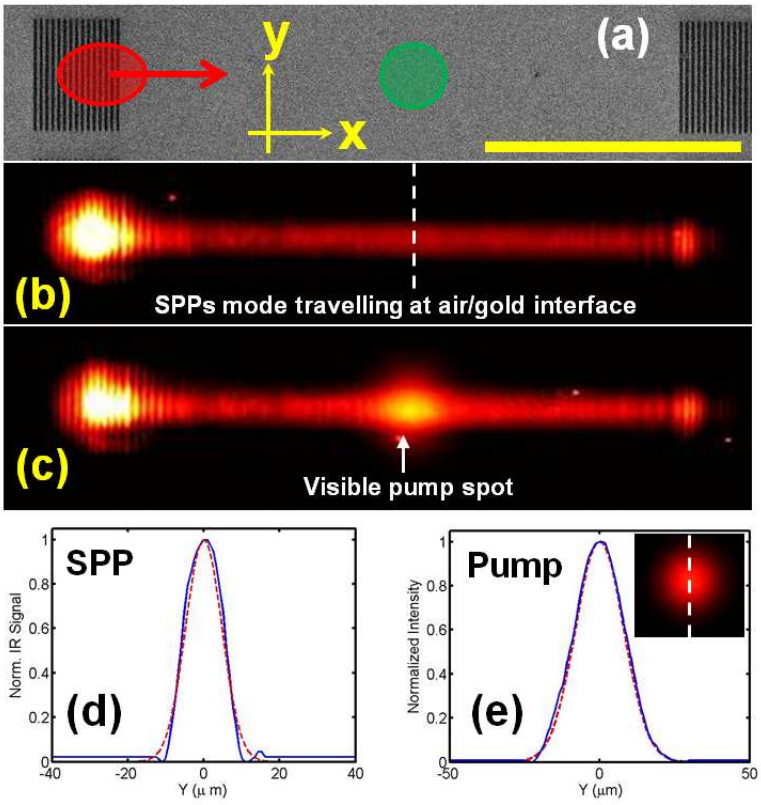


Figure 2.7: (a) SEM image of the grating couplers showing the respective location of the input infrared and visible pump spot (scale bar=100 $\mu$m) (b) (resp.(c)) Leakage radiation image of the SPP jet generated by the input grating coupler with the pump spot off (resp. on) (d) Solid line: Cross-cut of the SPP jet. The jet can be approximated by a Gaussian profile (dashed line) with a waist of 9.5 $\mu$m (e) Solid-line: Cross-cut of the intensity distribution of the pump spot. The pump spot can be approximated by a Gaussian beam (dashed line) with a waist of 16 $\mu$m

Figure 2.8(a) shows the ac coupled SPPs signal detected by the InGaAs IR photo-diode along with the visible photo-diode signal when a photo-thermal cw excitation modulated at a frequency of 1 kHz (duty cycle=50%) is applied on the SPPs propagation path. For an incident power of 100 mW (power of the pump beam measured after the 5x objective and without modulation), the relative depth of modulation $|\Delta I/I|$ is found to be 4.5%. In all the following, the relative depth of modulation is defined as the ratio of the SPPs signal modulation $\Delta I$ during the

photo-thermal pumping to the SPPs signal $I$ in the cold state in absence of pumping. Knowing the depth of modulation $\Delta I/I$ obtained for known parameters (pump power, pump spot size, plasmon jet width...), a model for SPPs propagation modulation is needed to correlate the thermo-optical characteristics of the SPP mode to the experimental value of $\Delta I/I$.

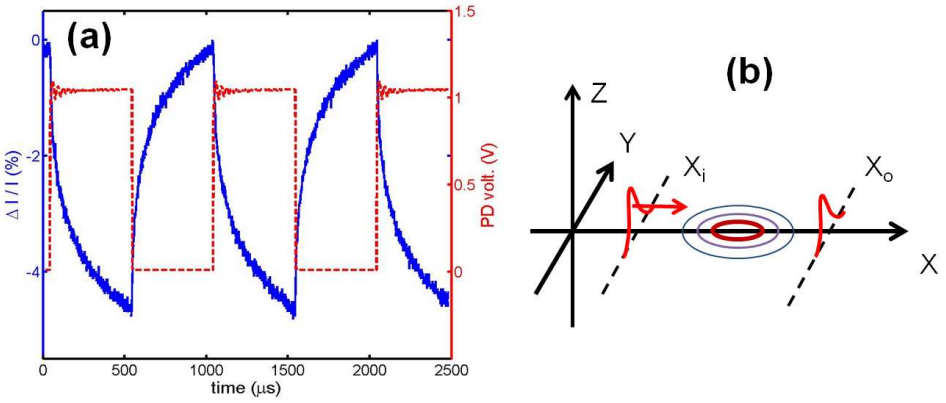


Figure 2.8: (a) Solid-line: SPPs signal modulation recorded with the IR photo-diode in the case of a photo-thermal excitation with a cw illumination (100mW) modulated at a frequency of 1kHz (duty-cycle=50%). Dashed-line: control signal of the visible photo-diode showing the modulation of the cw pump beam (b) Schematic view of the SPP jet propagation. The input (resp. output) grating coupler is located at $x = x_i$ (resp. $x = x_o$)

In this modeling, the situation can be considered as depicted in the figure 2.8(b). A gold/air plasmon jet centered on the y-axis is travelling along x-axis toward the positive values of x. The plasmon jet has a Gaussian transverse profile (along the y-axis) with a waist $w_{jet}$. We assume that the gold film supporting the SPP mode is locally heated creating a known temperature distribution $T_f(x, y)$ in the plane of the film. More precisely, $T_f(x, y)$ denotes the average temperature of the film over the penetration depth of the SPP mode field. At telecom wavelengths, this penetration depth does not exceed of a few tenths of nanometers. Owing to the vanishing temperature gradient of the gold film over such a thickness, the $z$ dependence for temperature $T_f$ can be safely neglected.

For $w_{jet}$ large enough compared to the SPP wavelength, the width of the spatial frequencies spectrum of the plasmon jet can be neglected in the first approximation and the electric field of the SPP jet in the plane of the film verifies:

$$\vec{E}^h(x, y) = \vec{E}^h(x_i, y) \exp(i\Phi(x, x_i, y)) \tag{2.12}$$

where the superscript $h$ indicates that the film is in the "hot" state. The function $\Phi(x, x_i, y)$ accounts for the accumulation of phase and damping along the distance $(x - x_i)$ and is given by:

$$\Phi(x, x_i, y) = \int_{x_i}^{x} k_{spp}(x', y)dx' \tag{2.13}$$

The function $k_{spp}(x', y)$ denotes the complex SPPs wavevector which depends upon the observation point through the temperature distribution $T_f(x', y)$. The skin depth of gold in the infrared depends linearly on temperature over a range of more than 1000 K [106]. Thus, for a sufficiently small temperature change in the range of one or two hundreds of Kelvins, the SPPs wavevector is expected to depend linearly on the temperature as well in such a way that:

$$k'_{spp}(x', y) = k'_{spp} + \partial_T k'_{spp}(T_f(x', y) - T_{room}) \tag{2.14}$$

and

$$k''_{spp}(x', y) = k''_{spp} + \partial_T k''_{spp}(T_f(x', y) - T_{room}) \tag{2.15}$$

where $k'_{spp}$ and $k''_{spp}$ are respectively the phase and damping constant of the SPP mode in the "cold" state when the film is at room temperature $T_{room}$ and where $\partial_T k'_{spp}$ and $\partial_T k''_{spp}$ are the partial derivative of respectively the phase and damping constant with respect to the temperature. By introducing equations 2.14 and 2.15 into 2.12, the field at $x = x_o$ can be written:

$$\vec{E}^h(x_o, y) = \vec{E}^h(x_i, y) \exp(i\Phi(x_o, x_i, y)) \tag{2.16}$$

where $\Phi(x_o, x_i, y)$ is given by:

$$\Phi(x_o, x_i, y) = (k'_{spp} + ik''_{spp})(x_o - x_i) + (\partial_T k'_{spp} + i\partial_T k''_{spp}) \int_{x_i}^{x_o} \Delta T(x', y) dx' \tag{2.17}$$

where $\Delta T(x', y) = T_f(x', y) - T_{room}$.

For the observation points located along the line $x = x_i$, we assume that the SPP electric field is unaffected by the heating of the film. This assumption is realistic provided that the $x = x_i$ line is located at a sufficiently large distance from the pump spot. With this assumption, we have $\vec{E}^h(x_i, y) = \vec{E}^c(x_i, y)$ where the superscript "c" indicates that the field corresponds to the cold state. By using this last assumption and by noting that $\vec{E}^c(x_o, y) = \vec{E}^c(x_i, y) \exp(i(k'_{spp} + ik''_{spp})(x_o - x_i))$, the electric field in the hot state along the profile $x = x_o$ can be expressed as:

$$\vec{E}^h(x_o, y) = \vec{E}^c(x_o, y) \exp(i\partial_T k'_{spp} \int_{x_i}^{x_o} \Delta T(x', y) dx') \exp(-\partial_T k''_{spp} \int_{x_i}^{x_o} \Delta T(x', y) dx') \tag{2.18}$$

From this last equation, the electric field intensity along the profile $x = x_o$ is given by:

$$I^h(x_o, y) = I^c(x_o, y) \exp(-2\partial_T k''_{spp} \int_{x_i}^{x_o} \Delta T(x', y) dx') \tag{2.19}$$

Experimentally, the signal we record accounts for the intensity distribution of the plasmon jet

at the location of the output grating. In this respect, the experimental signal can be approximated by:

$$\frac{\Delta I}{I} = \frac{\int_{-\infty}^{\infty}(I^h(x_o,y) - I^c(x_o,y))dy}{\int_{-\infty}^{\infty} I^c(x_o,y)dy} \tag{2.20}$$

Given that the argument of the exponential term in the equation 2.19 is expected to be small, the depth of modulation $\frac{\Delta I}{I}$ can be expressed as:

$$\frac{\Delta I}{I} = \frac{-\int_{-\infty}^{\infty} I^c(x_o,y)(2\partial_T k''_{spp}\int_{x_i}^{x_o}\Delta T(x',y)dx')dy}{\int_{-\infty}^{\infty} I^c(x_o,y)dy} \tag{2.21}$$

The plasmon jet having an intensity Gaussian distribution along the $y$-axis, the cold state intensity can be written:

$$I^c(x_o,y) = I_0\exp(-2k''_{spp}x_o)\exp(\frac{-2y^2}{w_{jet}^2}) \tag{2.22}$$

By introducing $I^c(x_o,y)$ into the equation 2.20 and using Gauss integrals, we find that the experimental depth of modulation is related to the temperature derivative of the damping constant of the SPP mode by:

$$|\frac{\Delta I}{I}| = 2\partial_T k''_{spp}\int_{x_i}^{x_o}\Delta T_{av}(x')dx' \tag{2.23}$$

where the average change of temperature is given by:

$$\Delta T_{av}(x') = \int_{-\infty}^{\infty}\sqrt{\frac{2}{\pi w_{jet}^2}}\exp(\frac{-2y^2}{w_{jet}^2})\Delta T(x',y)dy \tag{2.24}$$

It should be emphasized that this approach holds for temperature ranges such that the SPP effective index depends linearly on temperature and for a collimated plasmon jet with a Gaussian transverse intensity profile. On the basis of this analysis, we conclude that the temperature derivative of the SPP mode damping constant, denoted hereafter as the *thermo-plasmonic coefficient*, can be extracted from the experimental depth of modulation provided that the temperature distribution along the thin film is known. Note that, so far, only the thermo-plasmonic coefficient can be obtained with this approach. In order to correlate this SPP mode property to the thermo-optical properties of gold, further developments are necessary.

## 2.7 Thermo-optical coefficients of gold at telecom frequencies

### 2.7.1 Gold TOCs characterization from the gold/air thermo-modulation

It has been shown in the previous section that the thermo-plasmonic coefficient $\partial_T k''_{spp}$ can be obtained from the SPPs thermo-modulation depth as long as the temperature distribution along the film is known (see equation 2.23). However, in order to correlate this parameter to

the thermo-optical properties of gold, we need to analyze in more detail the SPPs properties at a gold/air interface at telecom frequencies.

For a gold film which is thick enough to neglect radiation losses compared to intrinsic losses, the SPPs wavevector of a gold/dielectric interface can be approximated by [34]:

$$k_{spp} \simeq k_0 \sqrt{\frac{\epsilon_m \epsilon_d}{\epsilon_m + \epsilon_d}} \tag{2.25}$$

where $\epsilon_m$ and $\epsilon_d$ are respectively the dielectric function of gold and of the dielectric medium in contact with gold (air in our case), and where $k_0 = 2\pi/\lambda_0$, with $\lambda_0$ the free-space wavelength of the incident light. At telecom frequencies, the absolute value of the real part of the dielectric function of gold is much larger than the imaginary part, $|\epsilon_m^{'}| \gg \epsilon_m^{''}$, at $\lambda_0 = 1.53\ \mu m$ for instance $\epsilon = \epsilon_m^{'} + \epsilon_m^{''}$ is equal to $-113.16 + 10.97i$ [129]. In addition, if $|\epsilon_m^{'}|$ is also much larger than $\epsilon_d$, the attenuation constant of the SPP mode traveling at the metal/dielectric interface can be approximated such that:

$$k_{spp}^{''} = k_0 \frac{\epsilon_m^{''}}{2(\epsilon_m^{'})^2} \Big( \frac{\epsilon_m^{'} \epsilon_d}{\epsilon_m^{'} + \epsilon_d} \Big)^{\frac{3}{2}} \simeq \frac{k_0}{2} \frac{\epsilon_d^{3/2} \epsilon_m^{''}}{(\epsilon_m^{'})^2} \tag{2.26}$$

As stated previously that the complex dielectric function $\epsilon_m$ is related to the complex refractive index of gold through the relation $\epsilon_m = (n + i\kappa)^2$ where $n$ and $\kappa$ are respectively the real refractive index and the extinction coefficient of gold. On the other hand, at telecom frequencies, $\kappa$ is typically more than ten times larger than $n$ in such a way that the real dielectric function can be approximated by $\epsilon_m^{'} = (n^2 - \kappa^2) \simeq -\kappa^2$. By substituting of $\epsilon_m^{'} \simeq -\kappa^2$ and $\epsilon_m^{''} = 2n\kappa$ into the equation 2.26 and taking the temperature derivative of both sides, which will be denoted $\partial_T$ hereafter, it is thus obtained as follows:

$$\partial_T k_{spp}^{''} = \frac{k_0 \epsilon_d^{3/2}}{\kappa^3} \Big( \partial_T n - \frac{3n}{\kappa} \partial_T \kappa \Big) \tag{2.27}$$

Note that this last equation holds only if the dielectric function $\epsilon_d$ is only marginally affected by the heating of the gold film, a condition that is expected to be fulfilled when the SPP mode is travelling at the interface between gold and air. It should be also emphasized that the equation 2.27 indicates that if the temperature derivatives $\partial_T n$ and $\partial_T \kappa$ are of same order of magnitude, the main contribution to $\partial_T k_{spp}^{''}$ comes from the real part of the TOC ($\partial_T n$) of gold since the ratio $3n/\kappa$ is of the order of 10 % for gold in the infrared.

In order to compute these two TOCs of gold ($\partial_T n$ and $\partial_T \kappa$) in addition to the equation 2.27, a second equation is necessary. This equation can be simply derived from the equality of $\epsilon_m^{''} = 2n\kappa$ by taking its temperature derivative in a such way:

$$\partial_T \epsilon_m^{''} = 2\kappa \partial_T n + 2n \partial_T \kappa \tag{2.28}$$

Nevertheless, the value of $\partial_T \epsilon_m^{''}$ is also needed in order to solve the equations 2.27 and 2.28 together. This value is provided by the experimental data reported in the reference [105] where the change of complex dielectric function of gold have been investigated for temperatures

ranging from 295K to 770K. The same data have been used to extract gold TOCs over the visible range in the reference [101] at the cost however of a Kramer-Kronig analysis. Therefore, the experimental data from the reference [105] are used to evaluate the temperature derivative $\partial_T \epsilon_m^{''}$ which is needed in conjunction with the equation 2.27 to extract gold TOCs.

As a result, gold TOCs can be computed by using the equations 2.27 and 2.28 provided that $\partial_T k_{spp}^{''}$ and $\partial_T \epsilon_m^{''}$ are known. However, according to the equation 2.23, the thermo-plasmonic coefficient $\partial_T k_{spp}^{''}$ can only be evaluated from the measurement of the modulation depth $\frac{\Delta I}{I}$ if the temperature distribution of the gold film, $\Delta T_{av}(x')$ is known. The approach that is used for the computation of this temperature distribution along the gold film is described in the next section.

### 2.7.2 Temperature distribution of the gold film under modulated continuous-wave (cw) laser beam illumination

The problem of computing the temperature distribution in a bulk metal under a laser irradiation is of key importance in fields such as laser machining for example. Usually, the situation is reduced to a one-dimensional heat diffusion problem leading to an analytical solution [130]. In our case, we rely on a numerical approach in order to avoid an oversimplification of the system. Owing to the cylindrical symmetry of a Gaussian beam impinging at normal incidence onto an infinitely extended thin film, it is considered the situation depicted in the figure 2.9.

In cylindrical coordinates the time-dependent heat diffusion equation can be written as follows:

$$\rho C_p \frac{\partial T}{\partial t} = \frac{1}{r}\frac{\partial}{\partial r}\Big(rk\frac{\partial T}{\partial r}\Big) + \frac{\partial}{\partial z}\Big(k\frac{\partial T}{\partial z}\Big) + \tilde{Q}_E(r,z) \tag{2.29}$$

where $\rho$, $C_p$ and $k$ are position dependent functions representing respectively the density, the specific heat and the thermal conductivity of the different materials in the system. The source term $\tilde{Q}_E(r,z)$ corresponds to a volume power density and is denoted in all the following as the heat source density (HSD). In our case, the HSD is generated by the ohmic losses of the pump beam into the metal film or it is originated from the temperature-dependent ohmic losses of the gold film. The HSD or in other words the amount of energy converted into heat in the film per unit time per unit volume is given by [131]:

$$\tilde{Q}_E(r,z) = \frac{1}{2}\Re(\vec{J}(r,z).\vec{E}^*(r,z)) \tag{2.30}$$

where $\vec{J}$ is the current density and where $\Re$ denotes the real part. By using Ohm's law, the heat source density can be more conveniently written in our situation:

$$\tilde{Q}_E(r,z) = n\kappa\frac{k_0}{Z_0}|E(r,z)|^2 \tag{2.31}$$

where $Z_0$ is the vacuum impedance and where $n+i\kappa$ is the complex refractive index of gold at the pump frequency for observation points located within the thin gold film. The HSD can be

readily computed by using a plane wave expansion of the incident pump beam [132]. Figure 2.9(b) shows the electric field intensity distribution of a Gaussian beam expanded over up to 430 plane-waves ($\lambda_0 = 532\ nm$, beam waits=16 $\mu$m) carrying a total power of 100 mW.

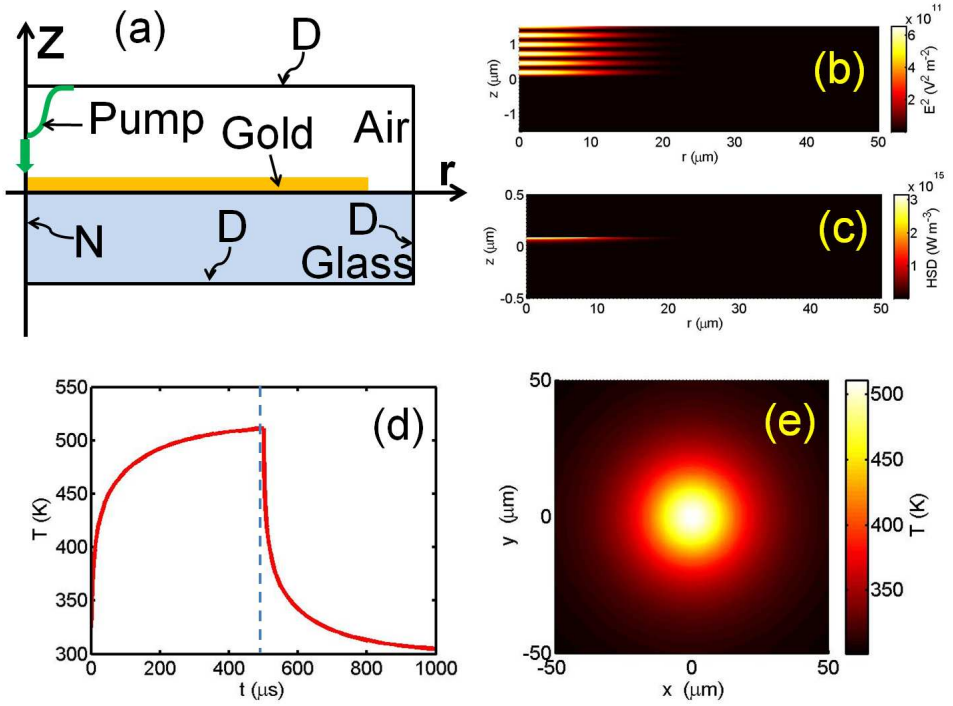


Figure 2.9: (a) Schematic view of the system considered for the finite-difference computation of the temperature distribution along the gold thin film under photo-thermal excitation. The computation window is 100 $\mu$m long (along r coordinate) and 50 $\mu$m high (in the Z direction). A Neumann (N) boundary condition $\partial T/\partial r = 0$ is applied at $r = 0$ due to the rotational symmetry around $Z$-axis whereas Dirichlet (D) conditions $T = T_{room}$ are used for the three other boundaries (b) Electric intensity distribution of the interference pattern created by the interaction of the normally incident and back-reflected pump beams. The power carried by the incident beam is 100 mW (c) Heat-source density distribution corresponding to the electric intensity distribution shown in the figure (b) (d) Temperature in the thin film at the focal point of the Gaussian beam as a function of time (in the case of 1 kHz modulation frequency with a 50 % duty-cycle) (e) Spatial temperature distribution at the surface of the thin film at t=500 $\mu$s

Although not necessary for a system comprised of a bare thin film deposited onto a substrate, the plane wave expansion of the Gaussian beam becomes very convenient to account for the presence of a surface defect on top of the thin film [133]. The electric field for observation points within the metal film is obtained from this plane wave expansion and eventually the HSD is computed according to the equation 2.31. Figure 2.9(c) shows the HSD corresponding to the pump beam falling onto a 80nm-thick gold film. As expected, the HSD features a strong decay along the direction perpendicular to the thin film as a result of the 35nm skin depth for gold at 532 nm. The HSD spatial distribution is next used as an input for solving the heat diffusion equation 2.29. We use an implicit centered finite difference scheme implemented on a non-regular rectangular mesh [134, 135] in order to compute the temperature distribution at all observation points within the computation windows (see the caption of the figure 2.9).

At this stage, the value for the thermal conductivity $k$ of the gold film must be chosen carefully as it impacts both the transient properties and the steady-state temperature distribution of the gold film. It is well known that for metal thin films with a thickness of the order of the electrons mean free path, the classical size effect [136] reduces significantly thermal conductivity compared to bulk materials. For example, for bulk gold $k$ is tabulated at 317 $Wm^{-1}K^{-1}$ whereas in the case of films with a typical thickness around 100 nm, thermal conductivity as low as $k = 120\ Wm^{-1}K^{-1}$ have been obtained [137]. The ratio of the bulk conductivity $k_b$ to the thin films conductivity $k$ is given by [137]:

$$\frac{k_b}{k} = 1 + \frac{3}{8t} + \frac{7\alpha}{5} \tag{2.32}$$

where $t = d/l$ and $\alpha = l/D(R/(1-R))$ with $d$ the film thickness, $l$ the electron's mean free path, $D$ the average grain size in the film and $R$ the grain boundary reflection coefficient. These parameters have been specifically investigated for gold in the mid-infrared in the reference [138]. For polycrystalline thin films, typical values for $l$ and $R$ are 17 nm and 0.63 respectively. High magnification scanning electron microscope characterization (not shown) reveals that the average grain size for our 80 nm-thick films is about $D = 65 \pm 6$ nm leading to a heat conductivity for our gold films of $k = 150\ Wm^{-1}K^{-1}$. By using this value, the temperature at the surface of the thin film at the focal point ($r = 0$, $z = 0$) of the pump beam shown in the figure 2.9(d) has been obtained for an incident (dc) power of 100 mW modulated at a frequency of 1 kHz with a duty-cycle of 50 $\%$. The spatial distribution of the temperature in the plane of the thin film at $t = 500$ $\mu$s right before the end of the heating cycle is shown in the figure 2.9(e).

In summary, by knowing the temperature distribution in the film, we can extract first, the thermo-plasmonic coefficient $\partial_T k''_{spp}$ by using the equation 2.23 and second, the thermo-optical coefficients (TOCs) ($\partial_T n$ and $\partial_T \kappa$) of gold by using the equations 2.27 and 2.28 at telecom wavelengths.

### 2.7.3 Thermo-plasmonic figure of merit and gold TOCs at telecom frequencies

The effective computation of gold TOCs is conducted by considering the experimental situation where the pump beam has a power of 100 mW. When modulated at 1 kHz with a duty-cycle of 50 $\%$, the photo-thermal modulation of the SPPs signal travelling through the heated area leads to a modulation depth of $|\Delta I/I| = 4.5\%$ (see fig. 2.8(a)). From this modulation depth and the temperature distribution along the thin gold film at the end of the heating period (t =500 $\mu$s), it is easily evaluated (from the eq. 2.23) the thermo-plasmonic coefficient $\partial_T k''_{spp}$ of the gold/air SPP mode which is $2.90\times10^{-6}\ \mu m^{-1}K^{-1}$.

Secondly, for the reference situation that we consider (when the pump beam power is 100 mW) the maximum temperature of the gold film at the end of the heating period is found to be around 510 K. Therefore, the temperature derivative $\partial_T \epsilon''$ for the gold film is expected to be 0.01425 $K^{-1}$ according to the results reported in the reference [105] for temperatures ranging from 470 K to 670 K. Knowing both $\partial_T k''_{spp}$ and $\partial_T \epsilon''$, the thermo-optical coefficients of the gold film can be obtained from the equations 2.27 and 2.28 provided that the refractive index of gold at room temperature is known.

In all the following we use a complex refractive index of gold of $0.515+i10.65$ extracted from tabulated values reported in the reference [129] for a free-space wavelength of 1.53

$\mu$m. This choice is motivated by the fact that the refractive index of gold thin films was measured at telecom frequencies [139] which are found to be in good agreement with the values reported in the reference [129]. For example, at a free space wavelength of 1.55 $\mu$m, the refractive index of thin films with a typical thickness around 60 nm was measured at $0.505+i10.7$ deviating by less than 3 $\%$ for $n$ and $\kappa$ compared to the value $0.52+i10.8$ reported in the reference [129].

Given the refractive index of gold at room temperature for a free-space wavelength of 1.53 $\mu$m, the linear system formed by the equations 2.27 and 2.28 can be solved for $\partial_T n$ and $\partial_T \kappa$ leading to TO coefficients displayed in the table 2.1.

| TOCs | $\partial_T n$ [K$^{-1}$] | $\partial_T \kappa$ [K$^{-1}$] |
|---|---|---|
| This work | $0.72\text{x}10^{-3}$ | $-1.0\text{x}10^{-3}$ |
| Ref [99] | $1.68\text{x}10^{-3}$ | $-0.32\text{x}10^{-3}$ |
| Ref [101] | $0.55\text{x}10^{-3}$ | $-1.78\text{x}10^{-3}$ |

Table 2.1: Comparison of the thermo-optical coefficients (TOCs) of gold extracted from the measured SPPs depth of modulation (this work [140]) with the temperature-dependent Drude model for gold given in the reference [99] and the results of the reference [101] which are obtained from a linear extrapolation (see the text).

Thermo-optical coefficients of this work are compared to the linear TO coefficients obtained from the temperature-dependent Drude model for gold described in the reference [99] and TO coefficients obtained from a linear extrapolation explained in the reference [101]. Although all of them have same order of magnitude, it should be noted however that our TO coefficients are significantly different from those given in the reference [99]. In particular, $\partial_T n$ is more than two-fold smaller in our case as compared to the model developed in the reference [99]. As a result, our values compare more favorably with the linear extrapolation at 1.53 $\mu$m of the gold TOCs obtained from the Kramer-Kronig analysis of the reference [105] data which are given in the reference [101].

Figure 2.10 (a) shows the modulation depth computed from the equation 2.23 by using either our TOCs values or the model's ones in the reference [99] for different incident peak power pump beam modulated at 1 kHz with a 50 $\%$ duty-cycle. Whatever the incident pump power, the temperature-dependent Drude model for gold leads to a depth of modulation which is overestimated by about 60 $\%$ compared to our experimental values or computed values. The experimental oscilloscope traces of the thermo-modulated SPPs signal displayed in the figures 2.10 (b)-(d) are compared to the modeled traces computed by using our gold TOC values. Apart for a small deviation for times larger than 200 $\mu$s after the beginning of the heating cycle and for an incident power of 100 mW, it is observed a quite good agreement between the

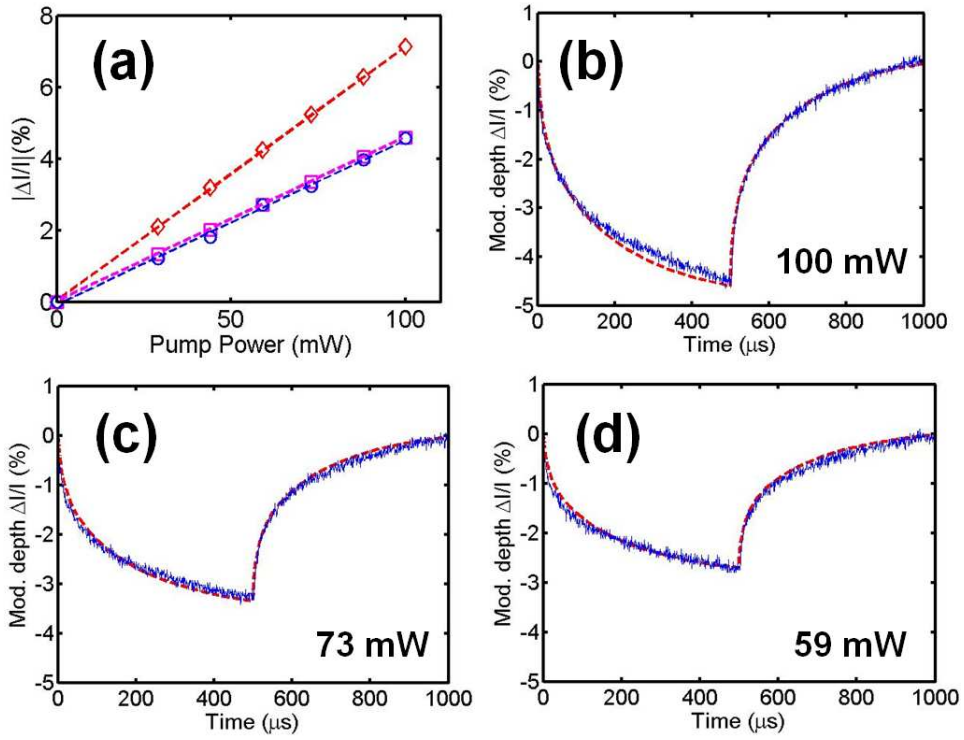


Figure 2.10: (a) Comparison of our experimental modulation depths (open blue circles) with the modulation depths computed using either our gold TOCs values (open pink squares) or the temperature-dependent refractive index (TOCs) given by the reference (open red diamonds) [99] (b) (resp. (c) and (d)) Comparison of the experimental (solid blue line) and computed SPPs modulations (dashed red line) as a function of time in the case of a modulated cw excitation (1 kHz, duty-cycle=50 $\%$ for an incident power of 100 mW (resp. 73 mW and 59 mW)).

computed and the experimental profiles suggesting that our computations allow us to extract not only the amplitude of the photo-thermal modulation but also the characteristic time for this modulation. Although it is of great practical importance, the dynamic of photo-thermal SPPs modulation is however out of the scope of the present chapter and will be analyzed in detail down to the nanosecond regime for confined plasmonic waveguides in the next chapter.

When considering the results displayed in the figure 2.10 (a), it is worth to comment on the amplitude of the SPPs signal photo-thermal modulation. It should be noted that a temperature rise as large as 200 K (for a pump power of 100 mW) generates a SPPs modulation amplitude as small as 4.5 $\%$. This result can be understood from the fact that the gold/air interface mode we consider is only very little confined within the metal and thus features a long propagation distance and accordingly a weak thermo-plasmonic $\partial_T k''_{spp}$ coefficient. For SPP modes with losses dominated by ohmic losses (bounded or a weakly leaking modes), the damping constant $L_{spp} = 1/(2k''_{spp})$ is inversely proportional to the SPPs field confinement into the metal. In this respect, the quantity $L_{spp} \times \partial_T k''_{spp}$ can be viewed as a **figure of merit (FOM)** characterizing the thermo-optical sensitivity of the metal for plasmonic applications at a given frequency. Relying on the modulation obtained for the pump power of 100 mW, it can be found

in our case such that a FOM for gold at telecom wavelengths of:

$$L_{spp} \times \partial_T k''_{spp} = 8.0 \times 10^{-4}\ K^{-1} \tag{2.33}$$

where $L_{spp} = 276\ \mu m$ calculated for the gold/air SPP mode has been used to evaluate the numerical value of the FOM.

As long as thermal modulation of surface plasmon modes is concerned, the use of the FOM defined above is an interesting practical approach. Indeed, by knowing this FOM from measurements performed on a given SPP mode, one can easily obtain at least a coarse evaluation of the thermo-modulation depth for the other SPP mode provided that the propagation distances for the two modes are known in the cold state. For example, by using our gold TOC values, it can be calculated that the depth of modulation for the glass/gold interface SPP mode ($Lspp = 81\ \mu m$) should be around 14.6 % when the pump power is 100 mW. For the same excitation conditions, this depth of modulation is evaluated at 15.3 % when the calculation is performed by using the FOM value for gold given above.

## 2.8 Photo-thermal SPPs modulation in the nanosecond regime

In the previous section, the thermo-optical coefficients of gold have been obtained from the measurements of the SPPs signal thermo-modulation created by a modulated continuous-wave (cw) source. The goal of this last section is to test the reliability of our gold TOC values in the context of a pulsed nanosecond illumination.

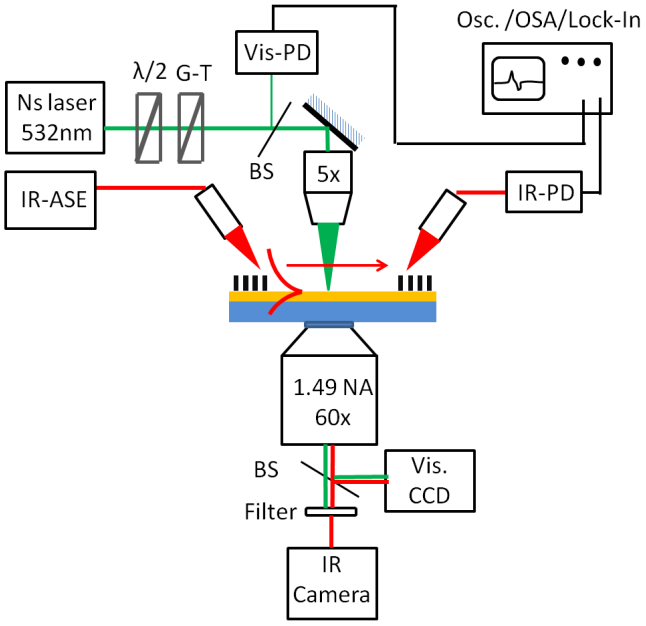


Figure 2.11: Schematic view of the Q-switched visible laser (532 nm) installed experimental setup for measurement of the photo-thermal SPPs modulation in the nanosecond regime

The experimental set-up of this last section have been established simply by replacing the cw laser and the electro-modulator with a 532 nm Q-switched laser as shown in the figure 2.11. The laser has a repetition rate of 8.3 kHz and delivers 6.5 $\mu$J pulses with a width (full width at half maximum) of 0.59 ns as specified by the manufacturer. In all the following, it is assumed that the pulses have a Gaussian temporal profile. As shown in the figures 2.12(a) and (b), the pump spot that we use has a Gaussian spatial profile with a waist of 50 $\mu$m. Furthermore, in order to prevent thin film damaging, the pump spot has been enlarged compared to the case of cw excitation.

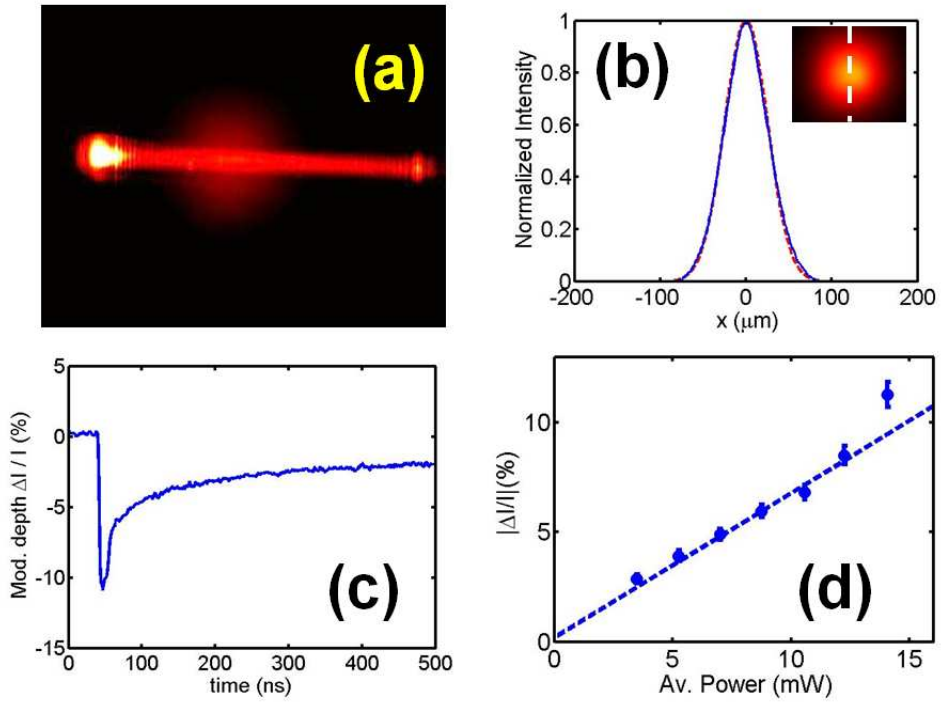


Figure 2.12: (a) Leakage radiation image showing the infrared plasmon jet and the nanosecond pump spot (b) Optical image of the pump spot. The cross-cut of the experimental intensity profile (solid line) of the pump beam is approximated by a Gaussian beam (dashed line) with a waist of 50 $\mu$m (c) Oscilloscope trace showing the photo-thermal modulation of the SPPs signal under the Q-switched nanosecond laser excitation. The average power is 14 mW (d) Depth of modulation of the SPPs signal as a function of the average power of the pulsed pump beam.

Figure 2.12 (c) shows the oscilloscope trace of the SPPs signal recorded for an average pump power of 14 mW. The modulation of the SPPs signal exhibits an asymmetric shape with an amplitude depth of 11.7 $\%$ resulting from the abrupt rise of the film temperature over the duration of the pulse and the much slower cooling after the end of the pulse. In the figure 2.12 (d), the modulation depth $\Delta I/I$ is displayed as a function of the average pump power. It should be noted that these experiments were conducted by increasing the pump power meaning that low pump powers were investigated first. The modulation depth depends linearly on the pump power until a threshold around 12.2 mW whereas the point obtained for 14 mW departs significantly from the linear behavior. This result is attributed to a change of the structural

properties of the metal film. This conclusion has been confirmed by a subsequent electron microscope characterization showing a clear change of the grain size of the film at the location of the pump spot center indicative of a possible partial melting of the film in this area which is shown in the figure 2.13. Disregarding the result obtained at 14 mW, we obtain a modulation efficiency corresponding to the slope of the linear fit displayed in the figure 2.12 (d) of 0.66 $\% \, mW^{-1}$.

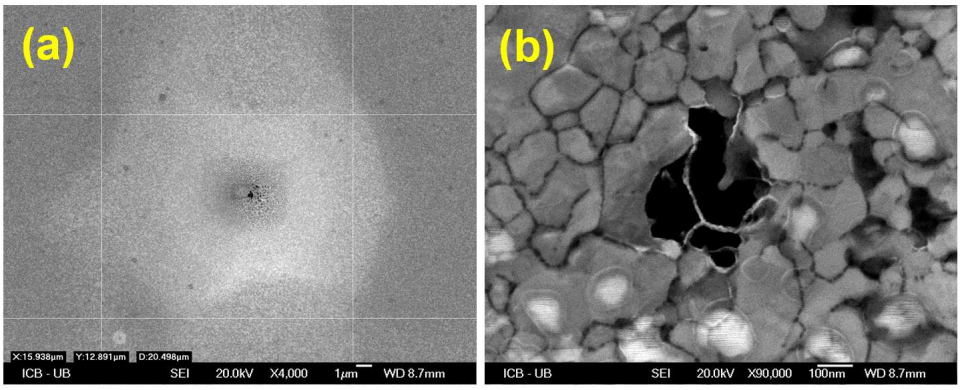


Figure 2.13: (a) Area of the gold film where the pump spot was incident with gradually increased powers that has caused to change the structure of the gold film and led to the formation of a thermal-hole displayed with a magnification of 4000x (b) The thermal-hole area shows unambiguously deterioration of gold grain structures imaged with a magnification of 90000x

The evaluation of the SPPs depth of modulation requires the computation of the temperature distribution in the system at any time during the pulsed illumination. For nanosecond pulses illuminating a particular metal surface, the free-electron gas and the lattice are already at thermal equilibrium after a characteristic time (10 ps) much shorter than the pulse duration. In this respect a two-temperature model (accounting for a temperature of the electron gas different from the ion lattice temperature) is not usually necessary in the pulsed nanosecond regime and the computation of the temperature can be conducted following the same procedure described for cw excitation.

Figure 2.14 (a) shows the temporal change of the gold film temperature at the center of the pump beam for an incident average power of 12.2 mW. The instantaneous power of the pump pulse for such an average power is displayed in the inset of the figure 2.14 (a). The heat source density resulting from the absorption of the pump beam follows the temporal profile of the incident pulse and thus the temperature rises over the pulse duration but decays at a rate controlled by the characteristic time for heat dissipation in the system. Knowing the temperature distribution at each time, the depth of modulation is computed according to the equation 2.23 with the thermo-plasmonic coefficient given by the equation 2.27. The experimental and computed temporal profiles are superimposed on the figures 2.14 (b) and (c) for incident powers of 12.2 mW and 10.6 mW respectively. In both cases, it can be noticed that modulation depths computed with our gold TOC values are slightly under-estimated compared to the experimental values. The computed modulation efficiency is shown in the figure 2.14(d) where the experimental depth of modulation is compared to the depth of modulation computed by using our gold TOC values. As expected, the computed depth of modulation increases linearly

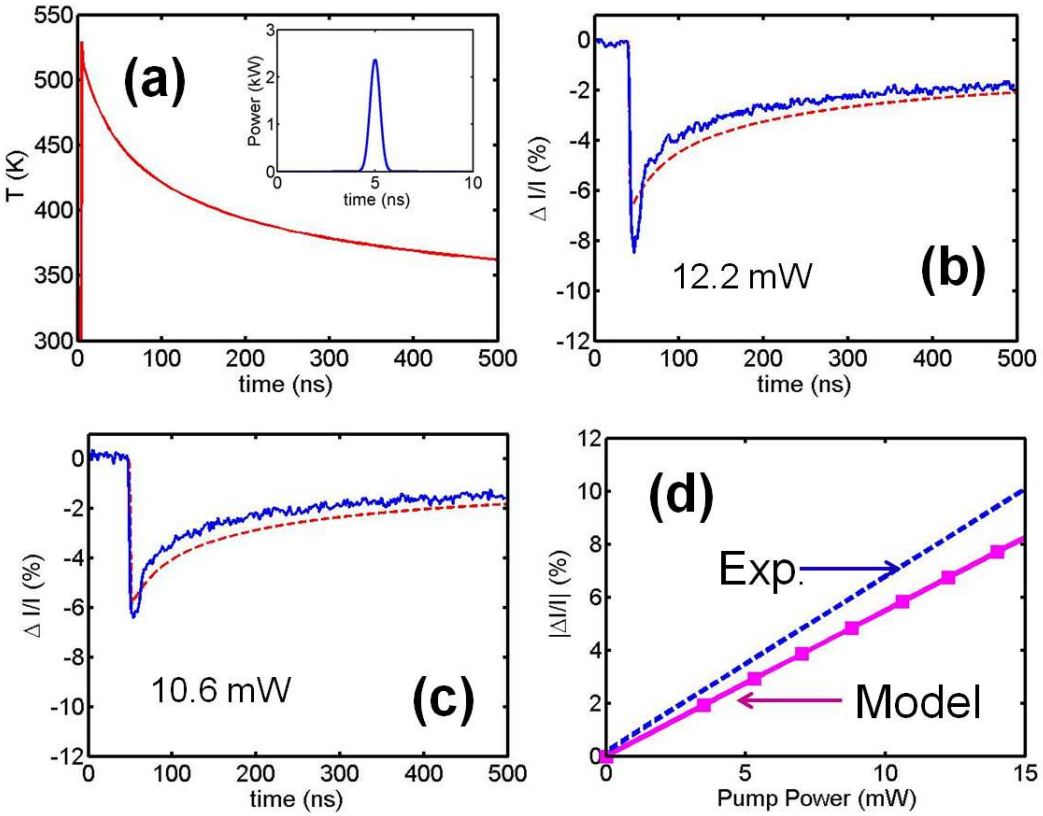


Figure 2.14: (a) Temperature of the thin film at the center of the pump beam in the case of an incident pulse with an average power of 12.2 mW, both repetition rate and pulse duration correspond to the experimental situation. The incident pulse reaches its maximum at t=5 ns as shown on the inset displaying the power of the pulse as a function of time (b) (resp. (c)) Comparison of the experimental (solid blue line) and computed (dashed red line) SPPs photo-thermal modulation for an average incident power of 12.2 mW (resp. 10.6 mW). The computed profile accounts for the 2 ns rise time of the infrared photo-diode response (d) Comparison of the experimental (dashed blue line) depth of modulation and the depth of modulation (solid pink line) computed using our gold TOC values.

with the pump power, at a rate of 0.55 $\%\ mW^{-1}$, smaller by about 17 $\%$ compared to the experimental rate. Such a discrepancy could be related to a pulse duration (which could not be measured experimentally due to the rise time of our visible photo-diode) slightly different than the specification.

A more accurate modeling of temperature distribution including a temperature-dependent absorption of gold film at the pump wavelength could also contribute to a better agreement between computed and experimental pulsed SPPs thermo-modulation. Nevertheless, in spite of this difference, it should be noted that the thermo-plasmonic properties of SPP modes supported by gold at telecom frequencies can be predicted with a fairly good accuracy by using the TO coefficients obtained in this work.

## 2.9 Conclusion

In this chapter, we have specifically investigated the thermo-optical modulation of a thin-film SPP mode propagation in the near-field infrared frequency range.

After a brief introduction on optical constant of metals and their dependence upon temperature, we have considered the experimental set-up along with the fabrication process of the samples used for the demonstration of photo-thermal SPP mode modulation.

The investigation of the photo-thermal modulation of thin film SPP mode launched at a gold/air interface at telecom frequencies is performed by operating a specific fiber-to-fiber detection configuration in conjunction with a leakage radiation microscope set-up. For a gold/air SPP mode at telecom frequencies, it is shown that the depth of modulation is proportional to the thermo-plasmonic coefficient defined as the temperature derivative of the damping constant of the mode. This coefficient is obtained in the case of a gold/air SPP mode by using the experimental depth of modulation and the temperature distribution along the film computed by means of a finite-difference scheme.

Moreover, we have proposed a figure of merit which can be useful to characterize the thermal properties of a metal at a given wavelength. Once established on the basis of the thermo-modulation of a given SPP mode, the figure of merit can be conveniently used for a rough evaluation of the thermo-plasmonic properties of other SPP modes provided that the losses of those modes are dominated by ohmic losses. By using our experimental results in conjunction with optical data available in the literature, we have computed the thermo-optical coefficients of gold at telecom wavelengths. These coefficients lead to a SPPs thermo-modulation amplitude about $60\%$ lower than predicted by the temperature-dependent Drude model for gold indicating that the temperature dependent Drude model can significantly deviates from the experimental situation.

Finally, we have checked the reliability of our gold TOCs by performing photo-thermal experiments with a pulsed nanosecond laser. Although the computed depth of modulation for pulsed illumination are underestimated by about $17\%$ compared to the experimental values, it should be concluded that the gold TOCs obtained in this work are reasonable and can be useful for anticipating thermal effects on SPP modes supported by gold at telecom wavelengths. Those thermal effects are actually critical and are expected in any non-linear experiment when a large amount of power is deposited into the metal or even in loss-compensation configurations when the optical pumping and potentially the electrical pumping in semiconductor gain media can be at the origin of a significant rise of the plasmonic metal temperature.

The next steps in the study of SPP mode photo-thermal control include the characterization of the temporal dynamic of the modulation in the case of plasmonic waveguides featuring a high field confinement and the use of pulsed photo-thermal excitation for the activation of fast thermo-plasmonic devices which will be demonstrated in the following chapter.

Chapter 3

# Nanosecond thermo-optical dynamics of polymer loaded plasmonic waveguides

## 3.1 Introduction

Thermo-optical (TO) effects are to date the most common way to control dynamically integrated plasmonic components such as variable attenuators [92, 141] and low bandwidth modulators [91, 142]. Initially implemented by using waveguided long-range surface plasmon modes [47], more compact thermo-optical plasmon based devices relying on dielectric loaded surface plasmon polariton waveguides [60, 64, 143] have been proposed [93, 94, 144] and demonstrated [16, 66, 67, 145]. So far, and most often, the dielectric loading material is a polymer deposited onto a metal film or strip and in this respect the waveguides will be denoted hereafter as polymer loaded surface plasmon polaritons waveguides (PLSPPWs).

Single-mode PLSPPW feature cross-sections with typical sub-micron dimensions enabling low-loss coupling with passive silicon-on-insulator circuitry [74, 146, 147]. The ability of integrating PLSPPW devices into a photonic passive circuitry has triggered the development and the demonstration of hybrid Si-PLSPPW thermally-activated routers for controlling high-bit rate traffic at the system level [12, 14, 15]. The key interest of the plasmon based devices in the context of thermo-optical control resides in the fact that the metal sustaining the plasmon mode can also be used as an heating electrode. However, photo-thermal activation of thermo-plasmonic devices is also an appealing approach. Indeed, this **all-optical** control offers the possibility to tune parameters such as the incident pump wavelength and/or polarization to optimize the TO devices activation [17].

Except when implemented with ultra-high quality factor resonators with corresponding narrow spectral range of operation [148], the main limitation of TO devices, whatever the material platform, is their moderate response times in the range of a few microseconds. For TO-PLSPPW routers integrated into a silicon on insulator circuitry, response times around 3-4 $\mu$s have been obtained [12, 14]. Although many dc or low-frequency characterizations of TO-PLSPPW devices have been reported, the dynamics of the thermo- optical response of these components has not been investigated in detail. It is therefore the main objective of this study to analyze experimentally and numerically the PLSPPW dynamics down to the nanosecond

time scale. For this purpose, we operate a photo-thermal excitation of the PLSPPW devices by using a Q-switched nanosecond pulsed visible (532nm) pump laser. The nanosecond pulse can be viewed, in the first approximation, as a delta-function excitation from which the overall TO dynamics of the PLSPPWs can be extracted. However, beyond PLSPPW TO dynamics, we also consider the use of nanosecond pulses for fast photo-thermal activation of our devices. In this context, the pulse is used as a pre-conditioning of the TO component by abruptly setting it into its hot state. Our approach can be viewed as the optical equivalent of the so-called "pre-emphasis driving" recently operated for fast reconfiguration of electrically driven silicon-based TO devices [149].

The chapter is organized as follows. The fabrication process of the samples as well as the experimental setup based on a combined leakage radiation microscope (LRM) and a fiber-to-fiber characterization scheme are briefly described in the following two sections. In the next section, we present our model of the PLSPPW TO response relying on a numerical computation of temperature distributions for a nanosecond photo-thermal excitation coupled to an effective index method. Afterwards, we investigate the thermo-absorption of a PLSPPW mode traveling along straight waveguides irradiated by nanosecond pulses in the section four. We demonstrate depth of modulations as large as 50% and we find that the presence of the polymer impacts the thermo-absorption dynamics at the sub-nanosecond scale. In this way, we show that the heat diffusion into the polymer over characteristic lengths around 20 nm is detectable from the PLSPPW properties. Next, we consider in the section five, the TO dynamics of photo-thermally excited PLSPPW racetracks resonators. We demonstrate that an activation of the resonators at a time scale of 300 ns followed however by a cool down characteristic time of about 18 $\mu$s. By analyzing the origin of these performances from the thermal properties of our polymer-based configuration, we conclude that nanosecond photo-thermal excitation is a convenient approach for the development of high-speed TO plasmonic devices.

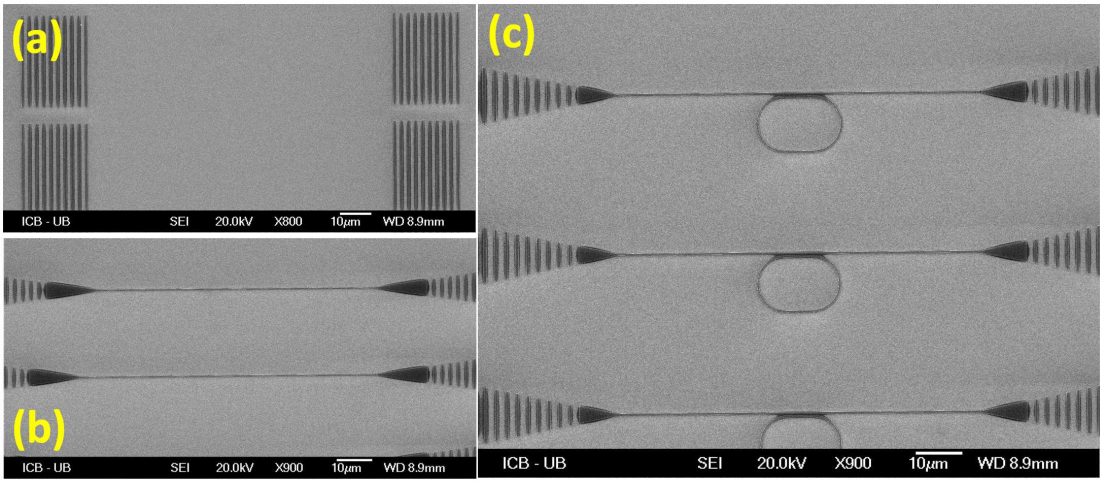


Figure 3.1: (a) Top view SEM images of (a) dielectric grating couplers at 800x magnification (b) Polymer loaded surface plasmon polariton waveguides (PLSPPWs) at 900x magnification (c) PLSPPW racetrack shaped resonators at 900x magnification which all are fabricated on thin gold film lying on a glass substrate

## 3.2 Nanofabrication of samples

The same fabrication methods, as described in chapter two, are used for the production of various PLSPPW samples basically comprised of patterned polymer at nanoscale. We fabricate three different samples for the TO characterization in our study such that in/out grating couplers for the excitation of air/Au SPP mode, PLSPPW consisting of grating couplers with a 100 $\mu$m waveguide section for the propagation of polymer/Au SPP mode and PLSPPW racetrack shaped resonators which all are displayed in the figure 3.1(a)-(b)-(c) respectively.

The samples we use in all the following are fabricated by electron beam lithography using a negative tone resist AR-N 7500 as the same before (from Allresist Co.) which is spin-coated at a speed of 1800 rotations per minute onto a gold film with a thickness of 70 nm deposited onto a 170 $\mu$m thick BK7 glass substrate. The design of the grating couplers for efficient excitation of SPPs depends on the same principle described earlier in the section "Electron-beam lithography" of the chapter two. Once this deposition is completed, the resist layer with a typical thickness of 600 nm is exposed to the electron beam at a dose of 170 $\mu$C/cm$^2$ under an acceleration voltage of 20 kV and eventually dissolved in a mixture of developer (AR 300-47: 4 vol) and DI water (1 vol) for 5 minutes to complete fabrication process.

## 3.3 Experimental setup

Figure 3.2 shows a schematic view of the experimental setup we use for the characterization of the PLSPPW nanosecond photo-thermal excitation. The setup is built up around a leakage radiation configuration [128] relying on an inverted microscope equipped with a high numerical aperture objective (1.49 NA) and a sensitive InGaAs camera. The samples mounted onto the microscope stage are excited by an infrared laser tunable over the C+L telecom bands. The infrared incident light is injected through a lensed-fiber producing a spot with a typical radius of 20 $\mu$m focused onto the input grating couplers of the PLSPPW device under test (DUT). The signal at the output of the DUT is scattered by a grating coupler and collected by the output focuser. With this configuration, insertion losses for PLSPPW samples in the range of 25-30 dB are typically achieved.

A visible pump spot (532 nm) produced by a Q-switched laser is directed at normal incidence onto the samples by means of a low magnification, long working distance objective which has been already introduced in chapter two. The Q-switched nanosecond laser has a pulse duration of 0.59 ns (full width at half maximum), a repetition rate of 8.3 kHz and a maximum energy per pulse of 6.5 $\mu$J. The thermo-optical activation of the PLSPPW devices is monitored by the infrared signal transmitted through the DUT. The output signal can be directed on two different photo-detectors. For short time scale measurements, the output signal is amplified with an erbium-doped fiber amplifier (EDFA), filtered to remove the spontaneous emission contribution and directed onto a 50 GHz photo-diode. The voltage of the 50 GHz photo-diode is next monitored by a real time 33 GHz bandwidth oscilloscope which is triggered by a visible photo-diode receiving a tiny fraction of the pump signal. For long timescale observations (in the range of several $\mu$s), the output signal is directed onto a 250 MHz (2 ns rise/fall time) sensitive photo-diode without optical amplification connected directly to a 1 GHz bandwidth oscilloscope.

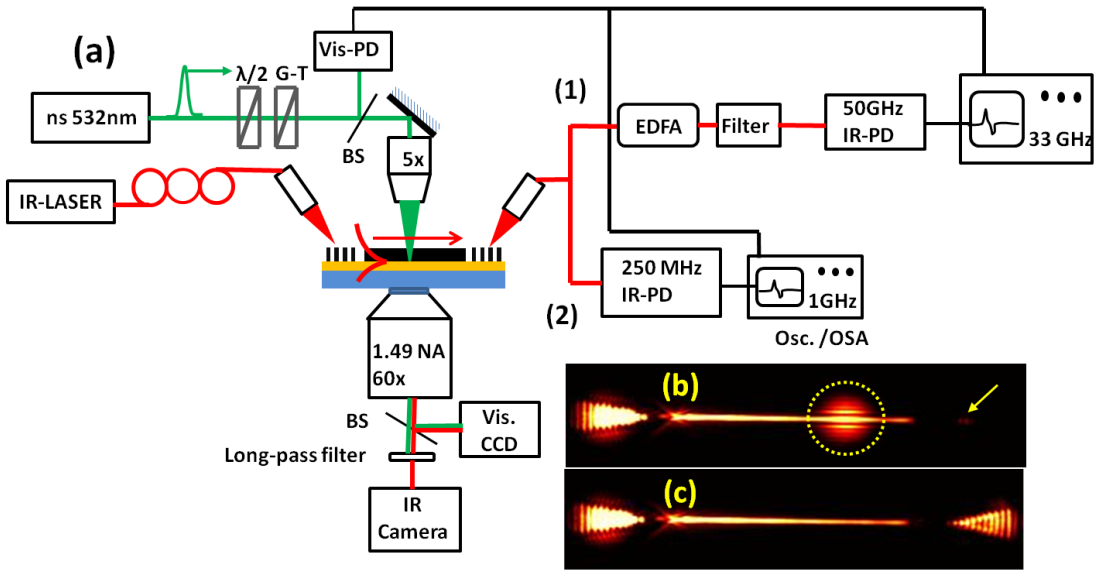


Figure 3.2: (a) Schematic view of the experimental setup combining a leakage radiation microscope and a fiber-to-fiber detection scheme. (b) and (c) Typical leakage radiation images recorded during the alignment procedure of the two lensed-fibers. (b) The infrared signal coupled by means of the left grating creates the output scattering spot shown by the arrow. For alignment purposes the output fiber is also coupled to another infrared source to generate the spot surrounded by the dashed perimeter. (c) At the end of the coarse alignment procedure, the spots generated by the input and output fibers are respectively located on the input and output grating couplers

Figures 3.2(b)-(c) show typical leakage radiation microscope images of a straight 100 $\mu$m-long PLSPPW. The main interest of leakage radiation microscopy in this study is to provide a very convenient way for the optimization of the input and output coupling at the cost however of the use of transparent substrates.

## 3.4 Thermo-optical modeling

When a nanosecond pulse irradiates a metal film, the temperatures of the free-electron gas and the lattice becomes thermal equilibrium after a characteristic time (typ. 10ps) much shorter than the pulse duration. Therefore, the use of a two-temperature model considering the lattice and the electron gas temperature separately is then usually not necessary in the nanosecond regime. In addition, if the characteristic heat diffusion times into the system are larger than phonons relaxation times (1ps), the classical Fourier's law holds and the thermal problem can be solved in the framework of classical heat diffusion theory. For simple configurations such as a semi-infinite absorbing medium illuminated by a pulsed Gaussian beam, analytical solutions exist. However, in our situation, these approximate solutions are not sufficient and a numerical approach is necessary. Numerically, we consider the two-dimensional (2D) situation schematically shown in the figure 3.3. The PLSPPW we consider is excited by a two-dimensional pulsed beam with a Gaussian intensity distribution in space (along x-axis) centered onto the z-axis. The pulse has also a Gaussian temporal profile. The temperature distribution of the sys-

tem under photo-excitation is obtained by solving the time-dependent heat diffusion equation such that

$$\rho(\vec{r})C_p(\vec{r})\frac{\partial T}{\partial t} = \tilde{Q}_E(\vec{r},t) + \vec{\nabla}\cdot(k(\vec{r})\vec{\nabla T}) \tag{3.1}$$

where $\rho$, $C_p$ and $k$ are the position dependent density, specific heat and thermal conductivity of each materials of the system. The source term $\tilde{Q}_E$ is the volume power density created by the absorption of the incident pulse and is given by [131]

$$\tilde{Q}_E(\vec{r},t) = \frac{1}{2}\omega\epsilon_0\epsilon''_m E^2(\vec{r},t) \tag{3.2}$$

where $\epsilon''_m$ denotes the imaginary part of the relative dielectric function of gold and where $E(\vec{r},t)$ is the electric field for observation points located within the gold film.

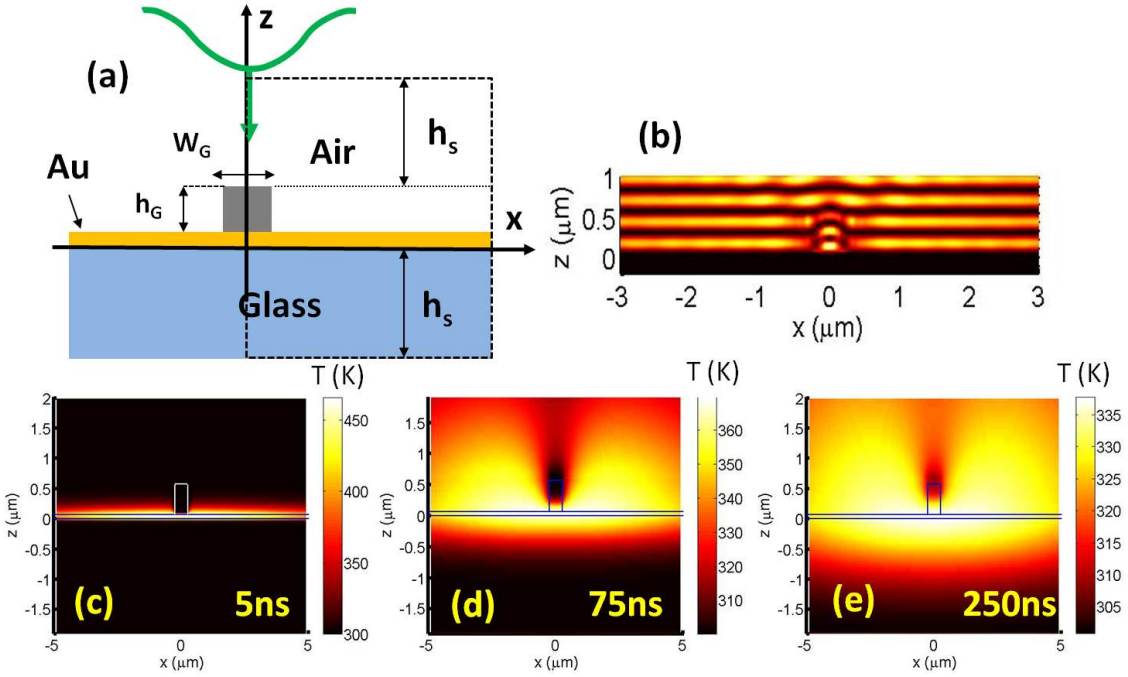


Figure 3.3: (a) Schematic view of the two-dimensional configuration for temperature distribution computation. The PLSPPW has a 0.5 $\mu$m$\times$0.5$\mu$m cross-section. The computation windows shown by the dashed line perimeter has a width of 35 $\mu$m and a total height $2h_s$=20$\mu$m and is discretized over up to 125$\times 10^3$ rectangular non-regular meshes. A Neumann condition ($\partial T/\partial x = 0$) is applied onto the $x = 0$ boundary in order to account for the symmetry of the configuration. Dirichlet conditions at the room temperature are applied on the three other boundaries. (b) Electric field distribution generated by the illumination of the PLSPPW by a Gaussian beam with a waist of 10 $\mu$m. (c)-(d)-(e) Temperature distribution in the PLSPPW for a 0.6ns-FWHM Gaussian pulse reaching its maximum in the metal plane at $t = 5$ ns

Figure 3.3(b) shows a typical example electric field intensity distribution computed with the differential method [150] in the case of 2D Gaussian beam with a waist $w_0$ =10 $\mu$m

illuminating a PLSPPW. The source term $\tilde{Q}_E(\vec{r},t)$ can be obtained readily from this intensity distribution and used to solve the equation 3.1. We compute the temperature distribution by using a non-regular rectangular mesh finite-difference implicit scheme with non-uniform time steps ranging from 50 ps to 100 ns depending on the delay with respect to the excitation pulse.

Figures 3.3(c) and 3.3(d) show typical temperature distributions computed at different times in the case of a 2D nanosecond pulse with temporal characteristics similar to the experimental case (pulse duration FWHM duration=0.59 ns, repetition rate 8.3 kHz) and a central fluence (at x = 0) of 4.8 mJ/cm$^2$. Once the temperature is known, the refractive index at each point is computed from the thermo-optical coefficients (TOCs) of each material listed in the table 3.1 along with their thermal parameters. Next the PLSPPW is divided into ten slices and the average refractive index of these slices is used to compute the complex propagation constant of the plasmonic waveguide mode from the effective index method [60] implemented on the basis of the reflection pole method [151]. In this way, we obtain the complex propagation constant of the PLSPPW mode as a function of temperature from which the TO dynamics can be extracted.

## 3.5 Thermo-absorption dynamics of PLSPP waveguides

The thermo-modulation of the signal intensity transmitted through a straight PLSPPW is mediated by the temperature dependence of the PLSPPW mode damping constant. Many works have been devoted to the thermally induced change of the real effective index of PLSPPWs (thermo-optical effect) but so far and to the best of our knowledge, none of them have addressed the temperature dependence of the PLSPPW mode imaginary effective index (thermo-absorption effect). So this dependence deserves a careful examination due to the remarkable impact on the performances of PLSPPW devices in practical applications.

| Material | $\rho$ [ kg/m$^3$ ] | $C_p$ [ J/kg K ] | k [ W/K m ] | $n+i\kappa$ | $\partial_T n+\partial_T \kappa$ [ 1/K ] |
|---|---|---|---|---|---|
| Glass | 2500 | 500 | 1.4 | 1.5 | NA |
| Polymer | 1200 | 1500 | 0.15 | 1.5 | -1.0x10$^{-4}$ |
| Air | 1.2 | 1005 | 0.024 | 1.0 | NA |
| Gold | 19300 | 129 | 150 | 0.55+10.7$i$ | (0.72-1.0$i$ ) x10$^{-3}$ |

Table 3.1: Thermal and optical parameters of the materials used in our thermo-optical model are listed above. It should be noted that the data taken into account for the thermal (or heat) conductivity coefficient of the gold thin film is smaller than the bulk's one [137] and besides the gold TOCs employed here has been extracted from our previous results [140]

Waveguiding in a PLSPPW results from the combined actions of metal and polymer from which the vertical and lateral field confinement of the guided mode originates respectively. These two materials are then expected to contribute to the thermo-optical properties of a

PLSPPW. At this stage, it is instructive to refer to the situation of a SPP mode traveling at an interface between a metal and a dielectric. At telecom wavelengths, metal of interest for plasmonic applications are such that where $|\epsilon_m^{'}| \gg \epsilon_m^{''}$ where $\epsilon_m^{'}$ and $\epsilon_m^{''}$ are the real and imaginary part of the relative dielectric function of the metal. The relative dielectric function $\epsilon_d$ of typical dielectric media such as standard polymers is also small compare to $|\epsilon_m^{'}|$ in such a way that the temperature derivative of the SPP mode damping constant $k_{spp}^{''}$ is given by [34]

$$\partial_T k_{spp}^{''} = k_{spp}^{''}\Big(\frac{3}{2}\frac{\partial_T \epsilon_d}{\epsilon_d} + \frac{\partial_T \epsilon_m^{''}}{\epsilon_m^{''}} - 2\frac{\partial_T \epsilon_m^{'}}{\epsilon_m^{'}}\Big) \tag{3.3}$$

where the notation $\partial_T$ is used in place of $\partial/\partial_T$.

The metal contribution to the SPPs thermo-absorption is not only mediated by the ohmic losses (through $\partial_T \epsilon_m^{''}$) but also by the temperature dependent $\epsilon_m^{'}$. At telecom wavelengths, where the dielectric function of noble metals are dominated by the free-electron contribution, the ohmic losses depend on temperature mostly through the electron-phonon scattering rate whereas a change of the free-electron density resulting from a thermally induced lattice volume expansion is at the origin of the $\partial_T \epsilon_m^{'}$ coefficient.

The dielectric medium also contributes to the SPPs thermo-absorption through the change of the SPPs field confinement within the metal which depends on $\partial_T \epsilon_d$. For a PLSPPW with a complex geometry, the respective contribution of the metal and the dielectric to the thermo-absorption effect is difficult to estimate. It is then useful to investigate first a situation where the dielectric medium contribution is expected to be negligible such as in the case of a SPP mode traveling at a gold/air interface.

The Au/air SPPs is coupled in and out using dielectric grating couplers separated by a distance of 100 $\mu$m (see fig. 3.4(a)) and designed according to the approach described in chapter two [121]. A very similar configuration has been previously used to extract the thermo-optical coefficients (TOCs) of gold given in table 3.1 [140]. Typical leakage radiation images of the SPPs jet launched by the input grating couplers are shown in the figure 3.4(b) and 3.4(c) with the pump spot respectively off and on. And figures 3.4(d)-(f) show the oscilloscope traces at different time scales of the Au/air SPPs signal thermo-modulated by a Gaussian pump beam with a waist of 50 $\mu$m. For this experiment, the average pump power was 5.6 mW ($Ep$=0.68 $\mu$J/pulse) corresponding to a fluence at the center of the Gaussian beam of $F = E_p/(\pi w_r^2)$ =8.5 mJ/cm$^2$ far below the damage threshold (140 mJ/cm$^2$ [152]). The normalized signal plotted in Figs.3.4(d)-(f) is defined as $S_N = 1 - V(t)/V_M$ where $V(t)$ is the ac-coupled voltage measured at the output of the photodiode and where $V_M$ denotes the maximum modulation amplitude. For the 5.6 mW pump power, $V_M$ is only 3.7% of the cold state transmitted SPPs signal for a maximum thin film temperature rise at the center of the pumped beam evaluated at 87 K by solving numerically the heat diffusion equation in cylindrical coordinates [140]. For the Au/air SPP mode, the modulation amplitude is given by $V(t) \propto I^c(y_{out})(1 - \exp(-2\partial_T k_{spp}^{''} \int_0^{y_{out}} \Delta T_f(y', t)dy'))$ [140] where $I^c(y_{out})$ is the electric field intensity of the SPPs jet in the cold state at the location of the output grating $y_{out}$ and $\Delta T_f(y', t)$ is the temperature rise in the gold film along the SPPs propagation pathway. The argument of the exponential in the definition of $V(t)$ being small, the normalized signal $S_N$ can be approximated by

$$S_N = 1 - \frac{\int_0^{y_{out}} \Delta T_f(y',t)dy'}{max(\int_0^{y_{out}} \Delta T_f(y',t)dy')} \tag{3.4}$$

Thus, for a SPP mode traveling at the interface between the metal and a dielectric with negligibly small TO coefficient, the thermo-absorption of the transmitted SPPs signal is characteristic of the thin film temperature change accumulated over the SPP mode propagation distance. By using the profile displayed in the figure 3.4(d), we measure a 90%-10% fall-time of $\tau_F$ = 1.0 ns indicating that the thin film temperature changes at the time scale of the pulse duration. On the other hand, the 10%-90% rise-time evaluated from the stretched exponential fit of the experimental [153] profile displayed in the figure 3.4(f) is measured at $\tau_R$ = 3.1 $\mu$s.

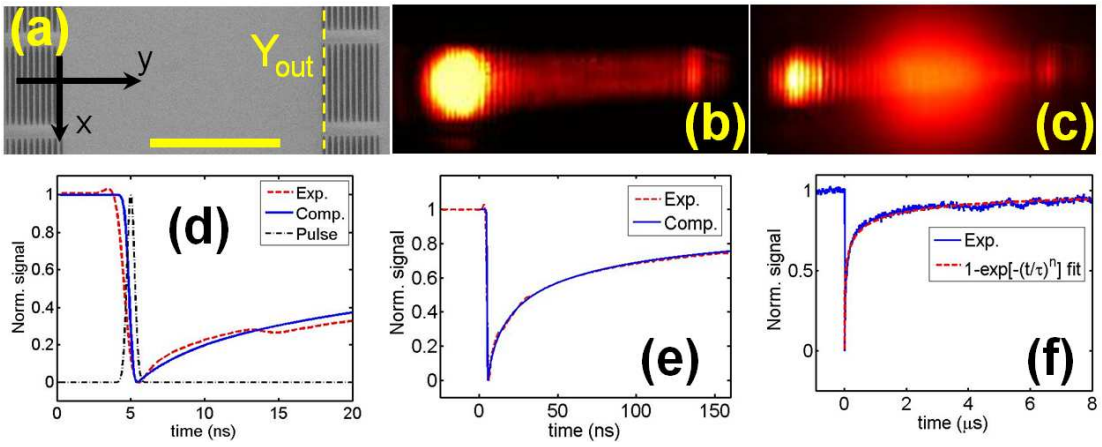


Figure 3.4: (a) Scanning electron microscope (SEM) image of the in and out grating couplers (scale bar=50 $\mu$m). (b) (resp. (c)) Typical leakage radiation microscope images of the plasmon jet (at $\lambda$ = 1540 nm) propagating at the Au/air interface with the pump beam off (resp. on, cut-on filter off). The pump spot features a Gaussian intensity distribution in $I(r) = I(0)\exp[-(r^2/w_r^2)]$ with a waist of $w_r$ = 50 $\mu$m. (d)-(e)-(f) Observation of the thermo-absorption of the SPPs signal under the nanosecond excitation at different time scales. In (d) and (e), the dashed lines are the experimental signal whereas the solid lines are the computed thermo-absorption profiles for an interface SPPs. The dashed-dotted line in (d) shows the temporal profile of the incident pulse used in the calculations

As discussed in the following, the value of $\tau_R$ depends on the ability of the system to dissipate heat and can be decreased down to the sub-$\mu$s regime by choosing a proper design. The thermo-absorption of the Au/air SPPs is compared in the figures 3.4(d) and 3.4(e) to the computed TO response following the approach described in the previous section. Our model underestimate the fall-time by about 0.5 ns compared to the experimental value. On the other hand, we note a very good agreement between experimental and computed profiles for the cooling process. The discrepancy of the computed and experimental results at very short time scale (a few nanoseconds) is not fully understood but could be related to a specific heat diffusion regime at the interface between the metal film and the glass substrate. Despite these differences, we note that our model can predict quantitatively the dynamics of the thermo-absorption process (at least for times larger than a few nanoseconds after the pulse) and then can be safely used to anticipate the TO response of other plasmonic devices at the sub-$\mu$s scale.

In Fig. 3(e), we observe a small increase of the transmitted signal right before the thermally induced abrupt signal drop. This increase, which is not visible onto the computed profile, could be due to a slight improvement of the in and out coupling conditions of the polymer gratings for a moderate temperature rise.

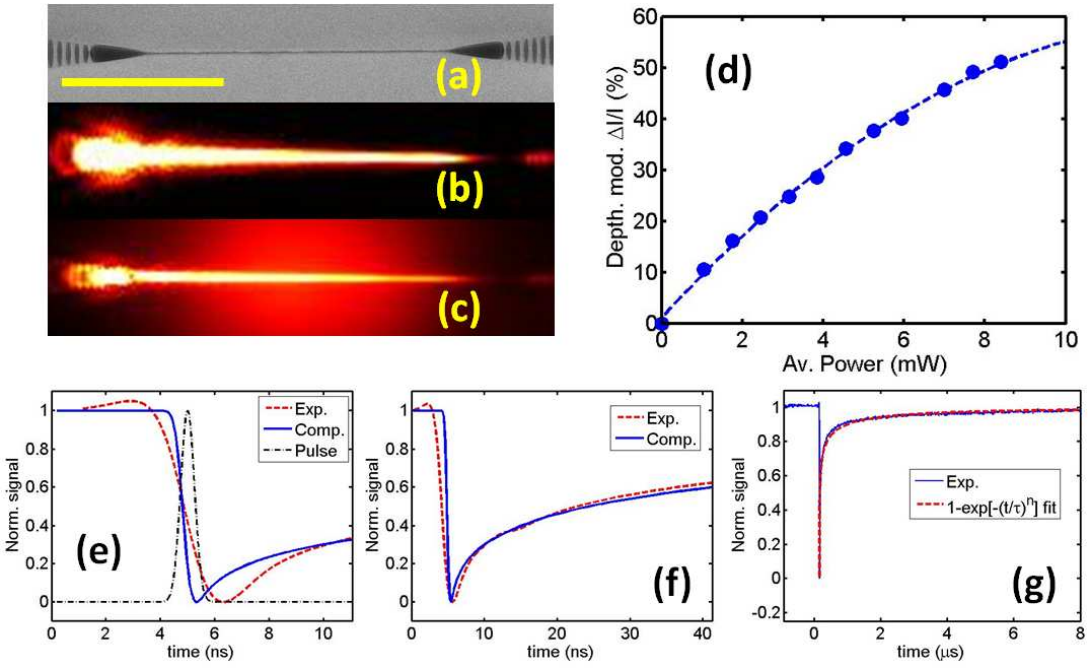


Figure 3.5: (a) Scanning electron microscope (SEM) image of a typical PLSPPW equipped with grating couplers (scale bar = 40 $\mu$m). (b) (resp. (c)) Leakage radiation microscope images of the PLSPPW mode (at $\lambda$ = 1530 nm) propagating at the polymer/gold interface with the pump beam off (resp. on, cut-on filter off). The excitation conditions are the same as in the figure 3.4. (d) Depth of thermo-absorption of the PLSPPW mode as a function of the incident average pump power. The depth of modulation is defined with respect to the signal level in the cold state. (e)-(f)-(g) Experimental and computed thermo-absorption of the PLSPPW signal under nanosecond excitation at different time scales. The solid lines are computed profiles whereas the dashed lines are experimental profiles. The dash-dotted line in the figure 3.5(e) is the profile of the excitation pulse used in the calculations

We consider now the situation of a straight PLSPPW photo-thermally excited by the nanosecond pulsed beam. The excitation conditions are the same as for the interface SPP mode. Figures 3.5(a)-(c) show respectively a scanning electron microscope image of the straight PLSPPW as well as a typical radiation leakage image of this waveguide with the pump spot off and on. Although we focus in this work onto the dynamics of the TO response of PLSPPWs, it is worth to consider first the curve displayed in the figure 3.5(d) showing the depth of modulation of the signal collected at the output of the PLSPPW as a function of the average pump power. For an average pump power of 5.6 mW, the depth of modulation is about 38% of the cold state signal amplitude, up to ten times larger than in the case of the interface SPPs. This difference can be understood from the larger field confinement within the metal (and accordingly the shorter propagation length) for the PSLPPW mode compared to the SPP

mode [140].

Figures 3.5(e)-(g) show the normalized signal $S_N$ recorded at different time scales. On the basis of the profiles displayed in the figures 3.5(e)-(g), we find that the fall-time for the thermo-absorption of the PLSPPW mode is $\tau_F$ = 1.7 ns and the sub-$\mu$s rise-time drops at $\tau_R$ = 800 ns respectively two times longer and four-fold shorter than in the case of the interface SPP mode. For a PLSPPW, the normalized signal $S_N$ does not follow anymore the dynamics of the metal film temperature but results from the combined contributions of the metal and polymer as illustrated by the equation 3.3. The activation time for the thermo-absorption of PLSPPWs can be explained from a slower thermalization of the gold film in the presence of the polymer but also from its negative TOC. The typical heat diffusion length for the pulse duration $\tau_p$ is $L = 2\sqrt{\alpha\tau_p}$ [154] where $\alpha$ is the thermal diffusivity $\left(\alpha = k/(\rho C_p)\right)$ of the material of interest. In our situation $\left(\alpha_{poly} = 8.3{\times}10^{-8}\,\mathrm{m^2s^{-1}}, \tau_p \simeq 1\,ns\right)$, the heat diffusion length into the polymer is around 20 nm. At the nanosecond scale, the temperature rise of the polymer generates a thin low index layer in contact with the metal film leading to a decrease of the PLSPPW mode field confinement into the metal and a corresponding increase of its propagation length. Hence, during the heating cycle, the increase of the metal losses is partly compensated by the PLSPPW mode field delocalization resulting in a longer activation time of the PLSPPW thermo-absorption process than for the Au/air SPPs mode. At longer times, after the pulse, the temperature of the metal film drops and the propagation length of the PLSPPW mode increases accordingly. However the rise-time $\tau_R$ for PLSPPWs being about four times shorter than for the Au/air SPPs, we conclude that the polymer still contributes to the increase of the PLSPPW damping distance during the cooling cycle.

Once again, we note that our model fails to capture the dynamics of the thermo-absorption during the first nanoseconds whereas computed and experimental profiles are in good agreement for times larger than 5 ns after the pulse. From these results, we conclude that our model is reliable for time scales larger than 10 ns which is still of key interest to predict the performances of high bandwidth thermo-plasmonic devices. The assessment of the characteristic time for the polymer contribution to the TO PLSPPW dynamics is difficult to complete from thermo-absorption experiments owing to the metal contribution and requires the use of frequency resonant devices.

## 3.6 Thermo-optical dynamics of a PLSPPW ring resonator

We have identified in the previous section the role of the polymer in the dynamics of the thermo-absorption of a PLSPPW mode by comparison with a reference Au/air SPP mode. To push further this qualitative analysis, we consider now the thermo-optical response of a PLSPPW based resonator. Prior to the discussion of the experimental results, we evaluate the respective contribution of the metal and polymer in this context by considering once again the situation of the interface SPP mode. At telecom wavelengths, the temperature derivative the SPP phase constant can be approximated by

$$\partial_T k'_{spp} \simeq \frac{k'_{spp}}{2(\epsilon'_m + \epsilon_d)} \left( \frac{\epsilon_d}{\epsilon'_m} \partial_T \epsilon'_m + \frac{\epsilon'_m}{\epsilon_d} \partial_T \epsilon_d \right) \tag{3.5}$$

The metal contribution to the PLSPPW TO coefficient is roughly two orders of magnitude

smaller than the dielectric contribution in such a way that the thermally-controlled properties of a PLSPPW based resonator can be interpreted in terms of polymer properties only. The resonators that we consider are racetrack resonators excited by a straight bus waveguide (see fig.3.6(a)). Plasmonic switches relying on optimized racetrack resonators have been already demonstrated in the reference [66] and the opto-geometrical parameters we use are directly inspired from this previous study. The resonator that we consider features well pronounced resonances as illustrated by the leakage radiation images recorded at 1560 nm (see fig.3.6(b)) and 1565 nm (see fig.3.6(c)).

The spectral properties of the resonator have been characterized by exciting the bus waveguide with a broadband spontaneous emission source and by collecting the output signal with an optical spectrum analyzer. The normalization of this first spectrum by the spectrum of a reference waveguide (without resonator) leads to the spectrum displayed in the figure 3.6(d). We focus onto the resonance centered at 1538 nm located within the optimum amplification band of the EDFA.

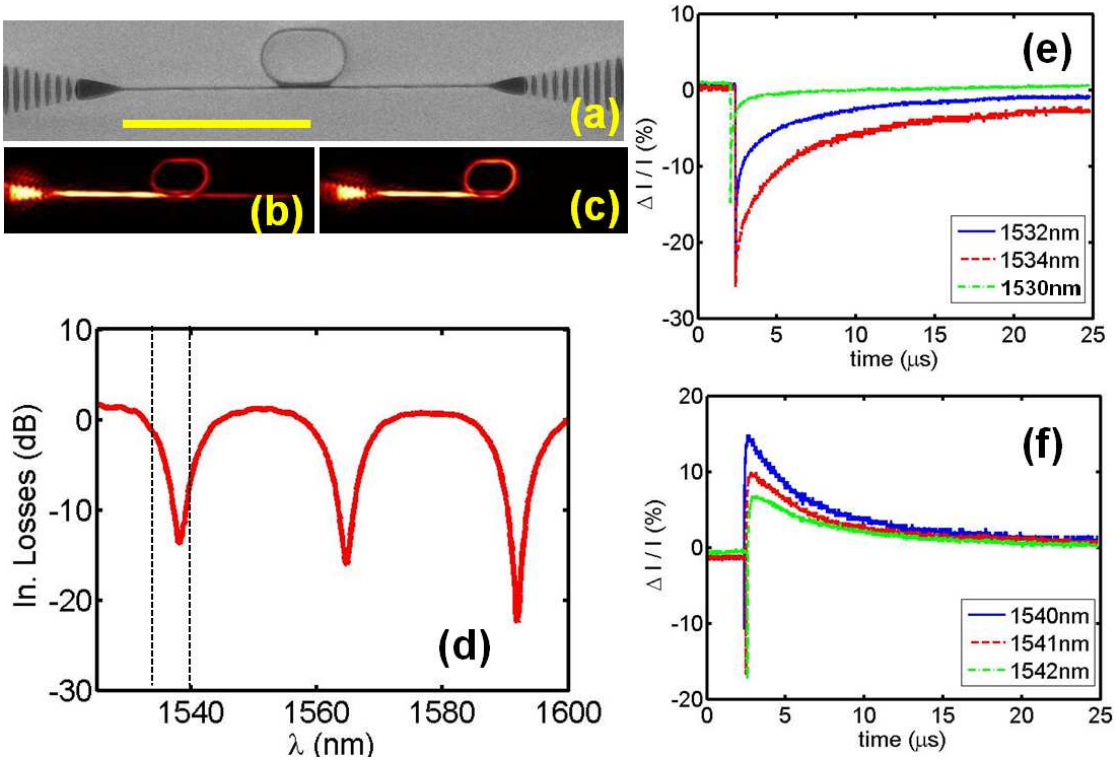


Figure 3.6: (a) Scanning electron microscope (SEM) image of the racetrack shaped resonator coupled to a straight bus waveguide (scale bar = 40 $\mu$m). The radius of the resonator is R = 5.5 $\mu$m, straight interaction length with the bus waveguide is 6 $\mu$m long and the nominal gap between the resonator and the bus waveguide is 250 nm. (b) (resp. (c)) Leakage radiation microscope image of the resonator at 1560 nm (resp. 1565 nm). (d) Cold state spectrum of the resonator. (e) (resp. (f)) Thermo-optical response of the resonator under ns excitation for blue-detuned (resp. red-detuned) wavelengths compared to the cold state resonance of 1538 nm. The photo-excitation is achieved with a large pump spot exciting simultaneously the resonator and the bus waveguide

The resonator is photo-thermally excited using a pump spot with a waist of 50 $\mu$m (average power 5 mW) illuminating the bus waveguide and the resonator simultaneously. Figures 3.6(e) and 3.6(f) show the time resolved signal modulation for wavelengths located respectively on the blue and red side of the central resonance wavelength (in the cold state). For wavelengths corresponding to a blue detuning, the photo-excitation leads to an abrupt drop of the signal followed by a slower signal rise. For those wavelengths the modulation is negative indicating that the signal in the hot state is lower than in the cold state. For a red detuning, we observe first a very sharp signal drop followed by a positive modulation of the signal at longer time scales. These results clearly indicate that the resonator has been photo-activated by the nanosecond pulse. Indeed, the polymer we use having a negative TOC, the spectrum of the resonator blue-shifts in the hot state causing the positive (resp. negative) modulation for red detuned (resp. blue detuned) wavelengths. For red-detuned wavelengths, the sharp drop of the signal is due to the thermo-absorption of the PLSPPW mode investigated in the previous section. For blue detuned wavelengths, the negative modulation of the signal can be unambiguously attributed to the heating of the polymer and not to the ohmic losses of the heated metal film. Indeed, the time scale for the signal rise after the excitation in the figure 3.6(e) is much slower for 1532 nm and 1534 nm than for 1530 nm for which the spectral response of the resonator is flat.

With this experiment, we show that nanosecond photo-thermal activation of plasmonic devices is possible and could be of practical interest for high-bandwidth thermo-optical devices. However in our situation neither the amplitude nor the dynamics of the optical response is sufficient to target such an application. Indeed, by increasing the average pump power up to 10 mW slightly below the damage threshold of the resonator, we could achieve a positive depth of modulation of $\Delta I/I = 25\%$ at 1541 nm, corresponding to a resonance detuning of only 0.6 nm, insufficient for switching with a low quality factor plasmonic resonator. Nevertheless, future designs of thermo-plasmonic devices activated in the nanosecond regime can greatly benefit from an analysis of the limited performances of the polymer based devices.

Figures 3.7(a) and 3.7(b) show the TO response of the photo-activated resonator at different time scales. The thermo-absorption of the PLSPPW mode occurring at a scale of 2 ns, the abrupt drop of the signal in the figure 3.7(a) is a reliable indication of the pump pulse arrival time from which the dynamics of the resonator can be accurately measured. The profile displayed in the figure 3.7(a) indicates that the characteristic activation time for the PLSPPW resonator is $\tau_R$ = 280 ns followed by a much longer relaxation time. We measure a 90%-10% fall time of $\tau_F$ = 18 $\mu$s on the profile shown in the figure 3.7(b).

The average temperature in the polymer and the metal film are plotted in the figure 3.7(c) for the PLSPPW excited in the same conditions as in the figure 3.3. The polymer slice in contact with the metal film, which is expected to contribute dominantly to the TO properties of the PLSPPW, reaches a maximum temperature (averaged over a thickness of 125nm) of only one fourth of the maximum metal film temperature. For slices at larger distances from the metal film, the temperature is maximum after a time characterizing the diffusion speed of the thermal pulse. The time dependent PLSPPW effective index $n_{eff} = k'/k_0$ ($k_0 = 2\pi/\lambda_0$, $\lambda_0$=1541 nm) plotted in the figure 3.7(d) has been obtained by means of the effective index method with the refractive index of each polymer slice evaluated from the temperature profiles of the figure 3.7(c). The minimum effective index is reached 200 ns after the excitation pulse, in reasonable agreement with the experiment given that no adjustable parameter is used for this calculation.

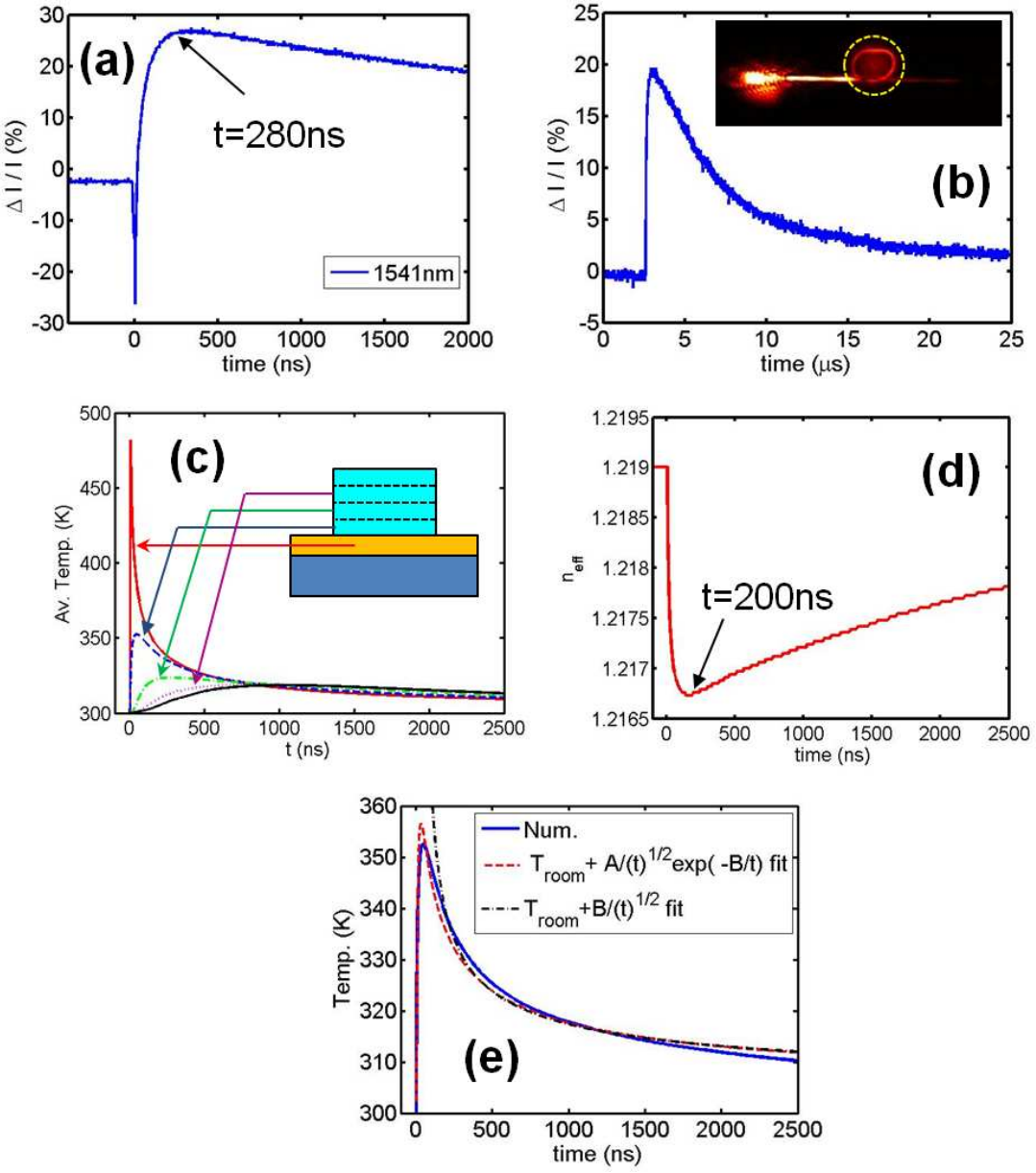


Figure 3.7: (a) Photo-thermal excitation of the resonator for a red-detuned signal wavelength (1541 nm). The photo-excitation is achieved by using a large spot ($w_r$ = 50 $\mu$m) exciting the resonator and the bus waveguide (average power 7 mW). The abrupt drop of the signal at t = 0 results from the thermo-absorption of the bus-waveguide mode and indicates the arrival time of the incident pulse. The activation (or heating) time of the resonator is 280 ns. (b) Long-time scale TO response of the resonator pump by a focused beam ($w_r \simeq 5\,\mu$m, see the inset) with an average power of 150 $\mu$W. With the local excitation of the resonator, the thermo-absorption is not observed anymore. The characteristic cooling time is 18 $\mu$s. (c) Comparison of the average temperature into the gold film and polymer slices of the PLSPPW with a thickness of 125 nm for the photo-excitation by a nanosecond pulse (0.6 ns FWHM) arriving onto the PLSPPW at t = 5 ns. (d) Computation of the effective index of the PLSPPW mode from the temperature profiles displayed in (c). (e) Comparison of the average temperature profile of the first polymer slice (125 nm) in contact with the metal film and different fit models inspired by the equation 3.6

The thermo-optical activation of the PLSPPW occurs at sub-$\mu$s time scale whereas the cooling time is clearly the main limitation to high-speed operation. Indeed, the cooling time for the thermo-optical response of the ring resonator is about 20 times larger than the thermo-absorption relaxation time along a straight PLSPPW. This difference results from the fact that the thermo-optical response depends upon the polymer temperature only whereas for thermo-absorption, the temperature of the metal film plays the dominant role.

Beyond the numerical modeling, the physical quantities of interest for improved TO performances can be more conveniently identified from an approximate analytical model. When a short pulse with a fluence $F$ is fully absorbed at $t$ = 0 within a very thin layer at the surface of a semi-infinite medium occupying the $z$ > 0 half-space, the temperature rise in the material at a distance $z$ from the surface is approximated by [155]

$$\Delta T(z,t) = \frac{F}{\epsilon\sqrt{\pi t}} \exp\left(\frac{-z^2}{4\alpha t}\right) \tag{3.6}$$

where $\epsilon = \sqrt{k\rho C_p}$ is the thermal effusivity of the semi-infinite medium. We assume that the TO properties of the PLSPPWs can be analyzed from the temperature of a characteristic polymer slice located at a distance $z_{eff}$ from the surface of the metal film. For typical PLSPPW heights of 500 nm, a reasonable choice for this effective distance is around $z_{eff}$ = 250 nm. According to the equation 3.6, the temperature at $z_{eff}$ reaches its maximum value $\Delta T_{max}(z_{eff}) \propto F/(\rho C_p z_{eff})$ at $t = \tau_H = z_{eff}^2/(2\alpha)$ = 280 ns in perfect but fortuitous agreement with the experiment. From this approach, we conclude however that a high thermal diffusivity of the TO active medium is the key parameter for the fast activation time of PLSPPW devices.

The average temperature of the polymer slice in contact with the gold layer computed numerically is compared to fit models inspired by the equation 3.6 in the figure 3.7(e). We note that during the cooling cycle, the contribution of the exponential term in the equation 3.6 can be neglected in the first approximation. From this further approximation, one can show that the typical cooling time $\tau_C$ needed for the temperature at $z_{eff}$ to decrease from 90% to 10% of $\Delta T_{max}(z_{eff})$ is given by $\tau_C \simeq \left(100\,\pi\,e\,z_{eff}^2\right)/\left(2\,\alpha\right)$. Although this equation leads to a cooling time about five-fold overestimated compared to the experiment, the diffusivity $\alpha$ appears to be once again the main parameter for controlling the cooling dynamics of the system. However, the response time is not the only parameter that should be considered in a practical device. As pointed out recently in the reference [95], the dynamics of electrically driven TO PLSPPW devices is improved at the expense of larger activation powers. For photothermal excitation, such an increase can be minimized by a stronger focusing of the pump beam at least in the case of small footprint devices. In addition, the equation 3.6 indicates that the heating efficiency scales as the inverse of the thermal effusivity of the material. Combining this requirement to the large thermal diffusivity needed for high-speed operation, we conclude that the optimum material in this context should have a large thermal conductivity $k$ and a small $\rho C_p$ product.

The above analysis has been conducted considering heat diffusion in the TO active medium whereas in the experimental situation the role of the substrate is also critical. The conclusions given for the TO material also applies for the substrate which should feature a high thermal diffusivity as well. In addition, the thermal diffusivities and effusivities of the TO medium and

the substrate should also be close in order to prevent a poor heating of the TO medium as in our configuration (see fig.3.7(c)) where heat diffusion is four times faster in the glass substrate than in the polymer load.

On the basis of this analysis, we conclude that PLSPPW based TO devices operating in the sub-$\mu$s regime will be difficult to implement with standard polymers mostly due to their poor thermal diffusivity. In spite of their thermal properties, it is worth to note that sub-$\mu$s switching operations with PLSPPW based TO devices are achievable at the cost however of the implementation of sophisticated configurations such as a push-pull Mach-Zehnder interferometer. Indeed, for the latter, the switching speed is given by the typical activation time of each arm in the interferometer (in the range of 300 ns in our case) whereas the relaxation time (several $\mu$s with PLSPPWs) imposes the switch latency [156]. Nevertheless, provided that high-speed TO devices are targeted, the polymer and the glass substrate used in this study must be replaced by highly thermally diffusive materials such as semi-conductors. For example, heat diffusivity of silicon ($\alpha \simeq 8 \times 10^{-5}\mathrm{m}^2\mathrm{s}^{-1}$) is about three orders of magnitude larger than the polymer used in this study suggesting that the bandwidth of the TO semi-conductor loaded plasmonic devices could be extended up to several MHz.

## 3.7 Conclusion

In summary, we have experimentally and numerically investigated the dynamics of the thermo-modulation of PLSPPW devices photo-excited by nanosecond pulses. By operating a fiber-to-fiber detection scheme, we have demonstrated a response time for the thermo-absorption of the PLSPPW mode in the nanosecond regime at the scale of the pulse duration. Whatever the time scale, we have shown that the thermo-absorption of the PLSPPW mode is mediated not only by the temperature-dependent metal ohmic losses but also by the field distribution of the PLSPPW mode into the metal controlled by the polymer TOC. For a negative TOC, we observe a sub-$\mu$s thermo-modulation characteristic time (fall-time+rise-time) about four-fold shorter than the cooling time of the metal film itself. In addition, we find that the thermo-absorption amplitude for a PLSPPW mode is about 10 times larger than for a Au/air interface SPPs photo-excited in the same conditions. On the basis of these results, we conclude that the thermo-absorption effect significantly impacts the performances of the PLSPPW based TO devices.

Next, we have considered the thermo-optical response of PLSPPW racetrack resonators featuring well pronounced resonances. By choosing a signal at the wavelength either blue or red detuned compared to the cold state resonance, we have shown that the nanosecond pulse can activate the resonator at a time scale of 300 ns however followed by a characteristic cooling time of about 18 $\mu$s in our configuration. The slow TO dynamics of these resonators is attributed to the poor thermal diffusivity of both the polymer and the glass substrate used in this study. In spite of these poor thermal performances, we note that the nanosecond photo-thermal excitation is convenient for sub-$\mu$s activation which is the key feature for the fast pre-conditioning of the TO devices.

Finally, it should be also pointed out that, as long as the metal of the plasmonic devices is used as the heat transducer for electrical or optical driving, the TO plasmonic devices will suffer from the detrimental effect of thermo-absorption of the plasmon mode and from the time delay imposed by heat diffusion from the metal to the thermo-optically active material. Inter-

estingly, we note that photo-thermal excitation offers the unique possibility to circumvent all these limitations by localizing the absorption of the incident light within the TO active medium rather than in the metal. By combining the nanosecond pulsed photo-thermal approach to the use of inorganic materials featuring all high thermal diffusivity, TO plasmonic devices with several MHz bandwidths turn to be achievable.

Chapter 4

# Nanowire SPPs photo-thermal modulation at telecom wavelengths

## 4.1 Introduction

Waveguiding along plasmonics waveguides does not rely on refractive index contrast as in the case of standard photonic waveguides. This property makes it possible for plasmonic waveguides to outperform conventional waveguides in terms of footprint and compactness. Among many plasmonic waveguiding configurations, nanowires have attracted much interest as they can be fabricated by standard techniques such as not only electron beam lithography [157] but also chemically grown [80]. Lots of theoretical and experimental works have been reported in the literature operating nanowire such as unidirectional SPPs propagation along metallic nanowires [80], nanowire SPPs imaging by photon scanning tunneling microscopy [158], subwavelength focusing [159,160], long-range surface plasmon polaritons (LRSPPs) along metallic nanowires [161], selective launch and fan out of SPPs along nanowires [162], nanoparticle (QD) -surface plasmon coupling through nanowires [163, 164], SERS (surface-enhanced raman scattering) applications mediated by nanowire/nanoparticle systems [165–167], directional light emission from nanowires [168, 169], hybrid nanophotonic components [170, 171], plasmonic routers and multiplexers [172], interferometric logic operations [173], cascaded plasmonic logic gates by nanowire networks [174] and ultrashort-pulse propagation along nanowires [175]. Most of above-mentioned works have been addressed to demonstrate passive functionality of SPPs propagation. However, for operating a real plasmonic circuitry [11] to control and process SPPs signals, it is absolutely required for the components to be not only passive elements but also active devices (modulators, switches etc.).

Although many works dealing with active plasmonics have been reported so far [17, 91, 92, 94–96], the properties of the plasmonic waveguides are most often dynamically controlled through the properties of a nearby dielectric materials. In this respect, the contribution of the metal to the modulation of the propagation of a SPP mode deserves a careful examination. We have demonstrated in chapter 2 the thermo-optical modulation of a thin film SPP mode travelling at an air/gold interface at telecom frequencies. Such a configuration achieves a one-dimensional field confinement only in the direction perpendicular to the thin film. At this

stage, it is then worth to evaluate the impact of metal mediated thermo-optical effects for a configuration realizing a tight two-dimensional field confinement in particular in the context of plasmonic interconnect applications. So, in this chapter, we will focus onto photo-thermally induced effects of metallic nanowires. However it is clear that the results we discuss in the following are of interest for SPPs propagation along an electrically addressed nanowire that could be heated by joule effect.

In this chapter, we investigate the photo-thermal modulation of gold nanowires sustaining highly confined plasmonic mode at telecom wavelengths. The nanowires with widths ranging from 150 nm to 400 nm are fabricated by one-step electron-beam lithography. Both optical and telecom characterization of the nanowires are carried out by means of a fiber-to-fiber configuration. First of all, we demonstrate for what we believe for the first time this kind of plasmonic nanowires can be utilized and found to be convenient for a high-bit-rate traffic over short distances at telecom wavelengths. Next, we consider the photo-thermal modulation of the plasmonic nanowire modes by illuminating nanowires with an electro-optically modulated CW visible laser. We show that for a given pumping power, the modulation depth is larger for thinner nanowires. It is also demonstrated that the photo-thermal modulation can be controlled by the incident beam polarization. This effect is attributed to the excitation of localized surface plasmon along the transverse dimension of the nanowire if the incident field contains a component perpendicular to the longitudinal axis of the nanowire. This effect that can be termed as a plasmo-thermally induced heating have been exhaustively investigated in the case of nanoparticules sustaining localized surface plasmon modes [114] but has not been considered in detail propagative plasmon modes.

## 4.2 Design of the nanowire waveguides

The structures we target are schematically shown in the figure 4.1. They are comprised of a grating coupler and a nanowire connected to a taper which all fabricated from the evaporated gold lying on a glass substrate. The opto-geometrical parameters of the nanowires and the grating couplers have been chosen on the basis of numerical calculations explained in next paragraphs.

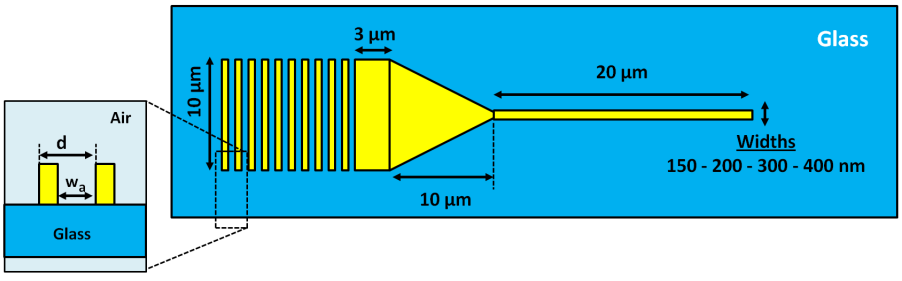


Figure 4.1: Sketched design of top view and cross-sectional view of a gold nanowire lying on a glass substrate

### 4.2.1 Modal analysis of gold nanowires deposited onto a glass substrate

Prior to the fabrication of gold nanowires, it is needed to perform modal analysis of the SPP modes sustained by those waveguides. To this aim, we are going to use COMSOL Multiphysics commercial software package which is numerical simulation software based on finite element method (FEM) for solving partial equations of the electromagnetic waves.

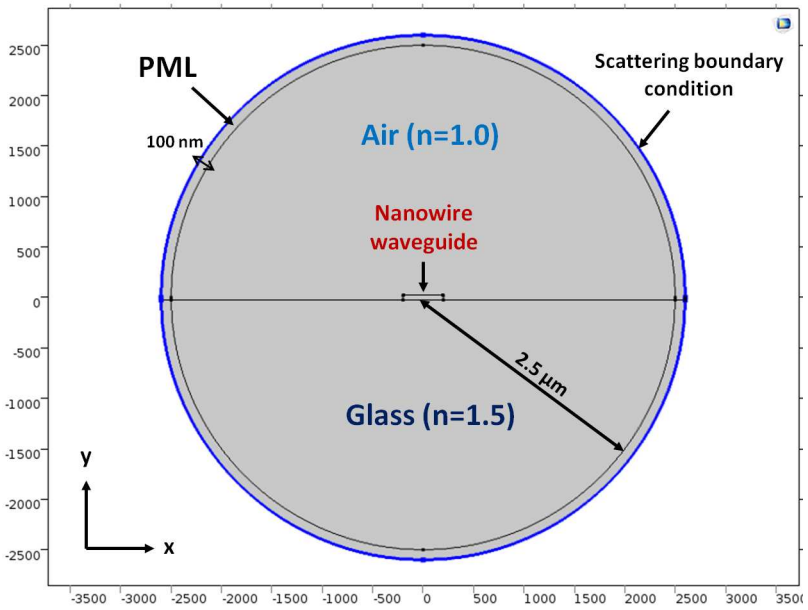


Figure 4.2: Design of the modeling domain for the investigation of modal analysis at $\lambda = 1.55\,\mu m$ telecom wavelength

Our design to be solved is represented in figure 4.2 where we investigate modal analysis in 2D (x-y plane) in which electromagnetic waves propagates in z direction. First, we describe our modeling domain composed of a closed circle with a radius of 2.5 $\mu$m as seen. And our gold plasmonic nanowire is placed at the center of the modeling domain on top of the glass substrate. Air is considered as superstrate with the refractive index of 1. Glass (BK7) is chosen as substrate with a refractive index of 1.5. The refractive index of gold at 1.55 $\mu$m telecom wavelength is selected from the dataset of Johnson and Christy such that $n = 0.52 + 10.74i$ [129]. The thickness of the nanowire is chosen to be 50 nm. The upper two edges of the nanowire waveguide are rounded with a radius of 5 nm to mimic a more realistic situation. The width of the nanowire is considered as a variable in the numerical calculation ranging from 50 nm to 400 nm.

Furthermore, we want to model our domain with open boundaries meaning that waves should pass through domain boundary without reflection. In other words, our boundary conditions of the modeling domain along the outside should be transparent to any incident radiation. So we surround around the outer border of the domain with a perfectly matched layer (PML) with a width of 100 nm (like a ring around the modeling domain). PML is in fact a domain having the same refractive index with the adjacent medium which should absorb all outgoing waves. Moreover, in order to ensure perfect absorption at the boundaries we apply a scatter-

ing boundary condition at the outer contour of the PML which is an another open boundary option proposed by COMSOL Multiphysics for truncated domains. This condition provides non-reflection for the radiations incoming normally to the boundary.

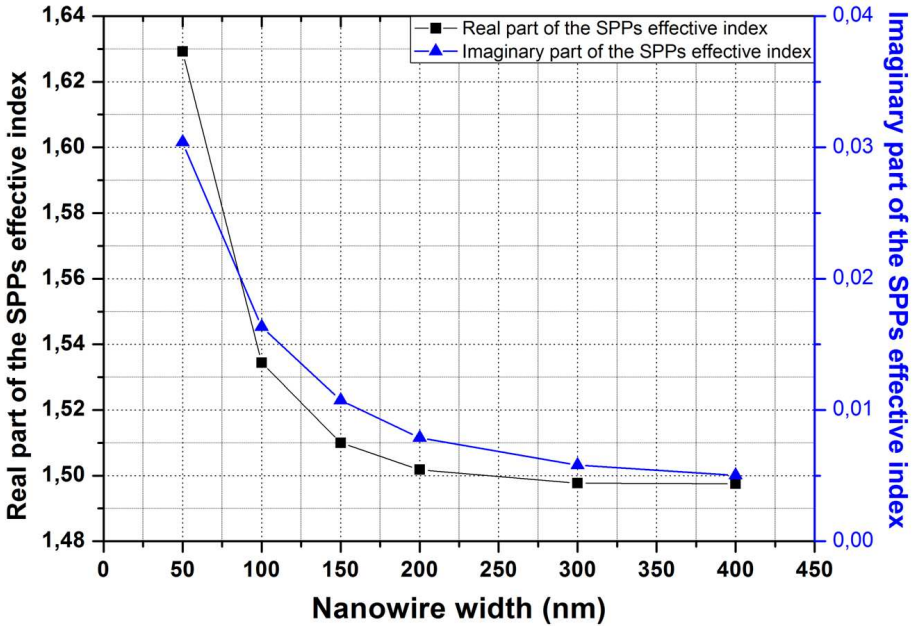


Figure 4.3: Numerically calculated effective mode index of the SPPs propagation versus the nanowire width ranging from 50 nm to 400 nm at $\lambda = 1.55\ \mu m$ telecom wavelength

The calculated modal field distributions of the SPPs propagation modes supported by nanowires of different widths are displayed in the figure 4.4 for a frequency corresponding to a free-space wavelength of 1.55 $\mu$m. For intermediate nanowire widths (400nm) we note that the mode of interest features a field confinement at the edges of the strip (see fig.4.4). The field becomes maximum at the corners in contact with the substrate leading to an effective index of the mode close to that of the glass substrate (see fig.4.3). We note however that the effective index of the SPP mode is lower than the refractive index of the substrate making the SPP mode leaky. This situation has already been recognized and reported in the work of Verhagen et *al.* [82]. In spite of its leaky nature, the propagation length of the SPP mode is still in the range of 25 $\mu$m (see fig.4.5). Note that, because of its leaky nature, the damping distance of the SPP mode depends upon two loss channels, ohmic losses on one hand and radiation leakages on the other hand. As the width of the nanowire decreases, the effective index on the SPP mode increases above the glass light line making the SPP mode bounded to the nanowire which is sometimes called bounded SPP mode. In this situation, the damping distance is only related to the ohmic losses. For a nanowire width of 50 nm, we find that the damping distance is reduced down to about 4 $\mu$m. This result can be understood from a higher field confinement of the SPP mode within the metal for narrow nanowires. Actually, for a narrow nanowire, one can speculate that the SPP mode is built-up from the hybridization of the edges modes. For highly sub-wavelength nanowire, this hybridization leads to a quasi-radial polarization of the SPP mode.

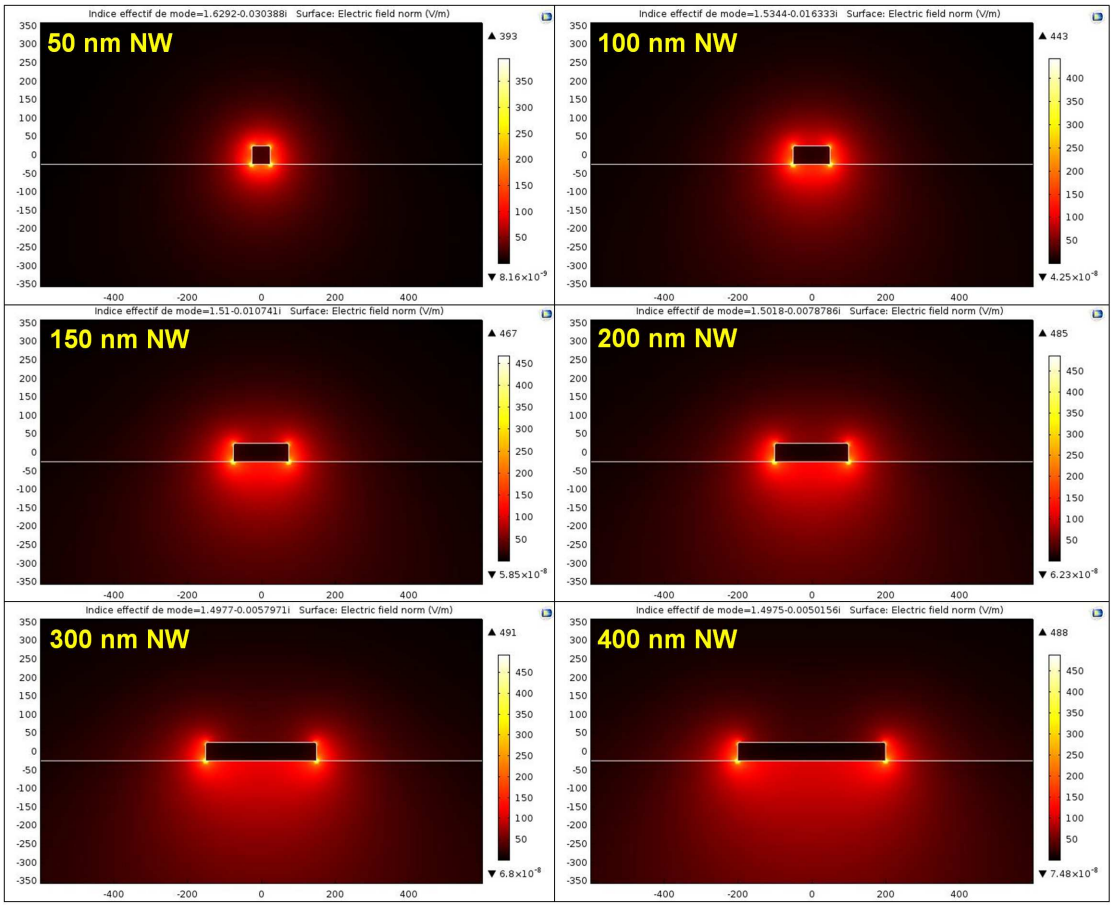


Figure 4.4: Numerically calculated modal field distribution of SPPs propagation modes supported by gold nanowires with a thickness of 50 nm whose width ranging from 50 nm to 400 nm at $\lambda = 1.55\ \mu m$ telecom wavelength

As previously noted, for narrow nanowires, the field still exhibits a maximum confinement at the metal/substrate interface (see fig.4.4). An efficient excitation of the nanowire can thus only be achieved by using an incident mode with a field featuring a field confinement at the same interface. For a wide metal strip, the SPP mode having a field amplitude maximum at the metal/substrate interface is the so-called short-range SPP (SR-SPP) mode reminiscent of the SR-SPP mode of an infinitely extended thin film. In this short range SPP mode or in other words antisymmetric mode most of the electric field distribution localized into the high-index side part of the medium, i.e. glass side [48]. The reason of our interest in this mode because of its outstanding feature allowing us nanofocusing of SPP field without cut-off width which has also been emphasized previously [176].

An efficient excitation of the nanowire mode can be achieved in principle by coupling with a SR-SPP mode sustained by a wide metal strip provided that first an efficient excitation of the SR-SPP mode is performed and second that an adiabatic transition from the metal strip to the nanowire is implemented. An efficient excitation of the SR-SPP mode of a wide metal strip is thus needed for the experimental characterization of the nanowires. As detailed in the

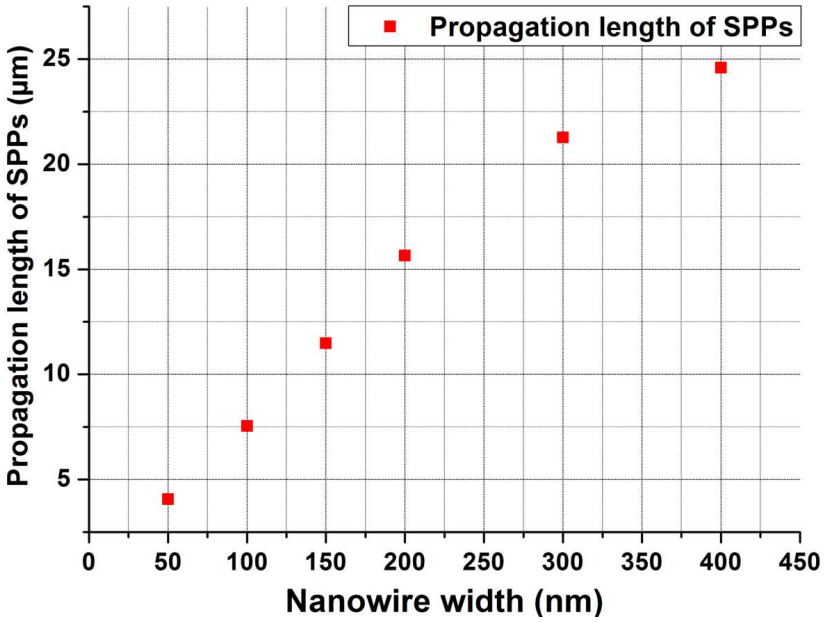


Figure 4.5: Numerically calculated SPPs propagation length along gold nanowires with a thickness of 50 nm whose width ranging from 50 nm to 400 nm at $\lambda = 1.55\ \mu m$ telecom wavelength

next paragraph, we operate grating couplers for the excitation of the SR-SPP mode. For the fabrication reasons, we limit the widths of the nanowire waveguide in the range of 150 to 400 nm for sustaining efficient short-range plasmonic mode.

### 4.2.2 Design of the gratings couplers

Because of the field symmetry of the plasmon modes sustained by the nanowires, the grating couplers are intended for the excitation of the short-range SPP mode sustained by the thin film taper and peaked at the glass/gold interface. The design of the gratings leads to the choice of the period and the filling factor of the gratings couplers. As described in the following, the excitation of the gratings will be done by using a tilted fiber-focuser at an average angle of 30° (see fig.4.18(a)). Thus we focus onto such tilted illumination for the design of the grating couplers. Unlike previous works [82] we consider simple one-dimensional gratings due to the fabrication reasons.

So, the period ($d$) of grating couplers are designed according to the well known grating coupler principle [34] in order to excite bound SPP mode (at gold/glass interface) such that:

$$k_{spp} = k_{||}^{inc} + mG \tag{4.1}$$

$$n_{eff}^{spp} k_0 = k_0 \sin\theta + m\frac{2\pi}{d} \tag{4.2}$$

where $k_{spp}$ is SPPs wave vector, $k_{||}^{inc}$ is the incident wave-vector component parallel to the average surface of the gratings, m is the order of diffraction harmonics (integer) and G is

the grating momentum vector of couplers which provides an additional momentum to in-plane wave vector in order to excite SPP mode. If we develop the equation 4.1, we can obtain the next equation where $n_{eff}^{spp}$ is the effective mode index of SR-SPP, $k_0$ is the free-space wave vector, $\theta = 30°$ is the angle of the tilted fiber-focuser and d is the period of the grating couplers. For instance, if we search the mode index of SR-SPP around $n_{eff}^{spp}$=1.51, then according to the principle given above the period can be deduced as d=1.534 $\mu$m. Besides, we could numerically obtain relevant values of the period and the filling factor via our homemade differential calculation method. Although the computed values from the simulations give us some tips about the approximate value of the period and the filling factor, nevertheless we extend the range of these values to ensure short range SPP excitation such as we choose for the range of period d=1.5 / 1.53 / 1.54 / 1.55 / 1.56 / 1.60 $\mu$m and for range of wa=700 / 750 / 760 / 770 / 780 / 790 / 800 nm. This extension of the values also allows us to overcome possible discrepancy results in nanofabrication process.

Based on the above considerations the following design is suggested in the figure 4.1. A 10 $\mu$m lateral width grating coupler is implemented in front of a 3 $\mu$m long thin film region. This thin film region is continued by a taper with a full opening angle of 53°. The taper is connected to 20 $\mu$m-long nanowires with different widths (150 nm, 200 nm, 300 nm and 400 nm). In all the following the thickness of the metal film is fixed at 50 nm. The distal end of the nanowire is not equipped with output grating coupler. As explained in the following, such a coupler is not necessary when a confocal detection of the light scattered at the end of the nanowire is performed.

## 4.3 Nanofabrication of gold nanowires

The gold nanowires are fabricated by one-step electron-beam lithography on the BK7 glass substrate. Using a support material (e.g. dielectric material) not only changes wave guided mode along a nanowire by breaking the symmetry of the mode field but also decreases optical confinement of the propagated mode which enable us to achieve highly confined nanowire plasmonic waveguides below the diffraction limit.

The nanofabrication of gold nanowires relies on the same electron beam lithography approach as described in the previous chapter. The main differences in the fabrication process are first using a positive tone resist for e-beam lithography which is known as PMMA resist and secondly a new process step called lift-off.

So we would like to explain fundamental differences in fabrication of nanowires: (see fig.4.6).

✓ After cleaning glass samples with the same protocol as before, this time we are going to deposit a positive resist onto the sample, PMMA resist (from Allresist Co.) composed of poly(meth)acrylates with a 950K molecular masse dissolved in ethyl lactate. A very small quantity, 160 $\mu L$ of PMMA resist is deposited on the glass surface and spin coated with a rotation speed of 4000 rpm for 50 s. Then the coated sample is baked on the hot plate at 170 °C for a duration of 5 minutes.

✓ Before starting electron-beam lithography process, it requires to deposit a thin conductor film on top of the PMMA layer in order to evacuate electrons from the sample surface. So we

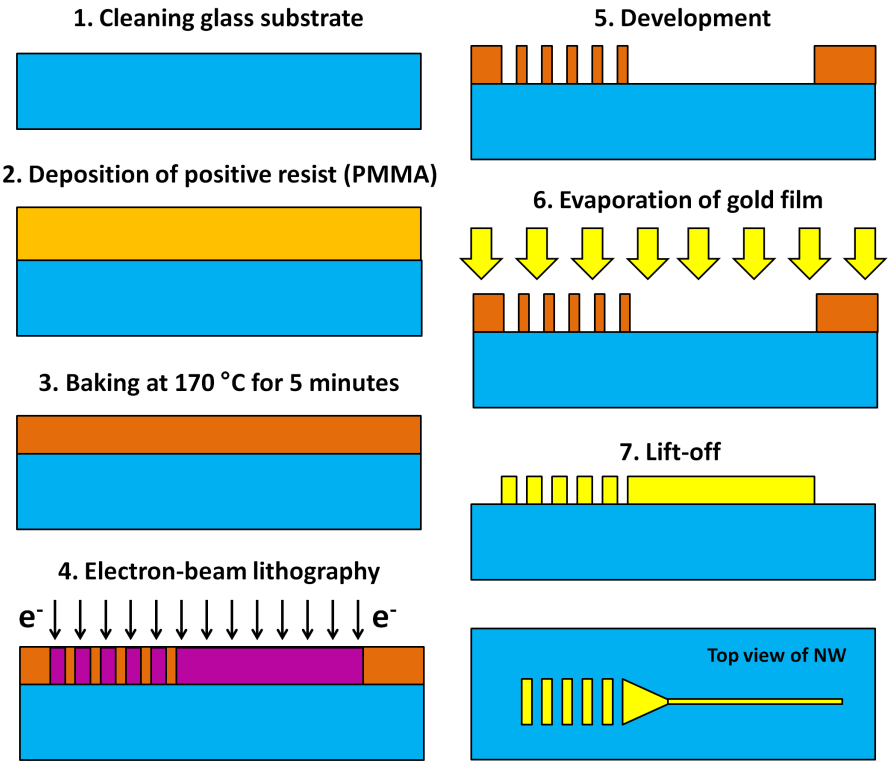


Figure 4.6: Nanofabrication steps for producing gold nanowires on a glass substrate

deposit a thin gold layer (∼15-20 nm) with a sputter coater (Edwards sputter coater S150B). Next, we realize our nanowire design (see fig.4.1) by using the specific lithography software (Elphy Quantum RAITH). Finally we designate e-beam lithography parameters and launch e-beam lithography process.

✓ As soon as the e-beam lithography process is finished, the samples are developed. The development process is also different with the previous one due to using the positive resist, PMMA resist. The samples are developed by immersing in a mixed solution of MIBK : IPA (2 : 5) inside an ultrasonic processor by sonicating of 1-2 second pulses in each 10 seconds for a duration of 50 seconds totally. This sonicating operation is needed and crucial for removing thin gold layer from top of the PMMA coated surface which was previously deposited for evacuating electrons in order to perform e-beam lithography. The development process is ended by immersing the sample inside a beaker filled with IPA (2-Propanol or isopropyl alcohol) and immediately after is gently blown dried with nitrogen.

✓ Before the deposition of gold, we put the samples inside a plasma cleaner with $O_2$ (Harrick Scientific) under vacuum conditions for 1 minutes to ensure complete removal of residual PMMA and other organic particles on the lithographically engraved regions of the resist. Next, a 50 nm-thin gold film is evaporated onto the samples under vacuum conditions ($\sim 10^{-8}$ mbar) at a speed of 0.1 nm/s without using any adhesion layer which is a critical requirement since we are interested in short range SPP mode at the intersection of gold and

glass so the evaporated metal must only be composed of pure gold film.

✓ Lift-off is the last process to be done (neither used nor explained before) for nanowire fabrication aiming at removing irrelevant gold+PMMA parts from the surface. The evaporated samples are placed inside a beaker filled with acetone which is covered by a thin aluminum film to avoid evaporation of acetone and are subsequently left for heating up on a hot plate at 70 °C for $\sim$ 4-5 hours to be able to perform lift-off process.

At the end, the fabricated gold nanowires are observed by an optical microscope to check the nanofabrication quality. For example, SEM images of well fabricated gold nanowires are displayed in the figure 4.7. It should be emphasized that the quality of fabricated gold nanowires is fine although no adhesion layer was used.

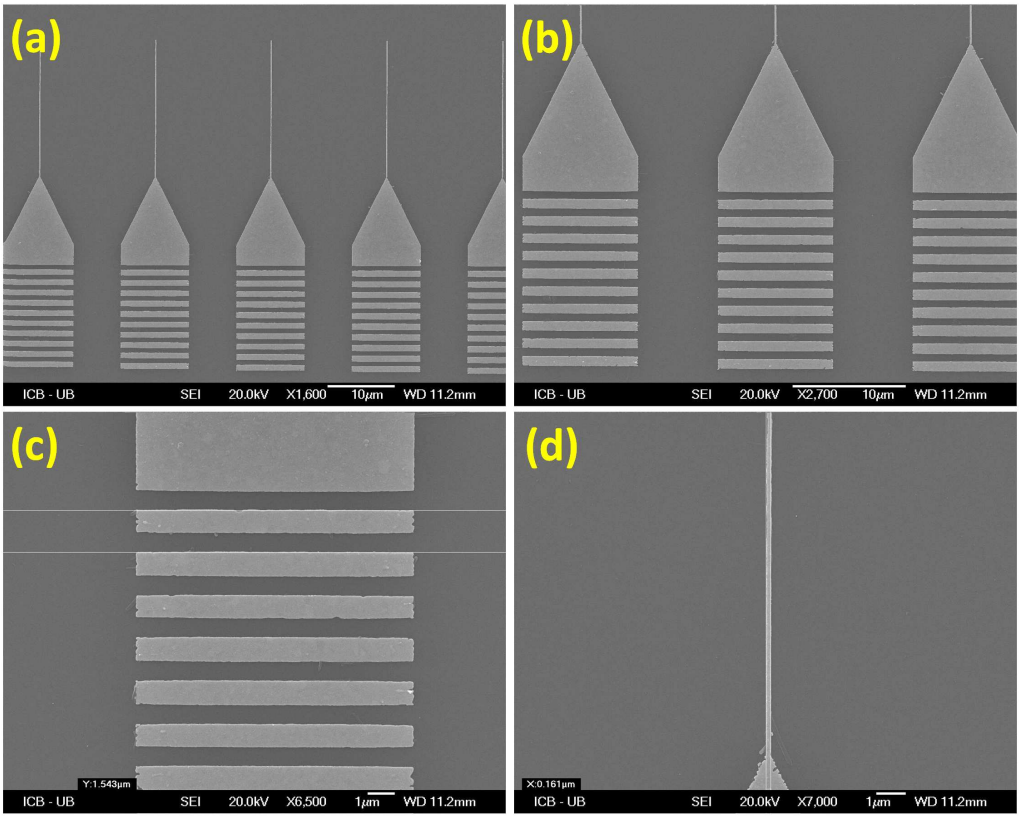


Figure 4.7: (a) Top view SEM image of various $150\,nm$-width gold nanowires on the glass substrate at 1600x magnification (b) Connections of wire parts to taper sections and grating couplers seem well fabricated at 2700x magnification (c) Period of a grating couplers $d$ which is previously designed $1.54\,\mu m$ and measured to be $1.543\,\mu m$ with SEM shows a fair agreement at 6500x magnification (d) Observed wire part of a nanowire shows both good fabrication quality and coherence width measurement of $161\,nm$ with designed value of $150\,nm$ at 7000x magnification

## 4.4 Optical characterization of gold nanowires at telecom wavelengths

In this section, we report on the results of two different kinds of optical characterizations of the lithographically fabricated gold nanowires. First we will consider the transmission of a high-bit rate (10 Gbit/s NRZ (Non return to zero)) signal along gold nanowires demonstrating for what we believe to be the first time the use of those kind of plasmonic waveguides for short-range data transfer. In particular, we will investigate the quality of the transmitted signal after propagation along the nanowires by means of eye-diagrams and BER (Bit Error Rate) measurements. The second part of this section will be devoted to the demonstration of the photo-thermal modulation of a DC (or low frequency) signal travelling along the nanowires at telecom wavelengths.

### 4.4.1 High-bit rate transmission along gold nanowires

#### 4.4.1.1 Basics of optical data transmission systems

In the following paragraphs, we are going to describe basic key components used in classical optical communication systems. Presentation of this part is essential to understand the following section regarding with high-bit rate data transmission along gold nanowires.

An optical communication system is basically considered in three main parts such that a transmitter (TX), a transmission channel and a receiver (RX) as depicted in the figure 4.8 below.

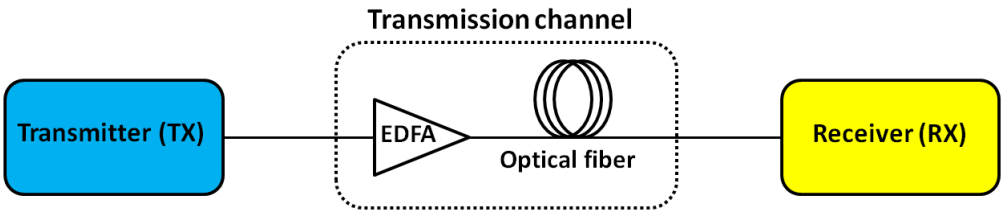


Figure 4.8: Schematic representation of an optical communication system

**a) Transmitter**

A transmitter serves as a generator of appropriate optical signals by converting them from the electrical ones. It is basically composed of a laser source or LED (Light Emitting Diode) and a modulator. The information sending from the transmitter originally consists of electrical bits or symbols such that 0 and 1. Although there are positive and negative voltage levels for electrical communication systems, no negative light exits in an optical communication system but instead of it only light intensity and no light intensity formats are present. So, the signal transmission can be performed through optical systems by means of these two levels.

Transmission in any optical systems is characterized by the rate which is known as the number of bits sent per second. For instance, 10 Gbits/s rate in our optical communication system in here signifies that ten milliards bits consisted of 0 or 1 are sent per second from the transmitter.

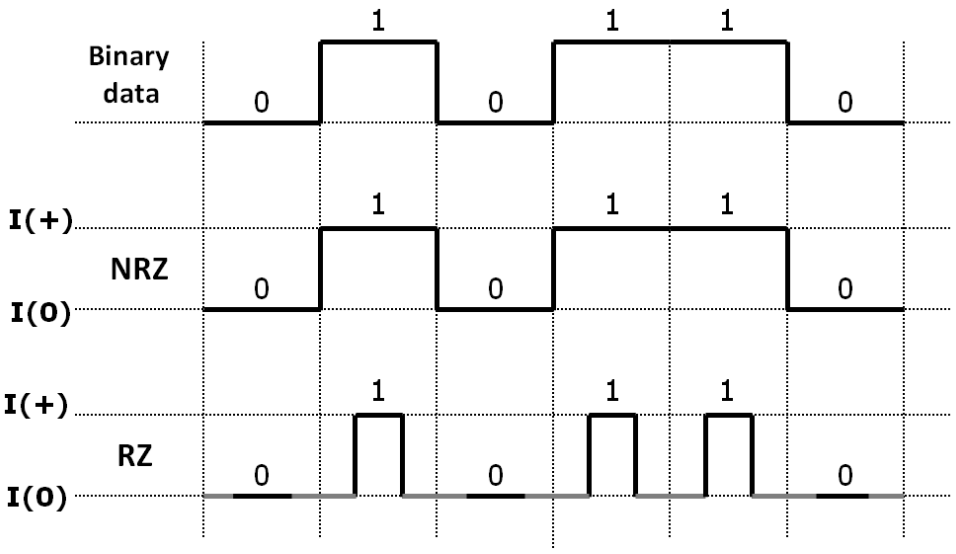


Figure 4.9: Non-return-to-zero (NRZ) and return-to-zero (RZ) coding for a given binary data in optical communication. I(+) and I(0) correspond to presence and absence of light intensity respectively

The generated optical signal coming from the transmitter has to be modulated before sent over the transmission channel. Modulation is defined as the process of changing one or more properties of the carrier signal depending upon the information to be transmitted. There are various coding techniques for modulation or in other words generating an optical bit sequence such as ASK (amplitude-shift keying), FSK (frequency-shift keying) and PSK (phase-shift keying).

ASK, is also known as ON-OFF keying while using within two formats such that NRZ and RZ (see fig.4.9). It is a type of intensity modulation based on the absence or presence of the light corresponding to 0 or 1 binary signal. In FSK, the frequency of a laser light is switched between two frequencies corresponding to 0 or 1 binary signal. And the PSK is also a phase switching of laser light between two different phases corresponding to 0 or 1 binary signal.

We are going to implement NRZ format to the signal in our optical characterization experiments, so it will be useful to give a very brief summary about ASK modulation types.

**Non-return-to-zero (NRZ)**

A non-return-to-zero (NRZ) is the most widely used coding format in optical communication systems. It is a binary code where 1s correspond to one significant condition, e.g., pulse of light and 0s correspond to other significant condition, e.g., no light. There is no rest condition or other neutral condition level while transition occurring between two consecutive conditions (see fig.4.9 and 4.10(a)).

**Return-to-zero (RZ)**

A return-to-zero (RZ) coding format is commonly used for solitons in optical communications. It is again a binary code where the signal returns zero level between each consecutive condition (see fig.4.9 and 4.10(b)). The "zero" is accepted to be a rest condition or neutral condition

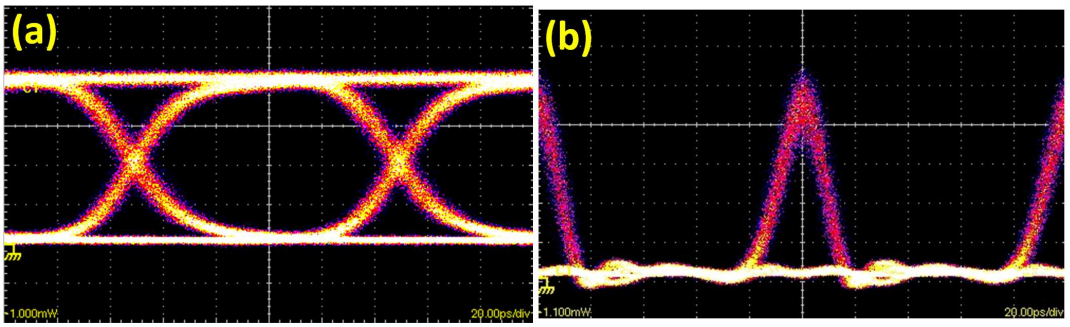


Figure 4.10: Eye diagrams of an optical signal (a) Non-return-to-zero (NRZ) (b) Return-to-zero (RZ) coding formats have been used (Image adapted from ref. [177])

between transitions (see grey lines on the part of the RZ coding depicted in the figure 4.9). When it is used for solitons, bit 1 represents presence of a pulse and bit 0 represents absence of a pulse.

**b) Transmission channel**

Optical fiber is known as the fundamental transmission medium for transporting optical signals from source to destination. Before travelling along optical fiber, the signal is amplified by an optical amplifier, such as EDFA (Erbium doped fiber amplifier) and then start to propagate through the transmission channel (see fig.4.8). It should be noted that while optical signal is travelling, it is subjected to loss of strength and dispersion. Therefore, this amplification is a required process for boosting its strength.
Optical fibers will be replaced by plasmonic nanowire waveguides in our experiments.

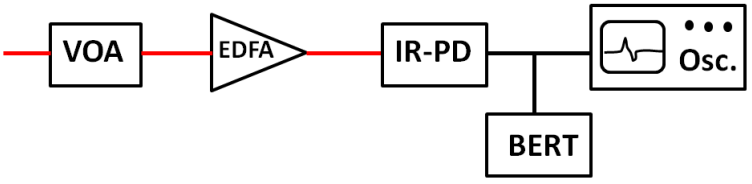


Figure 4.11: Schematic representation of our receiver part consecutively composed of variable optical attenuator (VAO), Erbium doped fiber amplifier (EDFA), infrared photodiode (IR-PD), bit error rate tester (BERT) and optical sampling oscilloscope (OSO) for imaging eye diagrams

**c) Receiver**

Receiver part is responsible for the conversion of transmitted optical signals to electrical ones and further processing them precisely in order to recover appropriate received signals. Receiver can compose of various types of components such as optical amplifier, photodiode, bit error rate tester (BERT) and optical sampling oscilloscope (OSO) as shown in the figure 4.11.

Optical amplifier functions for boosting optical signal strength and generally an optical filter is tailed after it to reduce amplified spontaneous emission noise. Photodiode or photodetector is used to convert optical signals into electrical ones. BERT is employed for the

assessment of transmitted signal accuracy in the optical communication system by measuring bit errors per unit time. Optical sampling oscilloscope (OSO) is operated for evaluating optical transmission quality in ultra high speed by different types of analysis such as pulse waveform, eye diagrams and SNR (Q factor) measurement.
In forthcoming experiments, we will conduct our investigations by involving in *eye diagrams* and *BER measurements*. So, it can be helpful to give brief explanations about these concepts.

**Eye diagrams (patterns)**

In a high-bit rate optical transmission (Gbit/s), ultra fast change of the signal state and accurate display desire of the received signal instantly do not allow us to measure and visualize it easily with conventional techniques. The eye diagrams propose an efficient solution by displaying each instants of the signal one top of the another one in a superimposed way. So that, you can assess the quality of the transmission by means of only observation the aggregate of all instances of the signal in a concise image.

An eye diagram is basically a demonstration format of the received data by a type of oscilloscope image where all transmitted symbols are continuously sampled and displayed on the vertical axis while the rate of the data is shown on the horizontal axis in the image (see fig.4.10(a)). This special image is generated by use of a photodiode and OSO (optical sampling oscilloscope) in the optical communication. Due to looking like to a pair of eyes, it is named as "eye diagram" or "eye pattern".

It is a very instructive experimental tool whereby we can evaluate the performance of a transmission system only by observing an eye diagram. For instance, an open eye diagram indicates a good quality transmission whereas a closed one shows the distortion of the signal due to various effects such as channel noise, intersymbol interference (ISI) and etc. Furthermore, some features of an eye diagram allow us to perform various measurements on the system for example, eye width permits to measure timing synchronization and jitter effects and so on.

**Bit error rate (BER)**

In digital communication systems, the threshold detection method is used to determine whether the transmitted bit is to be 0 or 1 in the receiver. If noise fluctuations are dominant on the signal level, received bit may be interpreted as 1 (or 0) instead of 0 (or 1) sent from the transmitter. Therefore, a bit error occurs. Bit error rate (BER) is defined as the ratio of bit errors to the total number of transmitted bits. Bit-error-rate analysis is considered as one of the fundamental characterization techniques for evaluating signal quality or measuring goodness of an optical communication system.

BER is indicated by a percentage and has no unit. Increasing of SNR (signal to noise ratio) decreases bit error rate. BER is expressed as a negative power of 10. For instance, in optical communications, the maximum acceptable BER is $10^{-9}$ signifying one error is acceptable in one billion bits sent.

**BER measurement**

The receiver part for measuring BER of the system is schematically depicted in the figure 4.11. It consists of variable optical attenuator (VAO), Erbium doped fiber amplifier (EDFA),

infrared photodiode (IR-PD), bit error rate tester (BERT) and optical sampling oscilloscope (OSO) with a bandwidth of 50 GHz for imaging eye diagram.

By increasing attenuation via VOA, the BER and received optical powers are measured for signal transmission through first the transmission medium such as optical fiber (in our case plasmonic waveguides) and then secondly **back-to-back (BtB)** transmission that means connecting the transmitter directly to the receiver without a transmission medium. So that we can distinguish two principal BER mechanisms, attenuation and dispersion, within the channel and then we can readily extract power penalty. At the end, we can demonstrate these obtained data in a graphical form as given in the figure 4.12 where two curves representing the BER of back-to-back (BtB) and fiber transmissions in terms of received optical power.

In most long distance telecom systems, a BER of $10^{-12}$ is accepted to be a requirement, so we use this value in order to calculate power penalty. At the same bit error rate, namely log(BER)=-12, the received optical power difference between two curves indicates the power penalty which is essentially required additional signal power in order to achieve a BER of $10^{-12}$ in these conditions. In general, the power penalty is desired to be as low as possible in optical communication systems.

#### 4.4.1.2 Gold nanowires as high-bit rate data transmitters

Telecom wavelengths in optical communication is accepted as essential frequency ranges with lowest losses where the minimum loss is 0.2 dB/km occurring through an optical fiber at 1.55 $\mu$m wavelength. Although the investigations in plasmonics is generally concentrated on visible wavelengths, recently telecom wavelengths has also attracted more interest especially demonstration of plasmonics in true datacom and telecom traffic applications [12–15]. So,

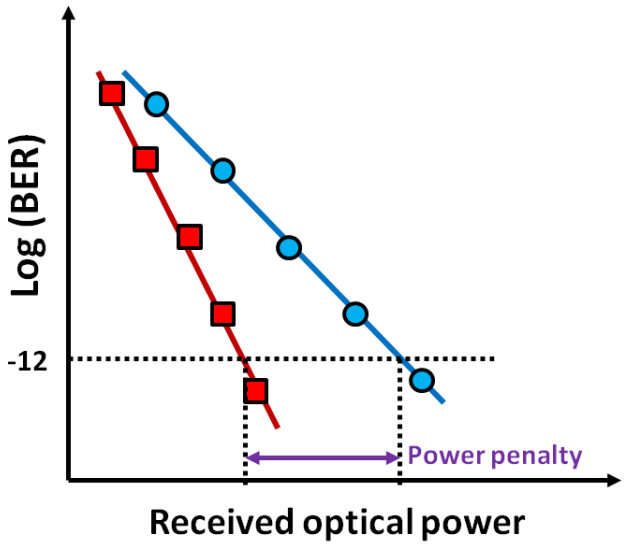


Figure 4.12: A conventional graph of logarithmic bit error rate (BER) versus received optical power with extraction of power penalty at the same bit error rate $log(BER = 10^{-12}) = -12$. Red-line with small squares corresponds to back-to-back (BtB) transmission and blue-line with small circles corresponds to fiber transmission (or any transmission medium)

in this section, we demonstrate telecommunication characterization of lithographically fabricated gold nanowires what is believed to be the first investigation on plasmonic nanowires as high-bit rate data transmitters according to our best knowledge.

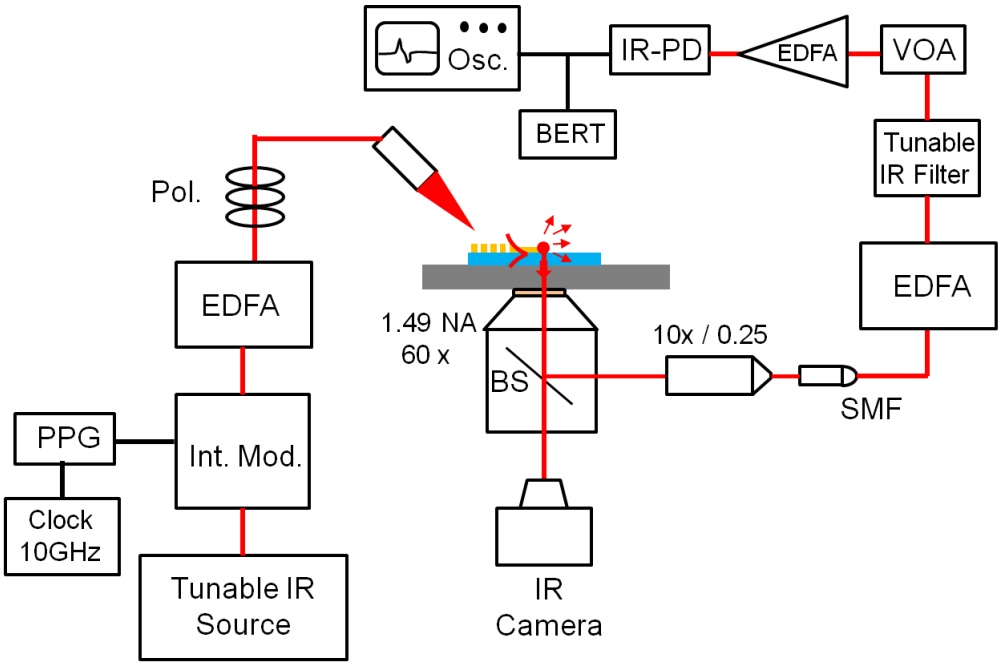


Figure 4.13: Fiber-to-Fiber homemade confocal detection set-up for measuring of 10 GHz NRZ signal transmission along lithographically fabricated gold nanowires at telecom wavelengths

The optical characterization of the high-bit rate signal traffic along lithographically fabricated gold nanowires are carried out by means of a fiber-to-fiber homemade confocal experimental set-up (see fig.4.13). The key features of this setup is first having a high excitation/detection sensitivity in free-space measurements, implying that, for instance more sensitive than a CCD camera and second allowing us to perform time-resolved high-bit rate investigation along nanowires by 10 Gbit/s signal transmission analysis. So that, we can also demonstrate the efficiency of this fiber-to-fiber set-up for the optical characterization of the nanowire waveguides by performing a 10 Gbit/s NRZ (Non return to zero) signal transmission experiment at telecom wavelengths. For this high bit rate experiment, we will use the Picasso platform which is a study platform for ultra-fast optical communications with a bandwidth of 500 GHz in optics and 50 GHz in electronics, a data rate ranging from 10 to 40 Gbit/s and 8 canals. [1]

First of all, we would like to present our telecom characterization set-up that consists of an important innovation based on a specific detection scheme of nanowires SPPs (see fig.4.18) different from the previous detection setup (see fig.2.5). In the experimental set-up, an optical 10 GHz NRZ pseudo-random binary sequence (PRBS) is generated by means of a pulse pattern generator (PPG) associated to an intensity modulator acting on a continuous-wave near-IR

[1]This technical support has been provided from the council of the Burgundy region in Dijon

laser source tunable from 1500 nm to 1610 nm. A TM-polarized non-return to zero signal (NRZ) is focused on input gratings of a nanowire through 30 degree tilted lensed fiber focuser with respect to the optical axis of the microscope.

The input gratings provide efficient excitation of highly confined SPP mode (will be considered in detail afterwards) on the nanowire. When the propagated SPPs signal arrives at the distal end (or endface) of the nanowire, naturally it scatters and then converted into the light. So it can be detected by an inverted high numerical aperture (NA=1.49) microscope equipped with an immersion oil objective. The detected signal can be both monitored by an IR camera and injected into a single-mode fiber (SMF) by means of low numerical aperture objective (10X / NA=0.25). This signal is then amplified and filtered optically to choose relevant part of telecom wavelengths ($\lambda = 1.56\ \mu m$ in our case). After that, by passing through our receiver part comprising of variable optical attenuator (VOA), erbium doped fiber amplifier (EDFA) and for converting optical signals to electrical one via IR photodiode with a bandwidth of 70 GHz, the corresponding detected signal can be either visualized by optical sampling oscilloscope (OSO) with a bandwidth of 50 GHz allows us to display "EYE diagram" or connected to BERT (bit error rate tester) in order to measure BER.

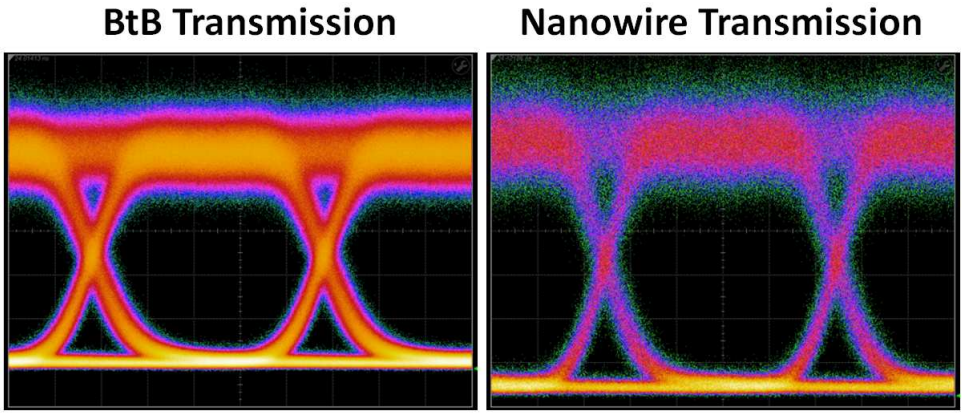


Figure 4.14: Eye-diagrams of the back-to-back (BtB) and nanowire transmission of 10 Gbits/s signal for a received average power of -29 dBm at the wavelength of 1.56 $\mu$m

Described steps up to now are the demonstration of high-bit rate transmission along lithographically fabricated gold nanowires. In order to investigate the back-to-back transmission (BtB) on the system, a non-return to zero optical signal (NRZ) is directly connected from the exit of polarizer to VOA (without passing through the nanowire) and then the measurement operation is performed again. In the end, the obtained results are compared and interpreted both qualitatively and quantitatively in the following paragraphs.

**Experimental results and discussions**

At first, we observe the displayed eye-diagrams in the case of back-to-back (BtB) and nanowire transmission in order to evaluate the impact of the nanowire transmission on the quality of a 10 GHz NRZ signal. The measured eye-diagrams for the two types of transmissions are demonstrated in the figure 4.14. In both cases, the eye-diagrams were recorded for an incident wavelength of 1.56 $\mu$m and an average received power of -29 dBm. For both BtB and nanowire

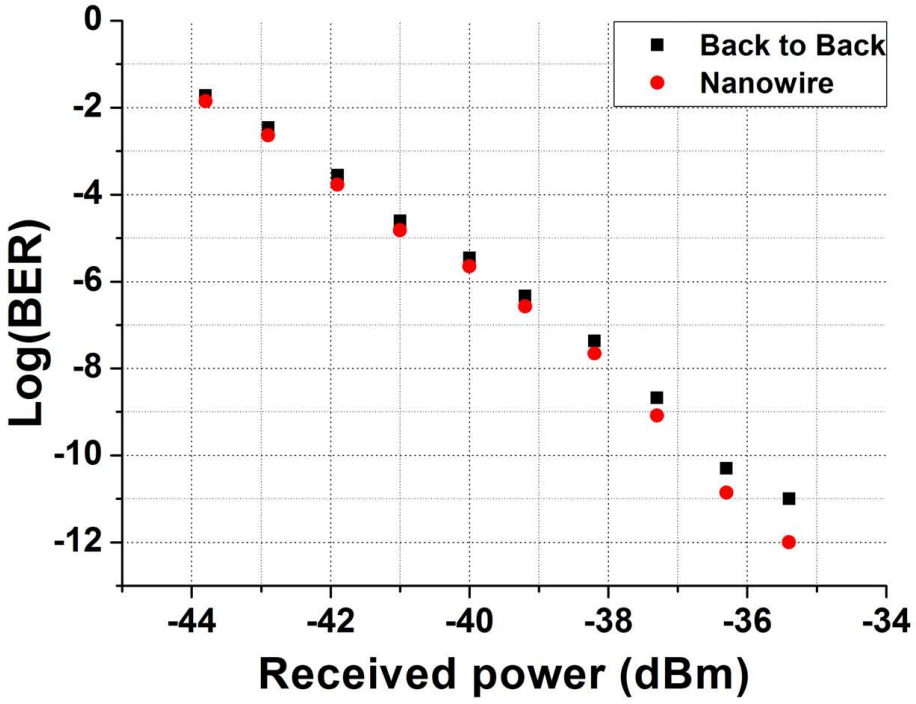


Figure 4.15: Comparison of the bit error rate (BER) for the back-to-back (BtB) and nanowire transmission as a function of the received power at $\lambda = 1.56\ \mu m$

transmission case, we adjusted received power by changing the VOA attenuation level while keeping constant the amplifier gains. As a result, it is observed that the transmission along the nanowire does not change the opening of the eye-diagram and the amplitude of the time jitter does not alter significantly which all proves that a lithographically fabricated gold nanowire can be safely used for high-bit rate traffic over short distances.

This qualitative result is further confirmed by the bit error rate (BER) measurements of 10 GHz NRZ signal as a function of the received powers for the nanowire and back-to-back (BtB) transmissions at 1.56 $\mu$m wavelength. No power penalty observed in these results which are displayed in the figure 4.15. It is clearly seen that at this wavelength an error-free traffic at 10 GHz along the nanowire is achievable for received power larger than -36 dBm. It should be also noted that the loss of our nanowire is found to be 41 dB at $\lambda$=1.56 $\mu$m according to these measurements.

As a conclusion, the negligible BER power penalty for 10 GHz NRZ signal transmission demonstrates that this kind of nanowires is convenient and can be safely used for a high-bit-rate traffic over short distances at telecom wavelength.

### 4.4.2 Photo-thermal modulation of SPPs propagation along nanowires

In this part, we focus on optical characterization of thermo-optical properties of lithographically fabricated gold nanowires. More specifically, we investigate the photo-thermal modulation of highly confined SPPs propagation mode along the nanowires at $\lambda$=1.55 $\mu$m telecom

wavelength. Photo-thermal excitation of lithographically fabricated gold nanowires is performed by means of a normally incident visible pump laser on a nanowire which leads to the photo-thermal modulation of SPPs propagation mode. While launched SPP mode is propagating along the nanowire at telecom wavelengths, the photo-thermal excitation is generated by illuminating on the wire center of the nanowire by means of a visible laser at the wavelength of 532 nm. As a matter of fact, the physical mechanism of this excitation is based on the nonlinear thermo-optical effects which arising from light-induced modulations of the refractive index of the gold due to the temperature changes and in turns modifies the field distribution of the nanowire plasmon mode travelling along the gold/glass interface.

| Thermo-optical coefficients | $\partial_T n$ [ $K^{-1}$ ] |
|---|---|
| Gold | $0.72 \times 10^{-3}$ |
| PMMA | $-0.105 \times 10^{-3}$ |
| Cycloaliphatic acrylate polymer (cyclomer) | $-0.3 \times 10^{-3}$ |

Figure 4.16: Comparison of thermo-optical coefficients (TOCs) of gold [140] with two different polymers' ones, PMMA [95] and cyclomer [66], at telecom wavelength which are being frequently used in plasmonic applications currently

It is well known that thermo-optical properties of metals are described by their thermo-optical coefficients (TOCs) which have previously been explained in the second chapter. And subsequently, we demonstrated that TOCs of gold at telecom wavelength are prominent and cannot be neglected [140]. Indeed, we can perceive this situation more clearly while comparing TOCS of gold with the ones of different types of polymers which are extensively used in plasmonic devices currently (see fig.4.16). Although it is not very convenient directly perform this comparison due to the extinction coefficient contribution of gold, nevertheless, we can qualitatively say that TOCs of gold are remarkable compared to frequently used polymers. As it can be seen, the absolute magnitude of the TOCs of gold is nearly seven times larger than PMMA's one [95] and two and a half times larger than cyclomer's one [66] which confirms the importance of this investigation especially for plasmonic applications.

Before anything else, we want to describe the experimental set-up (see figure 4.17) used for the measurement of the photo-thermal modulation of SPPs propagation mode along nanowires which contains some modifications with respect to the previous one (see figure 4.13). Near-IR signal provided from a tunable CW laser source (range between 1500-1610 nm) is polarized by a manual fiber paddle polarization controller and subsequently focused on the input gratings of a nanowire through 30 degree tilted lensed fiber focuser (also see figure 4.18). A low numerical aperture long working distance objective (EPI L Plan Apo 5X / 0.16) is placed above the

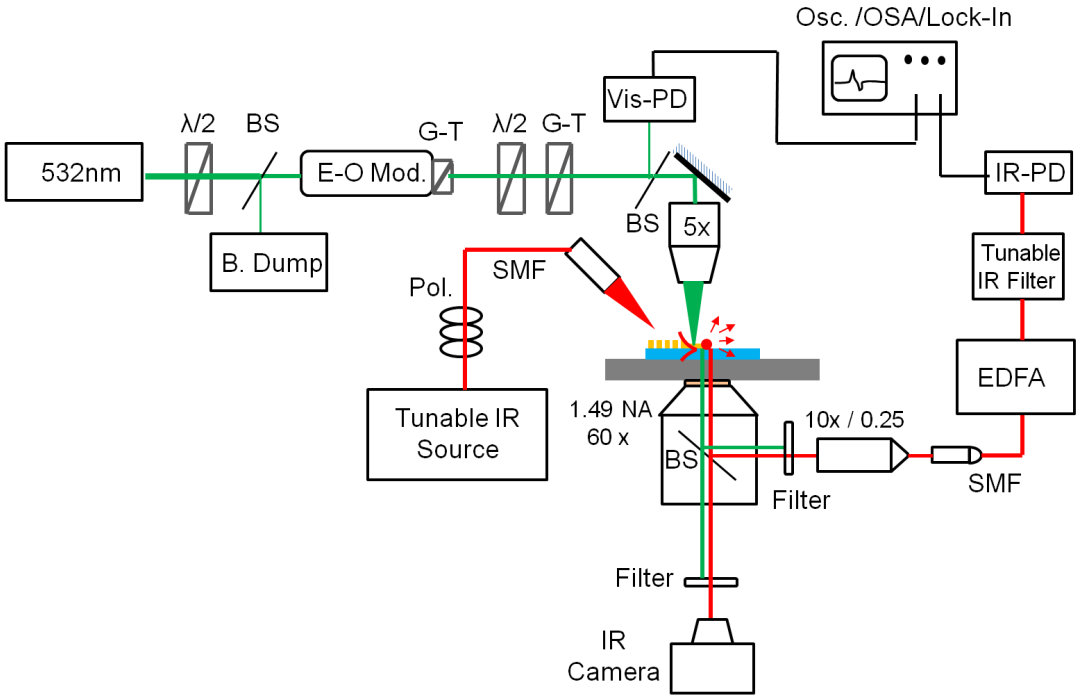


Figure 4.17: Schematic view of fiber-to-fiber homemade confocal experimental detection setup for measurement of the SPPs photo-thermal modulation along nanowires at telecom wavelengths

microscope stage to focus the visible pump beam. And the photo-thermal excitation is generated by a continuous-wave visible laser at the wavelength of $\lambda$=532 nm which is modulated by a highly efficient, 20 ns rise/fall-time, electro-optical modulator (EOM).

The detection scheme is identical to that of previous one (see figure 4.13) except that variable optical attenuator (VOA) and erbium doped fiber amplifier (EDFA) have been removed from the setup. While the visible pump beam is filtered at the exit of the microscope (see figure 4.18), the photo-thermally modulated signal detected and injected into a single mode fiber (SMF) through an objective (10X / 0.25). After amplifying the detected optical signal, it is optically filtered to obtain relevant part of the telecom wavelength and then converted to electrical signals by a fast IR photodiode (Rise time 2ns / frequency range 0-250 MHz). These detected electrical signals can be monitored by an oscilloscope with a bandwidth of 40 MHz which is also to be triggered by the signal of the fast visible photodiode (Rise time 2ns / frequency range 0-250 MHz) receiving a tiny fraction of the pump beam.

Leakage radiation microscopy (LRM) allows us to record simultaneously leakage radiation images of the SPP mode traveling along nanowires [128]. Specifically designed grating couplers can excite not only air/gold SPP mode which a is frequently encountered situation in the literature but also more confined gold/glass SPP mode (short range SPP mode) which has been preferred in here. By illuminating input grating couplers with our near-IR source with a polarization parallel to the longitudinal axis of the nanowire at $\lambda = 1.55\ \mu m$, we can excite bound SPP mode at gold/glass interface as shown in the figure 4.19. Increasing the integration times of recorded leakage images by our InGaAs-IR camera confirms our bound mode in which no leakages are seen along the wire part of the nanowire whereas a high intensity

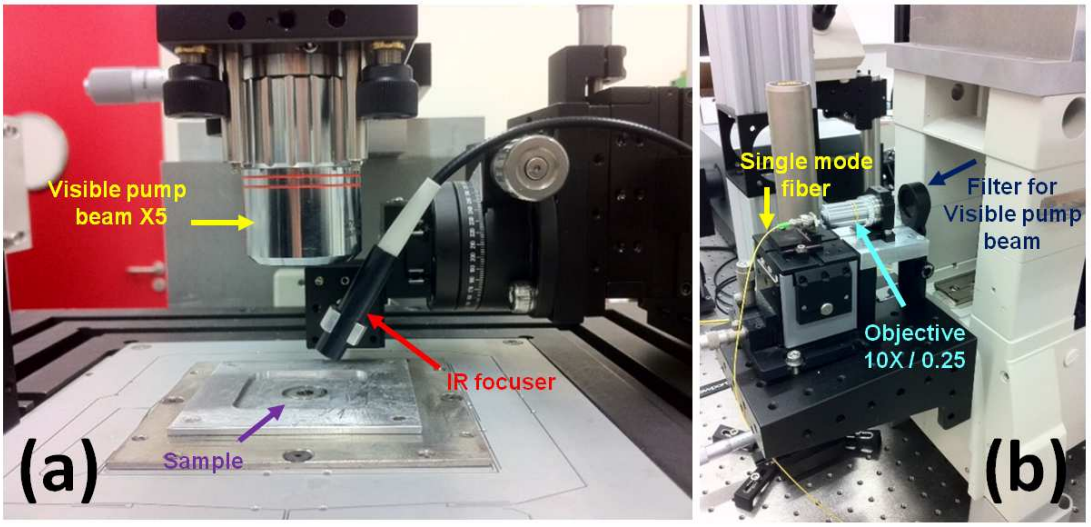


Figure 4.18: (a) Excitation part: It is composed of a 5X long working distance objective for focusing of visible laser and 30 degree tilted lensed fiber focuser for focusing of near-IR laser (b) Detection part: while blocking visible laser by a filter, a confocal detection of near IR laser is performed by injection into a single mode fiber (SMF) through an objective (10X / 0.25).

of SPP spot at the distal end of a $150\ nm$-width nanowire is clearly observed. It should be also pointed out that at very high integration times in the images taken by the camera, some small leakages may be observed on the wire part due to the roughness of gold surface originated from imperfections in lithographical fabrication results (see fig.4.7) which causes the conversion of the SPPs into a free space light.

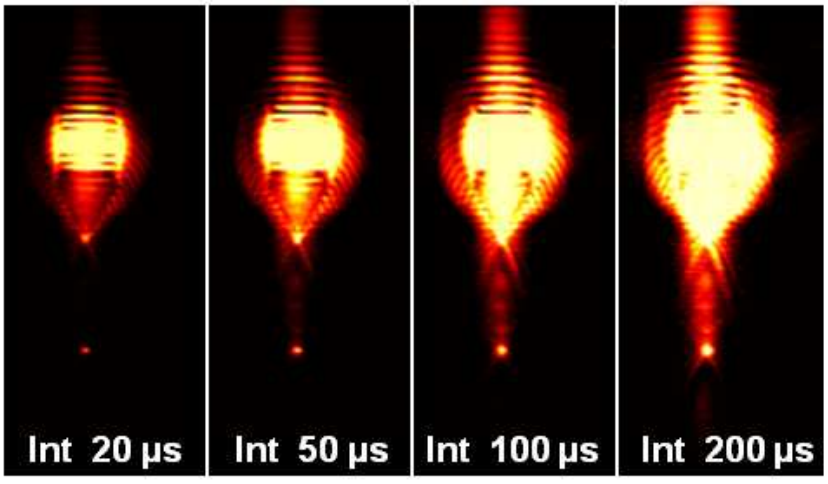


Figure 4.19: Bound SPP mode excitation via grating couplers and propagation along a 150 nm width nanowire with increasing integration times at $\lambda = 1.55\ \mu m$ wavelength imaged by LRM

After exciting this highly confined SPP mode and it propagates along the gold/glass interface, the detection mechanism can be accomplished in the manner described hereafter. Al-

though no output grating couplers are present at the distal end of the nanowire, propagated SPPs waves can be converted to scattered light via the edge of the nanowire that allows us to collect light waves if confocal detection set-up is already established. Besides, while SPPs waves are propagating along the nanowire, photo-thermal excitation is generated by illuminating on the midsection of the nanowire with a normally incident pump laser modulated at a frequency of 1 $kHz$ with a duty-cycle=50% (see fig.4.20(a)). The photo-thermal modulation of SPPs propagation can thus be measured through the edge of the nanowire with the confocal detection setup (see fig.4.18(b)). We demonstrate and discuss these measurements and results in detail in the next section.

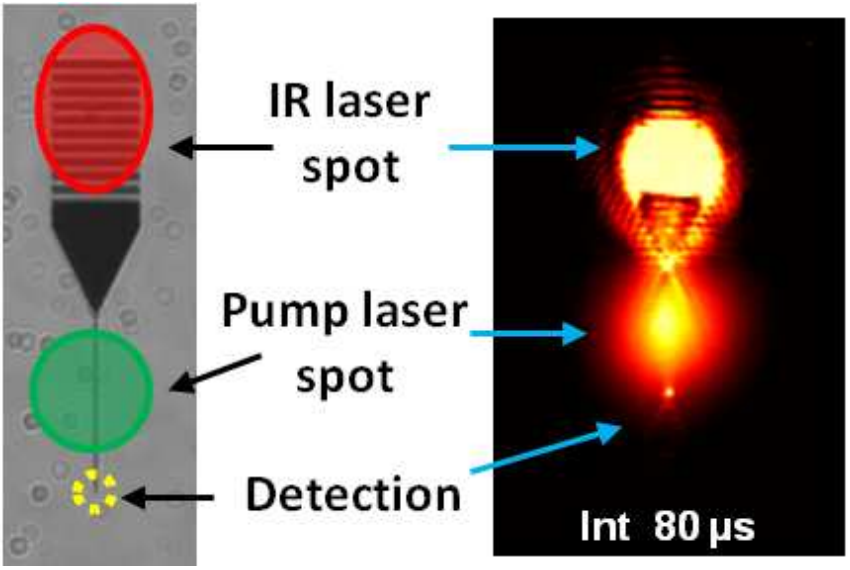


(a) While excited SPP mode propagates along the nanowire, photo-thermal excitation generated by a modulated pump laser illumination on the nanowire center and in turns SPP modulation depth can be detected by the edge

(**Notice:** Left image captured by visible camera, right image captured by IR camera and magnifications are different)

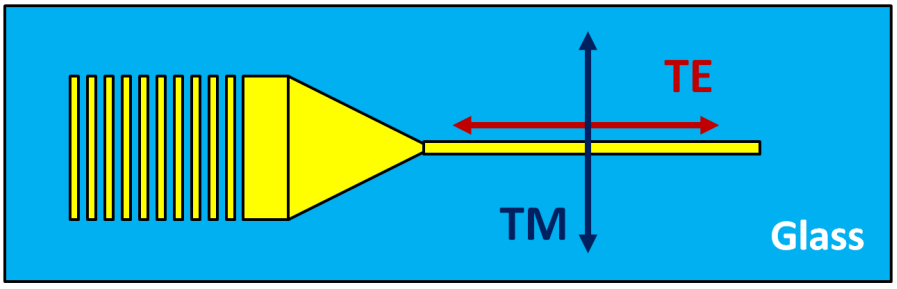


(b) Polarization convention of the incident visible pump beam

Figure 4.20:

#### 4.4.2.1 Experimental results and discussions

We have measured photo-thermal modulation depths of SPPs propagation along lithographically fabricated gold nanowires widths ranging from 150 $nm$ to 400 $nm$. In order to investigate consistency of measured modulation depths, the characterization steps for each width have been carried out with more than one nanowire. In other words, two different individual nanowires for the widths of 150 and 400 $nm$ and three different individual nanowires for the widths of 200 $nm$ and 300 $nm$ have been employed. Furthermore, the measurements have been performed either TM or TE incident polarization of the pump beam (see fig.4.20(b)). Besides, we have realized our experiments for three different pump powers normally incident on nanowires such that 56.8, 85.2 and 113.6 $mW$ in order to determine the effect of incident pump laser on the modulation depth.

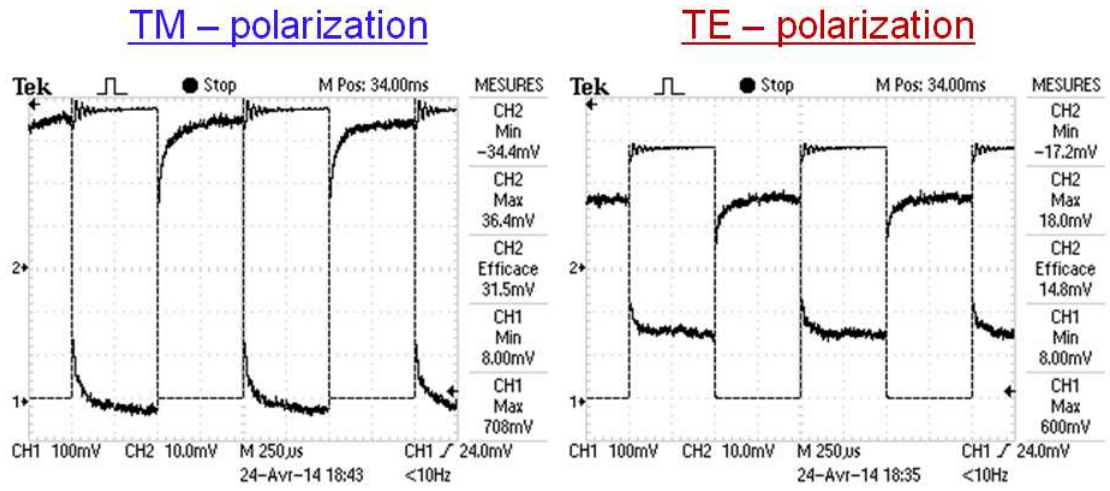


Figure 4.21: **Solid-line:** SPPs signal modulation recorded with the IR photo-diode in the case of a photo-thermal excitation with a cw illumination (113.64 mW) modulated at a frequency of 1 kHz (Duty-cycle=50%) along a 150 $nm$-width nanowire. **Dashed-line:** Control signal of the visible photo-diode showing the modulation of the cw pump beam

Photo-thermal modulation of SPPs signal can be detected by the fast IR photo-diode and then can be recorded by the oscilloscope which is triggered by the signal of the visible photodiode in case of modulated CW laser (see fig.4.17). Figure 4.21 shows the oscilloscope traces of the ac coupled SPPs signal for both TM and TE polarization of incident pump beam detected by the fast IR photo-diode along with the visible photo-diode signal when a photo-thermal CW excitation modulated at a frequency of 1kHz (with a power of 113.6 $mW$ and Duty-cycle=50%) is applied on the midsection of 150 $nm$-width nanowire (see fig.4.20(a)).

Likewise in our previous work (in chapter 2) [140], we define modulation depth as ratio of the SPPs signal modulation $\Delta I$ during the photo-thermal pumping to the SPPs signal $I$ in the cold state in absence of pumping as follows

$$Modulation\ depth\,(\%) = \frac{\Delta I}{I} \times 100 \tag{4.3}$$

Based on the experimental measurements of the detected SPPs signal, we can compute SPPs

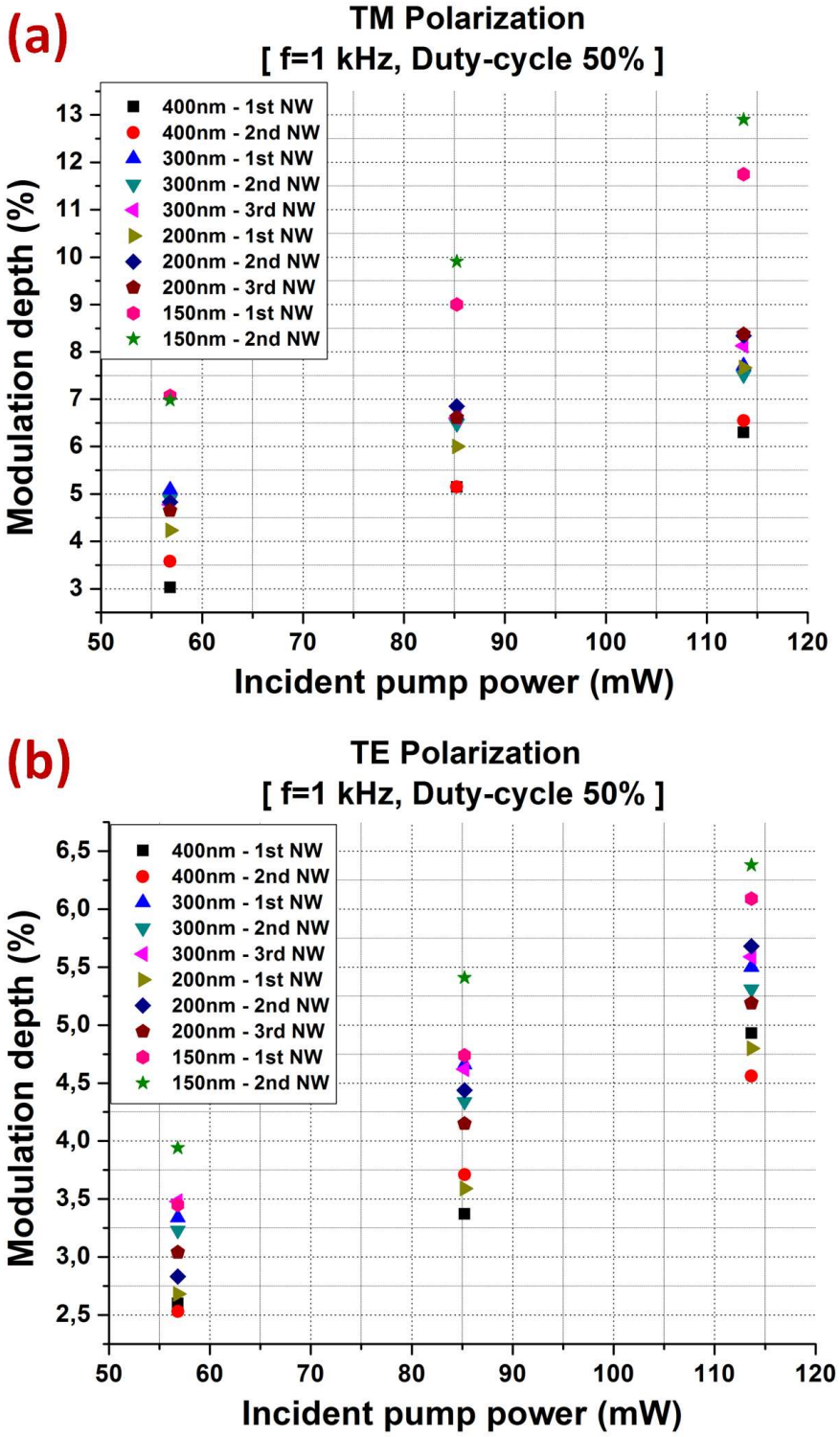


Figure 4.22: (a) (resp. b) Modulation depths (%) have been computed from the measurements of SPPs photo-thermal modulation for three different pump powers 56.8, 85.2, 113.6 mW incident on nanowires ranging from 150 to 400 nm for TM (resp. TE) polarization of the pump beam (f=1 kHz, Duty-cycle=50%)

photo-thermal modulation depths for individual nanowires which have been demonstrated in the figure 4.22 and 4.23.

Regardless of polarization state of incident pump power, it is clearly seen in the figure 4.22 (a)-(b) that the modulation depth increases when the width of nanowires decreases. In other words, modulation depth is found to be smaller for thicker nanowires whereas larger for thinner nanowires whatever the incident pump power. And also, modulation depth increases with rising of incident pump power.

If we consider modulation depths for a fixed pump power (maximum incident power of $113.64\ mW$) as shown in the figure 4.23 (a)-(b), it is apparently observed again that the modulation depth is larger for thinner nanowires at any polarization. This result arises from the larger damping and hence larger field penetration into the metal of the SPP mode sustained by narrow nanowires. Besides, a fair agreement of modulation depths of each consecutive individual nanowires of the same width can be noticed whatever the polarization.

On the other hand, the modulation depth can be controlled by the polarization of the incident pump beam as is seen. Both TM and TE polarization of incident pump beam have a tendency of increasing modulation depth when the width of the nanowires decreases from $400\ nm$ down to $150\ nm$. However, it is striking that the increase of TM polarization in thinner nanowires is much larger than thicker nanowires. We explain this physical situation as the enhancement of the modulation depths due to LSPR (Localized surface plasmon resonance) contribution effect which occurs only in TM polarization [178] and becomes a dominant mechanism when the aspect ratio of the nanowire approaches its resonant frequency. We have henceforth named this influence as *"plasmo-plasmonic effect"*.

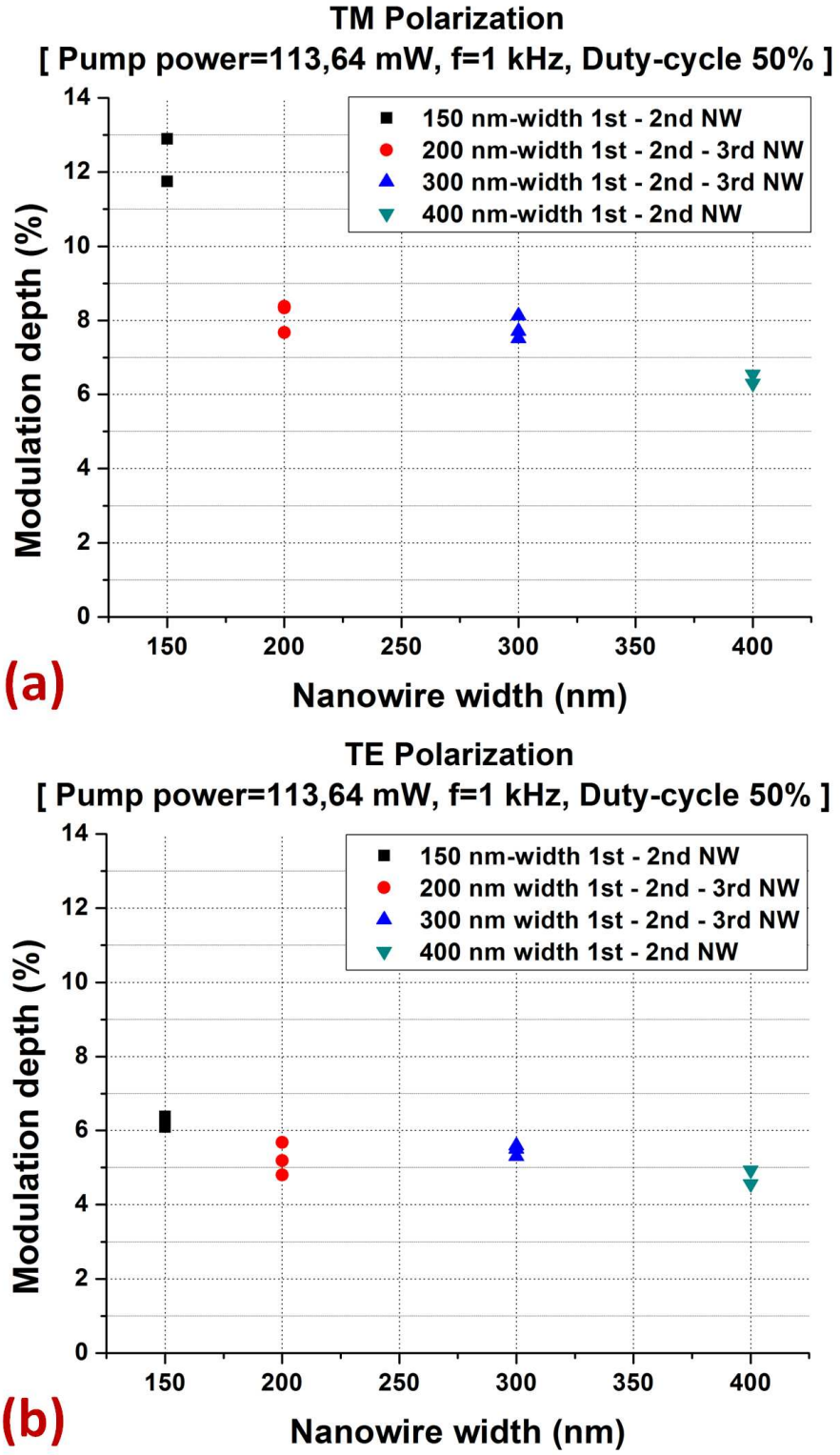


Figure 4.23: (a) (resp. b) Modulation depths of nanowires ranging from 150 to 400 nm are displayed at the maximum power of 113.6 mW for TM (resp. TE) polarization (f=1 kHz, Duty-cycle=50%)

## 4.5 Conclusion

In summary, we have investigated photo-thermal modulation of SPPs propagation along lithographically fabricated gold nanowires sustaining highly confined plasmon mode at telecom wavelengths. By operating a specific fiber-to-fiber homemade confocal detection configuration in conjunction with a leakage radiation microscope set-up, first we have performed a 10 GHz NRZ signal transmission experiment along the nanowires. A negligible BER power penalty for 10 GHz NRZ signal transmission demonstrates that this kind of nanowires is convenient for a high-bit-rate traffic over short distances at telecom wavelengths.

Secondly, we have performed photo-thermal modulation of SPPs propagation by illuminating nanowires with an electro-optically modulated CW visible laser. We have observed that the modulation depth is larger for thinner nanowires whatever the polarization of the incident beam. This result arises from the larger damping and hence larger field penetration into the metal of the SPP mode sustained by narrow nanowires. On the other hand, the modulation depth can be controlled by the polarization of the incident beam. In TM polarization, we have noticed a considerable increase in modulation depth for thinner nanowires which can be explained as the enhancement of the modulation depths due to LSPR (Localized surface plasmon resonance) contribution effect which becomes gradually a dominant mechanism when the aspect ratio of the nanowire approaches its resonant frequency.

Thirdly, we have previously obtained photo-thermal modulation depth as 4.5% for thin gold film sustaining air/gold SPP mode [140] whereas, in here, we have found a greater modulation depth value as 12.9% for a 150 nm-width nanowire ($\lambda$/10) sustaining short range SPP mode at TM polarization which is definitely a strong evidence of outstanding property of highly confined SPP mode along subwavelength nanowires.

As a result, we have demonstrated that lithographically fabricated thinner gold NWs are not only promising elements with their large thermo-plasmonic coefficient for nonlinear optical devices and thermo-optical based applications but also convenient for a high-bit rate traffic at telecom wavelengths.

# Conclusions and Future works

Plasmonics has been continuing to attract interests due to its versatile properties for realizing such as fast interconnects, improved resolution microscopes, efficient LEDs and sensitive chemical and biological detectors [5]. Plasmonic circuitry could be implemented in near future in order to perform ultrafast speed computers and optoelectronic devices [11]. Many works have been demonstrated as passive devices so far. But efficient, compact, and carrying high modulation features active devices are still needed. So we have surveyed thermo-optical (TO) and thermo-plasmonic properties of a noble metal sustaining various SPP mode at telecom wavelengths when photo-excited by either CW or nanosecond regime in order to reveal nonlinear effects.

In this context, first of all, we have investigated the photo-thermal modulation of thin film SPP mode launched at a gold/air interface at telecom frequencies by operating a specific fiber-to-fiber detection configuration in conjunction with a leakage radiation microscope (LRM) set-up [140]. It has been found that the photo-thermal modulation depth is proportional to the thermo-plasmonic coefficient defined as the temperature derivative of the damping constant of the mode. In addition, we have demonstrated that the thermo-plasmonic coefficient can be readily computed by using the experimental depth of modulation and the temperature distribution along the gold film computed numerically. Next, we have proposed a figure of merit which can be useful to characterize the thermal properties of a metal at a given wavelength. Subsequently, we have extracted the thermo-optical coefficients (TOCs) of gold at telecom wavelengths which may be helpful in TO based plasmonic devices for datacom applications. Finally, we checked the reliability of our gold TOCs by performing photo-thermal experiments with a pulsed nanosecond laser. Although the computed modulation depth for pulsed illumination are underestimated by about 17% compared to the experimental values, we can conclude that the gold TOCs obtained in this work are reasonable and can be useful for anticipating thermal effects on SPP modes supported by gold at telecom wavelengths.

Secondly, we have investigated the thermo-optical dynamics of polymer loaded surface plasmon waveguide (PLSPPW) based devices by exciting photo-thermally in the nanosecond regime [133]. It has been observed that a response time for the thermo-absorption of the PLSPPW mode is found to be in the nanosecond regime at the scale of the pulse duration. We have demonstrated that the thermo-absorption of the PLSPPW mode is mediated not only by the temperature-dependent metal ohmic losses but also by the field distribution of the PLSPPW mode into the metal controlled by the polymer TOCs. It has been demonstrated that a sub-$\mu$s

thermo-modulation characteristic time (fall time+rise time) about four-fold shorter than the cooling time of the metal film itself. Besides, the thermo-absorption amplitude for a PLSPPW mode has been found to be about 10 times larger than for a Au/air interface SPPs photo-excited in the same conditions. Furthermore, we have investigated the thermo-optical response of a PLSPPW based racetrack shaped resonator coupled to a straight bus waveguide and evaluate the photo-thermal activation. It is found that the nanosecond pulse can activate the resonator at a time scale of 300 ns however followed by a characteristic cooling time of about 18 $\mu$s in our configuration. We attribute these slow TO dynamics of the resonators due to the poor thermal diffusivity of both the polymer and the glass substrate used in this work. Although these poor thermal performances are not sufficient to realize high-speed TO devices, the nanosecond photo-thermal excitation is convenient for sub-$\mu$s activation which is the key feature for the fast pre-conditioning of the TO devices.

Finally, we have investigated photo-thermal modulation of SPPs propagation along lithographically fabricated gold nanowires sustaining highly confined plasmon mode at telecom wavelengths. By using a specific fiber-to-fiber homemade confocal detection setup, first we have performed a high-bit rate signal transmission experiment along the nanowires at telecom wavelengths. We have found a negligible BER power penalty for 10 GHz NRZ signal transmission demonstrates that this kind of nanowires is convenient for a high-bit-rate traffic over short distances at telecom wavelengths. After that, we have demonstrated photo-thermal modulation of SPPs propagation along nanowires by illuminating them with an electro-optically modulated CW visible laser. It has been observed that the modulation depth is larger for thinner nanowires whatever the polarization of the incident beam. This result arises from the larger damping and hence larger field penetration into the metal of the SPP mode sustained by narrow nanowires. In addition, the modulation depth can be controlled by the polarization of the incident beam. In TM polarization, we have noticed a considerable increase in modulation depth for thinner nanowires which can be explained as the enhancement of the modulation depths due to LSPR (Localized surface plasmon resonance), named as "plasmo-plasmonic effect". Besides, we have previously obtained photo-thermal modulation depth as 4.5% for thin gold film sustaining air/gold SPP mode whereas, in here, we have found a greater modulation depth value as 12.9% for a 150 nm-width nanowire ($\lambda$/10) sustaining short range SPP mode at TM polarization which is definitely a strong evidence of outstanding property of highly confined SPP mode along subwavelength nanowires. As a conclusion, lithographically fabricated thinner gold NWs are not only promising elements for TO based applications with their large TOCs but also can be used safely for a high-bit rate traffic at telecom wavelengths.

For the future research, although there is not a single material choice for plasmonic applications, Aluminum (Al), frequently used metal in semiconductor technology, can be considered as a prospective candidate for the investigation of TOCs, photo-thermal modulation and characterization of the temporal dynamics of SPPs propagation. So far, it has been rarely employed in plasmonic applications due to the larger plasma frequency which leads to its localized surface plasmon response to be found in the ultraviolet (UV) region while the gold one's takes place in the visible and NIR region that is why frequently used. Nevertheless, Al may play a critical role for merging plasmonics and semiconductor technology in near future.

On the other hand, although lithographically fabricated gold nanowire plasmonic waveguides was investigated in continuous wave (CW) regime, the nanosecond pulsed photo-thermal approach of this type of metallic plasmonic waveguides has not been considered in

this thesis. So it would be fruitful to handle this type of research for next generation thermo-optical based plasmonic devices.

# Bibliography


[1] P. R. West, S. Ishii, G. V. Naik, N. K. Emani, V. M. Shalaev, and A. Boltasseva, "Searching for better plasmonic materials," *Laser & Photonics Reviews*, vol. 4, no. 6, pp. 795–808, 2010.

[2] G. V. Naik and A. Boltasseva, "Semiconductors for plasmonics and metamaterials," *physica status solidi (RRL)-Rapid Research Letters*, vol. 4, no. 10, pp. 295–297, 2010.

[3] M. L. Brongersma, J. W. Hartman, and H. A. Atwater, "Plasmonics: Electromagnetic energy transfer and switching in nanoparticle chain-arrays below the diffraction limit," *MRS Proceedings*, vol. 582:H10.5, 1999.

[4] S. A. Maier and H. A. Atwater, "Plasmonics: Localization and guiding of electromagnetic energy in metal/dielectric structures," *Journal of Applied Physics*, vol. 98, no. 1, pp. 011101–011101, 2005.

[5] H. A. Atwater, "The promise of plasmonics," *Scientific American*, vol. 296, no. 4, pp. 56–62, 2007.

[6] R. H. Ritchie, "Plasma losses by fast electrons in thin films," *Phys. Rev.*, vol. 106, pp. 874–881, 1957.

[7] W. L. Barnes, A. Dereux, and T. W. Ebbesen, "Surface plasmon subwavelength optics," *Nature*, vol. 424, no. 6950, pp. 824–830, 2003.

[8] R. Zia, J. A. Schuller, A. Chandran, and M. L. Brongersma, "Plasmonics: the next chip-scale technology," *Materials today*, vol. 9, no. 7, pp. 20–27, 2006.

[9] M. L. Brongersma and V. M. Shalaev, "Applied physics the case for plasmonics," *Science*, vol. 328, no. 5977, pp. 440–441, 2010.

[10] E. Özbay, "Plasmonics: Merging photonics and electronics at nanoscale dimensions," *Science*, vol. 311, no. 5758, pp. 189–193, 2006.

[11] T. W. Ebbesen, C. Genet, and S. I. Bozhevolnyi, "Surface-plasmon circuitry," *Physics Today*, vol. 61, no. 5, p. 44, 2008.

[12] D. Kalavrouziotis, S. Papaioannou, K. Vyrsokinos, L. Markey, A. Dereux, G. Giannoulis, D. Apostolopoulos, H. Avramopoulos, and N. Pleros, "Demonstration of a plasmonic MMI switch in 10-Gb/s true data traffic conditions," *IEEE Photonics Technology Letters*, vol. 24, pp. 1819–1822, 2012.

[13] D. Kalavrouziotis, S. Papaioannou, K. Vyrsokinos, A. Kumar, S. I. Bozhevolnyi, K. Hassan, L. Markey, J.-C. Weeber, A. Dereux, G. Giannoulis, *et al.*, "Active plasmonics in true data traffic applications: Thermo optic ON/OFF gating using a silicon-plasmonic asymmetric mach-zehnder interferometer," *IEEE Photonics Tech. Lett*, vol. 24, no. 12, pp. 1036–1038, 2012.

[14] S. Papaioannou, D. Kalavrouziotis, K. Vyrsokinos, J.-C. Weeber, K. Hassan, L. Markey, A. Dereux, A. Kumar, S. I. Bozhevolnyi, M. Baus, *et al.*, "Active plasmonics in WDM traffic switching applications," *Scientific reports*, vol. 2, 2012.

[15] G. Giannoulis, D. Kalavrouziotis, D. Apostolopoulos, S. Papaioannou, A. Kumar, S. Bozhevolnyi, L. Markey, K. Hassan, J.-C. Weeber, A. Dereux, *et al.*, "Data transmission and thermo-optic tuning performance of dielectric-loaded plasmonic structures hetero-integrated on a silicon chip," *IEEE Photonics Technology Letters*, vol. 24, no. 5, p. 374, 2012.

[16] J. Gosciniak, S. I. Bozhevolnyi, T. B. Andersen, V. S. Volkov, J. Kjelstrup-Hansen, L. Markey, and A. Dereux, "Thermo-optic control of dielectric-loaded plasmonic waveguide components," *Opt. Express*, vol. 18, no. 2, pp. 1207–1216, 2010.

[17] J.-C. Weeber, K. Hassan, L. Saviot, A. Dereux, C. Boissière, O. Durupthy, C. Chaneac, E. Burov, and A. Pastouret, "Efficient photo-thermal activation of gold nanoparticle-doped polymer plasmonic switches," *Optics express*, vol. 20, no. 25, pp. 27636–27649, 2012.

[18] M. Noginov, V. A. Podolskiy, G. Zhu, M. Mayy, M. Bahoura, J. Adegoke, B. Ritzo, and K. Reynolds, "Compensation of loss in propagating surface plasmon polariton by gain in adjacent dielectric medium," *Optics express*, vol. 16, no. 2, pp. 1385–1392, 2008.

[19] I. De Leon and P. Berini, "Amplification of long-range surface plasmons by a dipolar gain medium," *Nature Photonics*, vol. 4, no. 6, pp. 382–387, 2010.

[20] R. Schenker and V. Singh, "Foundations for scaling beyond 14nm," in *Custom Integrated Circuits Conference (CICC), 2013 IEEE*, pp. 1–4, IEEE, 2013.

[21] L. R. Hirsch, R. J. Stafford, J. A. Bankson, S. R. Sershen, B. Rivera, R. E. Price, J. D. Hazle, N. J. Halas, and J. L. West, "Nanoshell-mediated near-infrared thermal therapy of tumors under magnetic resonance guidance," *Proceedings of the National Academy of Sciences*, vol. 100, no. 23, pp. 13549–13554, 2003.

[22] C. Loo, A. Lin, L. Hirsch, M.-H. Lee, J. Barton, N. Halas, J. West, and R. Drezek, "Nanoshell-enabled photonics-based imaging and therapy of cancer," *Technology in cancer research & treatment*, vol. 3, no. 1, 2004.

[23] N. E. Hecker, R. A. Hopfel, N. Sawaki, T. Maier, and G. Strasser, "Surface plasmon-enhanced photoluminescence from a single quantum well," *Applied physics letters*, vol. 75, no. 11, pp. 1577–1579, 1999.

[24] K. Okamoto, I. Niki, A. Shvartser, Y. Narukawa, T. Mukai, and A. Scherer, "Surface-plasmon-enhanced light emitters based on ingan quantum wells," *Nature materials*, vol. 3, no. 9, pp. 601–605, 2004.

[25] D. J. Bergman and M. I. Stockman, "Surface plasmon amplification by stimulated emission of radiation: Quantum generation of coherent surface plasmons in nanosystems," *Physical review letters*, vol. 90, no. 2, p. 027402, 2003.

[26] M. A. Noginov, G. Zhu, A. M. Belgrave, R. Bakker, V. M. Shalaev, E. E. Narimanov, S. Stout, E. Herz, T. Suteewong, and U. Wiesner, "Demonstration of a spaser-based nanolaser," *Nature*, vol. 460, no. 7259, pp. 1110–1112, 2009.

[27] A. Campion and P. Kambhampati, "Surface-enhanced raman scattering," *Chem. Soc. Rev.*, vol. 27, no. 4, pp. 241–250, 1998.

[28] X. Luo and T. Ishihara, "Surface plasmon resonant interference nanolithography technique," *Applied Physics Letters*, vol. 84, no. 23, pp. 4780–4782, 2004.

[29] W. Srituravanich, N. Fang, C. Sun, Q. Luo, and X. Zhang, "Plasmonic nanolithography," *Nano letters*, vol. 4, no. 6, pp. 1085–1088, 2004.

[30] N. W. Ashcroft and N. D. Mermin, *Solid State Physics*. Saunders College, Philadelphia, 1976.

[31] J. A. Stratton, *Electromagnetic Theory*. McGraw-Hill, 1941.

[32] H. P. Myers, *Introductory solid state physics*. Taylor & Francis, London, 1990.

[33] C. J. Powell and J. Swan, "Origin of the characteristic electron energy losses in aluminum," *Physical Review*, vol. 115, no. 4, p. 869, 1959.

[34] H. Raether, "Surface plasmons on smooth and rough surfaces and on gratings," *Springer-Verlag, Berlin*, 1988.

[35] S. A. Maier, *Plasmonics: fundamentals and applications*. Springer Science & Business Media, 2007.

[36] B. Prade, J. Vinet, and A. Mysyrowicz, "Guided optical waves in planar heterostructures with negative dielectric constant," *Physical Review B*, vol. 44, no. 24, p. 13556, 1991.

[37] M. V. Bashevoy, F. Jonsson, A. V. Krasavin, N. I. Zheludev, Y. Chen, and M. I. Stockman, "Generation of traveling surface plasmon waves by free-electron impact," *Nano letters*, vol. 6, no. 6, pp. 1113–1115, 2006.

[38] W. Cai, R. Sainidou, J. Xu, A. Polman, and F. J. García de Abajo, "Efficient generation of propagating plasmons by electron beams," *Nano letters*, vol. 9, no. 3, pp. 1176–1181, 2009.

[39] P. Bharadwaj, A. Bouhelier, and L. Novotny, "Electrical excitation of surface plasmons," *Physical Review Letters*, vol. 106, no. 22, p. 226802, 2011.

[40] A. Otto, "Excitation of nonradiative surface plasma waves in silver by the method of frustrated total reflection," *Zeitschrift für Physik*, vol. 216, no. 4, pp. 398–410, 1968.

[41] E. Kretschmann and H. Raether, "Radiative decay of non radiative surface plasmons excited by light (surface plasma waves excitation by light and decay into photons applied to nonradiative modes)," *Zeitschrift Fuer Naturforschung, Teil A*, vol. 23, p. 2135, 1968.

[42] E. N. Economou, "Surface plasmons in thin films," *Physical Review*, vol. 182, no. 2, p. 539, 1969.

[43] D. Sarid, "Long-range surface-plasma waves on very thin metal films," *Physical Review Letters*, vol. 47, no. 26, p. 1927, 1981.

[44] A. E. Craig, G. A. Olson, and D. Sarid, "Experimental observation of the long-range surface-plasmon polariton," *Optics letters*, vol. 8, no. 7, pp. 380–382, 1983.

[45] J. J. Burke, G. I. Stegeman, and T. Tamir, "Surface-polariton-like waves guided by thin, lossy metal films," *Physical Review B*, vol. 33, no. 8, p. 5186, 1986.

[46] F. Yang, J. R. Sambles, and G. W. Bradberry, "Long-range surface modes supported by thin films," *Physical Review B*, vol. 44, no. 11, p. 5855, 1991.

[47] P. Berini, "Plasmon-polariton waves guided by thin lossy metal films of finite width: Bound modes of symmetric structures," *Physical Review B*, vol. 61, no. 15, p. 10484, 2000.

[48] P. Berini, "Plasmon-polariton waves guided by thin lossy metal films of finite width: Bound modes of asymmetric structures," *Physical Review B*, vol. 63, no. 12, p. 125417, 2001.

[49] J.-C. Weeber, J. R. Krenn, A. Dereux, B. Lamprecht, Y. Lacroute, and J. P. Goudonnet, "Near-field observation of surface plasmon polariton propagation on thin metal stripes," *Physical review B*, vol. 64, no. 4, p. 045411, 2001.

[50] R. Charbonneau, P. Berini, E. Berolo, and E. Lisicka-Shrzek, "Experimental observation of plasmon polariton waves supported by a thin metal film of finite width," *Optics letters*, vol. 25, no. 11, pp. 844–846, 2000.

[51] R. C. Reddick, R. J. Warmack, and T. L. Ferrell, "New form of scanning optical microscopy," *Physical Review B*, vol. 39, no. 1, p. 767, 1989.

[52] J.-C. Weeber, Y. Lacroute, and A. Dereux, "Optical near-field distributions of surface plasmon waveguide modes," *Physical Review B*, vol. 68, no. 11, p. 115401, 2003.

[53] P. Berini, R. Charbonneau, N. Lahoud, and G. Mattiussi, "Characterization of long-range surface-plasmon-polariton waveguides," *Journal of Applied Physics*, vol. 98, no. 4, pp. 043109–043109, 2005.

[54] P. Berini and I. De Leon, "Surface plasmon-polariton amplifiers and lasers," *Nature Photonics*, vol. 6, no. 1, pp. 16–24, 2012.

[55] M. Nezhad, K. Tetz, and Y. Fainman, "Gain assisted propagation of surface plasmon polaritons on planar metallic waveguides," *Optics Express*, vol. 12, no. 17, pp. 4072–4079, 2004.

[56] J. Seidel, S. Grafström, and L. Eng, "Stimulated emission of surface plasmons at the interface between a silver film and an optically pumped dye solution," *Physical review letters*, vol. 94, no. 17, p. 177401, 2005.

[57] J. Grandidier, G. Colas des Francs, S. Massenot, A. Bouhelier, L. Markey, J. Weeber, C. Finot, and A. Dereux, "Gain-assisted propagation in a plasmonic waveguide at telecom wavelength," *Nano letters*, vol. 9, no. 8, pp. 2935–2939, 2009.

[58] A. Hohenau, J. R. Krenn, A. L. Stepanov, A. Drezet, H. Ditlbacher, B. Steinberger, A. Leitner, and F. R. Aussenegg, "Dielectric optical elements for surface plasmons," *Optics letters*, vol. 30, no. 8, pp. 893–895, 2005.

[59] B. Steinberger, A. Hohenau, H. Ditlbacher, A. L. Stepanov, A. Drezet, F. R. Aussenegg, A. Leitner, and J. R. Krenn, "Dielectric stripes on gold as surface plasmon waveguides," *Applied Physics Letters*, vol. 88, no. 9, pp. 094104–094104, 2006.

[60] T. Holmgaard and S. I. Bozhevolnyi, "Theoretical analysis of dielectric-loaded surface plasmon-polariton waveguides," *Physical Review B*, vol. 75, no. 24, p. 245405, 2007.

[61] T. Holmgaard, Z. Chen, S. I. Bozhevolnyi, L. Markey, A. Dereux, A. V. Krasavin, A. V. Zayats, *et al.*, "Bend-and splitting loss of dielectric-loaded surface plasmon-polariton waveguides," *Opt. Express*, vol. 16, no. 18, pp. 13585–13592, 2008.

[62] J. Grandidier, S. Massenot, G. Colas des Francs, A. Bouhelier, J.-C. Weeber, L. Markey, A. Dereux, J. Renger, M. U. González, and R. Quidant, "Dielectric-loaded surface plasmon polariton waveguides: Figures of merit and mode characterization by image and fourier plane leakage microscopy," *Physical Review B*, vol. 78, no. 24, p. 245419, 2008.

[63] A. Bouhelier and G. P. Wiederrecht, "Surface plasmon rainbow jets," *Optics letters*, vol. 30, no. 8, pp. 884–886, 2005.

[64] S. Massenot, J. Grandidier, A. Bouhelier, G. Colas des Francs, L. Markey, J.-C. Weeber, A. Dereux, J. Renger, M. U. Gonzàlez, and R. Quidant, "Polymer-metal waveguides characterization by fourier plane leakage radiation microscopy," *Applied Physics Letters*, vol. 91, no. 24, pp. 243102–243102, 2007.

[65] S. Massenot, J.-C. Weeber, A. Bouhelier, G. Colas des Francs, J. Grandidier, L. Markey, and A. Dereux, "Differential method for modeling dielectric-loaded surface plasmon polariton waveguides," *Optics express*, vol. 16, no. 22, pp. 17599–17608, 2008.

[66] K. Hassan, J.-C. Weeber, L. Markey, and A. Dereux, "Thermo-optical control of dielectric loaded plasmonic racetrack resonators," *Journal of Applied Physics*, vol. 110, p. 023106, 2011.

[67] K. Hassan, J.-C. Weeber, L. Markey, A. Dereux, A. Pitilakis, O. Tsilipakos, and E. Kriezis, "Thermo-optic plasmo-photonic mode interference switches based on dielectric loaded waveguides," *Applied Physics Letters*, vol. 99, no. 24, pp. 241110–241110, 2011.

[68] S. Papaioannou, K. Vyrsokinos, O. Tsilipakos, A. Pitilakis, K. Hassan, J.-C. Weeber, L. Markey, A. Dereux, S. I. Bozhevolnyi, A. Miliou, *et al.*, "A 320 Gb/s-throughput capable 2x2 silicon-plasmonic router architecture for optical interconnects," *Lightwave Technology, Journal of*, vol. 29, no. 21, pp. 3185–3195, 2011.

[69] D. F. Pile, T. Ogawa, D. K. Gramotnev, T. Okamoto, M. Haraguchi, M. Fukui, and S. Matsuo, "Theoretical and experimental investigation of strongly localized plasmons on triangular metal wedges for subwavelength waveguiding," *Applied Physics Letters*, vol. 87, no. 6, p. 061106, 2005.

[70] K. C. Vernon, D. K. Gramotnev, and D. F. Pile, "Adiabatic nanofocusing of plasmons by a sharp metal wedge on a dielectric substrate," *Journal of applied physics*, vol. 101, no. 10, p. 104312, 2007.

[71] E. Moreno, S. G. Rodrigo, S. I. Bozhevolnyi, L. Martin-Moreno, and F. Garcia-Vidal, "Guiding and focusing of electromagnetic fields with wedge plasmon polaritons," *Physical review letters*, vol. 100, no. 2, p. 023901, 2008.

[72] A. Boltasseva, V. S. Volkov, R. B. Nielsen, E. Moreno, S. G. Rodrigo, and S. I. Bozhevolnyi, "Triangular metal wedges for subwavelength plasmon-polariton guiding at telecom wavelengths," *Optics express*, vol. 16, no. 8, pp. 5252–5260, 2008.

[73] R. F. Oulton, V. J. Sorger, D. Genov, D. Pile, and X. Zhang, "A hybrid plasmonic waveguide for subwavelength confinement and long-range propagation," *Nature Photonics*, vol. 2, no. 8, pp. 496–500, 2008.

[74] R. M. Briggs, J. Grandidier, S. P. Burgos, E. Feigenbaum, and H. A. Atwater, "Efficient coupling between dielectric-loaded plasmonic and silicon photonic waveguides," *Nano letters*, vol. 10, no. 12, pp. 4851–4857, 2010.

[75] A. Graff, D. Wagner, H. Ditlbacher, and U. Kreibig, "Silver nanowires," *The European Physical Journal D-Atomic, Molecular, Optical and Plasma Physics*, vol. 34, no. 1-3, pp. 263–269, 2005.

[76] H. Ditlbacher, A. Hohenau, D. Wagner, U. Kreibig, M. Rogers, F. Hofer, F. R. Aussenegg, and J. R. Krenn, "Silver nanowires as surface plasmon resonators," *Physical review letters*, vol. 95, no. 25, p. 257403, 2005.

[77] P. Kusar, C. Gruber, A. Hohenau, and J. R. Krenn, "Measurement and reduction of damping in plasmonic nanowires," *Nano letters*, vol. 12, no. 2, pp. 661–665, 2012.

[78] J. Takahara, S. Yamagishi, H. Taki, A. Morimoto, and T. Kobayashi, "Guiding of a one-dimensional optical beam with nanometer diameter," *Optics letters*, vol. 22, no. 7, pp. 475–477, 1997.

[79] J.-C. Weeber, A. Dereux, C. Girard, J. R. Krenn, and J.-P. Goudonnet, "Plasmon polaritons of metallic nanowires for controlling submicron propagation of light," *Physical Review B*, vol. 60, no. 12, p. 9061, 1999.

[80] R. M. Dickson and L. A. Lyon, "Unidirectional plasmon propagation in metallic nanowires," *The Journal of Physical Chemistry B*, vol. 104, no. 26, pp. 6095–6098, 2000.

[81] G. Schider, J. R. Krenn, A. Hohenau, H. Ditlbacher, A. Leitner, F. R. Aussenegg, W. L. Schaich, I. Puscasu, B. Monacelli, and G. Boreman, "Plasmon dispersion relation of Au and Ag nanowires," *Phys. Rev. B*, vol. 68, p. 155427, 2003.

[82] E. Verhagen, M. Spasenović, A. Polman, and L. K. Kuipers, "Nanowire plasmon excitation by adiabatic mode transformation," *Physical review letters*, vol. 102, no. 20, p. 203904, 2009.

[83] D. F. Pile, T. Ogawa, D. K. Gramotnev, Y. Matsuzaki, K. C. Vernon, K. Yamaguchi, T. Okamoto, M. Haraguchi, and M. Fukui, "Two-dimensionally localized modes of a nanoscale gap plasmon waveguide," *Applied Physics Letters*, vol. 87, no. 26, p. 261114, 2005.

[84] P. Neutens, P. Van Dorpe, I. De Vlaminck, L. Lagae, and G. Borghs, "Electrical detection of confined gap plasmons in metal–insulator–metal waveguides," *Nature Photonics*, vol. 3, no. 5, pp. 283–286, 2009.

[85] H. Choo, M.-K. Kim, M. Staffaroni, T. J. Seok, J. Bokor, S. Cabrini, P. J. Schuck, M. C. Wu, and E. Yablonovitch, "Nanofocusing in a metal-insulator-metal gap plasmon waveguide with a three-dimensional linear taper," *Nature Photonics*, vol. 6, no. 12, pp. 838–844, 2012.

[86] L. Liu, Z. Han, and S. He, "Novel surface plasmon waveguide for high integration," *Optics Express*, vol. 13, no. 17, pp. 6645–6650, 2005.

[87] W. Cai, W. Shin, S. Fan, and M. L. Brongersma, "Elements for plasmonic nanocircuits with three-dimensional slot waveguides," *Advanced materials*, vol. 22, no. 45, pp. 5120–5124, 2010.

[88] G. Veronis and S. Fan, "Guided subwavelength plasmonic mode supported by a slot in a thin metal film," *Optics letters*, vol. 30, no. 24, pp. 3359–3361, 2005.

[89] J. Dionne, L. Sweatlock, H. Atwater, and A. Polman, "Plasmon slot waveguides: Towards chip-scale propagation with subwavelength-scale localization," *Physical Review B*, vol. 73, no. 3, p. 035407, 2006.

[90] A. Melikyan, L. Alloatti, A. Muslija, D. Hillerkuss, P. Schindler, J. Li, R. Palmer, D. Korn, S. Muehlbrandt, D. Van Thourhout, *et al.*, "High-speed plasmonic phase modulators," *Nature Photonics*, vol. 8, no. 3, pp. 229–233, 2014.

[91] T. Nikolajsen, K. Leosson, and S. I. Bozhevolnyi, "In-line extinction modulator based on long-range surface plasmon polaritons," *Optics communications*, vol. 244, no. 1, pp. 455–459, 2005.

[92] G. Gagnon, N. Lahoud, G. A. Mattiussi, and P. Berini, "Thermally activated variable attenuation of long-range surface plasmon-polariton waves," *Lightwave Technology, Journal of*, vol. 24, no. 11, pp. 4391–4402, 2006.

[93] O. Tsilipakos, T. V. Yioultsis, and E. E. Kriezis, "Theoretical analysis of thermally tunable microring resonator filters made of dielectric-loaded plasmonic waveguides," *Journal of Applied Physics*, vol. 106, no. 9, p. 093109, 2009.

[94] A. Pitilakis and E. E. Kriezis, "Longitudinal 2 x 2 switching configurations based on thermo-optically addressed dielectric-loaded plasmonic waveguides," *Lightwave Technology, Journal of*, vol. 29, no. 17, pp. 2636–2646, 2011.

[95] J. Gosciniak and S. I. Bozhevolnyi, "Performance of thermo-optic components based on dielectric-loaded surface plasmon polariton waveguides," *Scientific reports*, vol. 3, 2013.

[96] H. Fan and P. Berini, "Thermo-optic characterization of long-range surface-plasmon devices in cytop," *Applied optics*, vol. 52, no. 2, pp. 162–170, 2013.

[97] A. L. Lereu, A. Passian, J. P. Goudonnet, T. Thundat, and T. L. Ferrell, "Optical modulation processes in thin films based on thermal effects of surface plasmons," *Applied Physics Letters*, vol. 86, no. 15, pp. 154101–154101, 2005.

[98] A. Passian, A. Lereu, E. Arakawa, A. Wig, T. Thundat, and T. Ferrell, "Modulation of multiple photon energies by use of surface plasmons," *Optics letters*, vol. 30, no. 1, pp. 41–43, 2005.

[99] X.-Y. Zhang, T. Zhang, A.-M. Hu, X.-J. Xue, P.-Q. Wu, and Q.-Y. Chen, "Tunable microring resonator based on dielectric-loaded surface plasmon-polariton waveguides," in *Nanoelectronics Conference (INEC), 2010 3rd International*, pp. 1355–1356, IEEE, 2010.

[100] C. Kittel, "Introduction to solid state physics," 2005.

[101] M. Rashidi-Huyeh and B. Palpant, "Counterintuitive thermo-optical response of metal-dielectric nanocomposite materials as a result of local electromagnetic field enhancement," *Physical Review B*, vol. 74, no. 7, p. 075405, 2006.

[102] B. Palpant, M. Rashidi-Huyeh, B. Gallas, S. Chenot, and S. Fisson, "Highly dispersive thermo-optical properties of gold nanoparticles," *Applied physics letters*, vol. 90, no. 22, p. 223105, 2007.

[103] F. Wooten, *Optical properties of solids*. Academic Press, 1972.

[104] R. H. Doremus, "Optical properties of small gold particles," *The Journal of Chemical Physics*, vol. 40, no. 8, pp. 2389–2396, 1964.

[105] G. P. Pells and M. Shiga, "The optical properties of copper and gold as a function of temperature," *Journal of Physics C: Solid State Physics*, vol. 2, no. 10, p. 1835, 1969.

[106] K. Ujihara, "Reflectivity of metals at high temperatures," *Journal of Applied Physics*, vol. 43, no. 5, pp. 2376–2383, 1972.

[107] R. Rosei, F. Antonangeli, and U. M. Grassano, "d bands position and width in gold from very low temperature thermomodulation measurements," *Surface Science*, vol. 37, pp. 689–699, 1973.

[108] P. Winsemius, M. Guerrisi, and R. Rosei, "Splitting of the interband absorption edge in au: Temperature dependence," *Physical Review B*, vol. 12, no. 10, p. 4570, 1975.

[109] P. Winsemius, F. F. Van Kampen, H. P. Lengkeek, and C. G. Van Went, "Temperature dependence of the optical properties of Au, Ag and Cu," *Journal of Physics F: Metal Physics*, vol. 6, no. 8, p. 1583, 1976.

[110] R. Rosei and D. W. Lynch, "Thermomodulation spectra of Al, Au and Cu," *Physical Review B*, vol. 5, no. 10, p. 3883, 1972.

[111] T. Holstein, "Theory of transport phenomena in an electron-phonon gas," *Annals of Physics*, vol. 29, no. 3, pp. 410–535, 1964.

[112] R. N. Gurzhi, "Mutual electron correlations in metal optics," *Soviet Physics Jetp-Ussr*, vol. 8, no. 4, pp. 673–675, 1959.

[113] J. A. McKay and J. A. Rayne, "Temperature dependence of the infrared absorptivity of the noble metals," *Physical Review B*, vol. 13, no. 2, p. 673, 1976.

[114] G. Baffou and R. Quidant, "Thermo-plasmonics: using metallic nanostructures as nano-sources of heat," *Laser & Photonics Reviews*, vol. 7, no. 2, pp. 171–187, 2013.

[115] M. Liu, M. Pelton, and P. Guyot-Sionnest, "Reduced damping of surface plasmons at low temperatures," *Physical Review B*, vol. 79, no. 3, p. 035418, 2009.

[116] J.-S. G. Bouillard, W. Dickson, D. P. O'Connor, G. A. Wurtz, and A. V. Zayats, "Low-temperature plasmonics of metallic nanostructures," *Nano letters*, vol. 12, no. 3, pp. 1561–1565, 2012.

[117] R. T. Beach and R. W. Christy, "Electron-electron scattering in the intraband optical conductivity of Cu, Ag and Au," *Physical Review B*, vol. 16, no. 12, p. 5277, 1977.

[118] G. R. Parkins, W. E. Lawrence, and R. W. Christy, "Intraband optical conductivity $\sigma$ ($\omega$, t) of Cu, Ag and Au: Contribution from electron-electron scattering," *Physical Review B*, vol. 23, no. 12, p. 6408, 1981.

[119] C. S. Moreira, A. M. N. Lima, H. Neff, and C. Thirstrup, "Temperature-dependent sensitivity of surface plasmon resonance sensors at the gold–water interface," *Sensors and Actuators B: Chemical*, vol. 134, no. 2, pp. 854–862, 2008.

[120] G. Turhan-Sayan and Ş. K. Özdemir, "Temperature effects on surface plasmon resonance: design considerations for an optical temperature sensor," *Journal of Lightwave Technology*, vol. 21, no. 3, p. 805, 2003.

[121] M. G. Nielsen, J.-C. Weeber, K. Hassan, J. Fatome, C. Finot, S. Kaya, L. Markey, O. Albrektsen, S. I. Bozhevolnyi, G. Millot, and A. Dereux, "Grating couplers for fiber-to-fiber characterizations of stand-alone dielectric loaded surface plasmon waveguide components," *Journal of Lightwave Technology*, vol. 30, no. 19, pp. 3118–3125, 2012.

[122] D. W. Pohl, W. Denk, and M. Lanz, "Optical stethoscopy: Image recording with resolution $\lambda$/20," *Applied physics letters*, vol. 44, no. 7, pp. 651–653, 1984.

[123] U. Dürig, D. W. Pohl, and F. Rohner, "Near-field optical-scanning microscopy," *Journal of applied physics*, vol. 59, no. 10, pp. 3318–3327, 1986.

[124] D. W. Pohl, "Scanning near-field optical microscopy (snom)," *Advances in optical and electron microscopy*, vol. 12, pp. 243–312, 1991.

[125] P. Dawson, F. De Fornel, and J.-P. Goudonnet, "Imaging of surface plasmon propagation and edge interaction using a photon scanning tunneling microscope," *Physical review letters*, vol. 72, no. 18, p. 2927, 1994.

[126] B. Hecht, H. Bielefeldt, L. Novotny, Y. Inouye, and D. W. Pohl, "Local excitation, scattering, and interference of surface plasmons," *Physical review letters*, vol. 77, no. 9, p. 1889, 1996.

[127] A. Bouhelier, T. Huser, H. Tamaru, H. J. Güntherodt, D. W. Pohl, F. I. Baida, and D. Van Labeke, "Plasmon optics of structured silver films," *Physical Review B*, vol. 63, no. 15, p. 155404, 2001.

[128] A. Drezet, A. Hohenau, D. Koller, A. Stepanov, H. Ditlbacher, B. Steinberger, F. R. Aussenegg, A. Leitner, and J. R. Krenn, "Leakage radiation microscopy of surface plasmon polaritons," *Materials science and engineering: B*, vol. 149, no. 3, pp. 220–229, 2008.

[129] P. B. Johnson and R. W. Christy, "Optical constants of the noble metals," *Physical Review B*, vol. 6, no. 12, p. 4370, 1972.

[130] N. B. Dahotre and S. P. Harimkar, *Laser fabrication and machining of materials*, vol. 51. Springer, 2008.

[131] J. D. Jackson, *Classical Electrodynamics*. John Wiley & Sons, 3rd ed., 1999.

[132] J.-C. Weeber, A. Dereux, C. Girard, G. Colas des Francs, J. R. Krenn, and J. P. Goudonnet, "Optical addressing at the subwavelength scale," *Physical Review E*, vol. 62, no. 5, p. 7381, 2000.

[133] J.-C. Weeber, T. Bernardin, M. G. Nielsen, K. Hassan, S. Kaya, J. Fatome, C. Finot, A. Dereux, and N. Pleros, "Nanosecond thermo-optical dynamics of polymer loaded plasmonic waveguides," *Optics express*, vol. 21, no. 22, pp. 27291–27305, 2013.

[134] G. V. Miloshevsky, V. A. Sizyuk, M. B. Partenskii, A. Hassanein, and P. C. Jordan, "Application of finite-difference methods to membrane-mediated protein interactions and to heat and magnetic field diffusion in plasmas," *Journal of Computational Physics*, vol. 212, no. 1, pp. 25–51, 2006.

[135] R. J. LeVeque, *Finite difference methods for ordinary and partial differential equations: steady-state and time-dependent problems*, vol. 98. Siam, 2007.

[136] M. Latif, *Heat Conduction*. Springer-Verlag, Berlin Heidelberg, 2009.

[137] G. Chen and P. Hui, "Thermal conductivities of evaporated gold films on silicon and glass," *Applied physics letters*, vol. 74, no. 20, pp. 2942–2944, 1999.

[138] D. Canchal-Arias and P. Dawson, "Measurement and interpretation of the mid-infrared properties of single crystal and polycrystalline gold," *Surface science*, vol. 577, no. 2, pp. 95–111, 2005.

[139] W.-J. Lee, J.-E. Kim, H. Y. Park, S. Park, M.-s. Kim, J. T. Kim, and J. J. Ju, "Optical constants of evaporated gold films measured by surface plasmon resonance at telecommunication wavelengths," *Journal of Applied Physics*, vol. 103, no. 7, p. 073713, 2008.

[140] S. Kaya, J.-C. Weeber, F. Zacharatos, K. Hassan, T. Bernardin, B. Cluzel, J. Fatome, and C. Finot, "Photo-thermal modulation of surface plasmon polariton propagation at telecommunication wavelengths," *Optics express*, vol. 21, no. 19, pp. 22269–22284, 2013.

[141] K. Leosson, T. Rosenzveig, P. G. Hermannsson, and A. Boltasseva, "Compact plasmonic variable optical attenuator," *Optics express*, vol. 16, no. 20, pp. 15546–15552, 2008.

[142] T. Nikolajsen, K. Leosson, and S. I. Bozhevolnyi, "Surface plasmon polariton based modulators and switches operating at telecom wavelengths," *Applied Physics Letters*, vol. 85, no. 24, pp. 5833–5835, 2004.

[143] A. V. Krasavin and A. V. Zayats, "Passive photonic elements based on dielectric-loaded surface plasmon polariton waveguides," *Applied physics letters*, vol. 90, no. 21, pp. 211101–211101, 2007.

[144] O. Tsilipakos, E. E. Kriezis, and S. I. Bozhevolnyi, "Thermo-optic microring resonator switching elements made of dielectric-loaded plasmonic waveguides," *Journal of Applied Physics*, vol. 109, no. 7, p. 073111, 2011.

[145] J. Gosciniak, L. Markey, A. Dereux, and S. I. Bozhevolnyi, "Efficient thermo-optically controlled mach-zhender interferometers using dielectric-loaded plasmonic waveguides," *Optics Express*, vol. 20, no. 15, pp. 16300–16309, 2012.

[146] N. Pleros, E. E. Kriezis, and K. Vyrsokinos, "Optical interconnects using plasmonics and Si-photonics," *Photonics Journal, IEEE*, vol. 3, no. 2, pp. 296–301, 2011.

[147] O. Tsilipakos, A. Pitilakis, T. V. Yioultsis, S. Papaioannou, K. Vyrsokinos, D. Kalavrouziotis, G. Giannoulis, D. Apostolopoulos, H. Avramopoulos, T. Tekin, *et al.*, "Interfacing dielectric-loaded plasmonic and silicon photonic waveguides: Theoretical analysis and experimental demonstration," *Quantum Electronics, IEEE Journal of*, vol. 48, no. 5, pp. 678–687, 2012.

[148] M. Notomi, T. Tanabe, A. Shinya, E. Kuramochi, H. Taniyama, S. Mitsugi, and M. Morita, "Nonlinear and adiabatic control of high-q photonic crystal nanocavities," *Optics Express*, vol. 15, no. 26, pp. 17458–17481, 2007.

[149] A. H. Atabaki, A. A. Eftekhar, S. Yegnanarayanan, and A. Adibi, "Sub-100-nanosecond thermal reconfiguration of silicon photonic devices," *Optics express*, vol. 21, no. 13, pp. 15706–15718, 2013.

[150] M. Nevière and E. Popov, *Light Propagation in Periodic Media*. Marcel Dekker, Inc. New-York-Basel, 2003.

[151] E. Anemogiannis, E. N. Glytsis, and T. K. Gaylord, "Determination of guided and leaky modes in lossless and lossy planar multilayer optical waveguides: reflection pole method and wavevector density method," *Journal of lightwave technology*, vol. 17, no. 5, p. 929, 1999.

[152] R. J. Baseman, N. M. Froberg, J. C. Andreshak, and Z. Schlesinger, "Minimum fluence for laser blow-off of thin gold films at 248 and 532 nm," *Applied physics letters*, vol. 56, no. 15, pp. 1412–1414, 1990.

[153] X. Chen, Y. Chen, M. Yan, and M. Qiu, "Nanosecond photothermal effects in plasmonic nanostructures," *ACS nano*, vol. 6, no. 3, pp. 2550–2557, 2012.

[154] E. Marín, "Characteristic dimensions for heat transfer," *Latin-American Journal of Physics Education*, vol. 4, no. 1, pp. 56–60, 2010.

[155] D. Brunco, J. Kittl, C. Otis, P. Goodwin, M. O. Thompson, and M. Aziz, "Time-resolved temperature measurements during pulsed laser irradiation using thin film metal thermometers," *Review of scientific instruments*, vol. 64, no. 9, pp. 2615–2623, 1993.

[156] S. Nakamura, Y. Ueno, K. Tajima, J. Sasaki, T. Sugimoto, T. Kato, T. Shimoda, M. Itoh, H. Hatakeyama, T. Tamanuki, *et al.*, "Demultiplexing of 168-Gb/s data pulses with a hybrid-integrated symmetric mach-zehnder all-optical switch," *Photonics Technology Letters, IEEE*, vol. 12, no. 4, pp. 425–427, 2000.

[157] R. Quidant, J.-C. Weeber, A. Dereux, D. Peyrade, Y. Chen, and C. Girard, "Near-field observation of evanescent light wave coupling in subwavelength optical waveguides," *EPL (Europhysics Letters)*, vol. 57, no. 2, p. 191, 2002.

[158] J. R. Krenn, B. Lamprecht, H. Ditlbacher, G. Schider, M. Salerno, A. Leitner, and F. R. Aussenegg, "Non–diffraction-limited light transport by gold nanowires," *EPL (Europhysics Letters)*, vol. 60, no. 5, p. 663, 2002.

[159] M. I. Stockman, "Nanofocusing of optical energy in tapered plasmonic waveguides," *Physical review letters*, vol. 93, no. 13, p. 137404, 2004.

[160] L. Yin, V. K. Vlasko-Vlasov, J. Pearson, J. M. Hiller, J. Hua, U. Welp, D. E. Brown, and C. W. Kimball, "Subwavelength focusing and guiding of surface plasmons," *Nano letters*, vol. 5, no. 7, pp. 1399–1402, 2005.

[161] K. Leosson, T. Nikolajsen, A. Boltasseva, and S. I. Bozhevolnyi, "Long-range surface plasmon polariton nanowire waveguides for device applications," *Optics Express*, vol. 14, no. 1, pp. 314–319, 2006.

[162] A. W. Sanders, D. A. Routenberg, B. J. Wiley, Y. Xia, E. R. Dufresne, and M. A. Reed, "Observation of plasmon propagation, redirection, and fan-out in silver nanowires," *Nano letters*, vol. 6, no. 8, pp. 1822–1826, 2006.

[163] M. W. Knight, N. K. Grady, R. Bardhan, F. Hao, P. Nordlander, and N. J. Halas, "Nanoparticle-mediated coupling of light into a nanowire," *Nano Letters*, vol. 7, no. 8, pp. 2346–2350, 2007.

[164] A. V. Akimov, A. Mukherjee, C. L. Yu, D. E. Chang, A. S. Zibrov, P. R. Hemmer, H. Park, and M. D. Lukin, "Generation of single optical plasmons in metallic nanowires coupled to quantum dots," *Nature*, vol. 450, no. 7168, pp. 402–406, 2007.

[165] H. Wei, F. Hao, Y. Huang, W. Wang, P. Nordlander, and H. Xu, "Polarization dependence of surface-enhanced raman scattering in gold nanoparticle- nanowire systems," *Nano letters*, vol. 8, no. 8, pp. 2497–2502, 2008.

[166] J. A. Hutchison, S. P. Centeno, H. Odaka, H. Fukumura, J. Hofkens, and H. Uji-i, "Subdiffraction limited, remote excitation of surface enhanced raman scattering," *Nano letters*, vol. 9, no. 3, pp. 995–1001, 2009.

[167] Y. Fang, H. Wei, F. Hao, P. Nordlander, and H. Xu, "Remote-excitation surface-enhanced raman scattering using propagating Ag nanowire plasmons," *Nano letters*, vol. 9, no. 5, pp. 2049–2053, 2009.

[168] Z. Li, F. Hao, Y. Huang, Y. Fang, P. Nordlander, and H. Xu, "Directional light emission from propagating surface plasmons of silver nanowires," *Nano letters*, vol. 9, no. 12, pp. 4383–4386, 2009.

[169] T. Shegai, V. D. Miljkovic, K. Bao, H. Xu, P. Nordlander, P. Johansson, and M. Kall, "Unidirectional broadband light emission from supported plasmonic nanowires," *Nano letters*, vol. 11, no. 2, pp. 706–711, 2011.

[170] X. Guo, M. Qiu, J. Bao, B. J. Wiley, Q. Yang, X. Zhang, Y. Ma, H. Yu, and L. Tong, "Direct coupling of plasmonic and photonic nanowires for hybrid nanophotonic components and circuits," *Nano letters*, vol. 9, no. 12, pp. 4515–4519, 2009.

[171] R. Yan, P. Pausauskie, J. Huang, and P. Yang, "Direct photonic–plasmonic coupling and routing in single nanowires," *Proceedings of the National Academy of Sciences*, vol. 106, no. 50, pp. 21045–21050, 2009.

[172] Y. Fang, Z. Li, Y. Huang, S. Zhang, P. Nordlander, N. J. Halas, and H. Xu, "Branched silver nanowires as controllable plasmon routers," *Nano letters*, vol. 10, no. 5, pp. 1950–1954, 2010.

[173] H. Wei, Z. Li, X. Tian, Z. Wang, F. Cong, N. Liu, S. Zhang, P. Nordlander, N. J. Halas, and H. Xu, "Quantum dot-based local field imaging reveals plasmon-based interferometric logic in silver nanowire networks," *Nano letters*, vol. 11, no. 2, pp. 471–475, 2010.

[174] H. Wei, Z. Wang, X. Tian, M. Käll, and H. Xu, "Cascaded logic gates in nanophotonic plasmon networks," *Nature communications*, vol. 2, p. 387, 2011.

[175] M. Wulf, A. de Hoogh, N. Rotenberg, and L. Kuipers, "Ultrafast plasmonics on gold nanowires: Confinement, dispersion, and pulse propagation," *ACS Photonics*, vol. 1, no. 11, pp. 1173–1180, 2014.

[176] E. Verhagen, A. Polman, and L. K. Kuipers, "Nanofocusing in laterally tapered plasmonic waveguides," *Optics express*, vol. 16, no. 1, pp. 45–57, 2008.

[177] P. Morin, *Nouveaux systèmes de contrôle de la polarisation de la lumière par effets non linéaires dans les fibres optiques*. PhD thesis, Université de Bourgogne, 2013.

[178] G. Schider, J. Krenn, W. Gotschy, B. Lamprecht, H. Ditlbacher, A. Leitner, and F. Aussenegg, "Optical properties of Ag and Au nanowire gratings," *Journal of Applied Physics*, vol. 90, no. 8, pp. 3825–3830, 2001.